Use Authorization

In presenting this dissertation in partial fulfillment of the requirements for an advanced degree at Idaho State University, I agree that the Library shall make it freely available for inspection. I further state that permission to download and/or print my dissertation for scholarly purposes may be granted by the Dean of the Graduate School, Dean of my academic division, or by the University Librarian. It is understood that any copying or publication of this dissertation for financial gain shall not be allowed without my written permission.

Signature _____

Date _____

The Bloody Dick and Maiden Peak gneisses, southwest Montana: Implications for Archean and Paleoproterozoic basement framework

Nathan Dean Anderson

A thesis submitted in partial fulfillment
of the requirements for the degree of:

Master of Science in
Geology

Idaho State University

Spring 2017

Committee Approval

To the Graduate Faculty:

The members of the committee appointed to examine the thesis of Nathan Dean Anderson find it satisfactory and recommend that it be accepted.

_____

Paul Link,
Major Advisor

_____

David Pearson,
Committee Member

_____

Zac Gershberg,
Graduate Faculty Representative

Dedication

I dedicate this thesis to my children. All of the movie nights I have had to miss out on, trips to the museum I was unable to attend, vacations you had to take without me, birthdays spent apart, and all of the pumpkin carving, Easter egg coloring, and Christmas decorating that I was absent for in the pursuit of this work was done for you. I sincerely hope that the struggles and sacrifices of the last two years will be made up for by a lifetime of future opportunities, memories and security made possible by my completion of this work.

Acknowledgements

I would like to extend my gratitude to my advisor, Dr. Paul Link for always making the time to assist me with writing grants, planning fieldwork, proofreading all of my assignments and thesis drafts, fine-tuning my presentations, and for providing a wealth of invaluable knowledge. The quality and depth of my education and this thesis would be lacking without your guidance. Your actions have always demonstrated that my success was your top priority.

I also want to extend my appreciation to my committee member, Dr. David Pearson for your clear and straightforward direction, instruction and guidance. I thank you for setting tough, high expectations, but for also being a friendly and honest mentor when I needed it the most. From helping me print my poster, to video chatting with me in Tucson, to editing all of my thesis drafts, the amount of time which you have dedicated to my work has gone above and beyond that of a typical committee member.

Thanks to all of my friends at Idaho State University who have made me feel welcome. Thanks to Brandon Crawford for being my best friend these past two years. This would have been a lonely struggle without you and I'm glad we got to battle through it together. Thanks to Nick Patton for being the first person to put your arm around me, involve me, and help me feel like one of the guys.

A special thank you to Mark Pecha at the Arizona LaserChron Center for accommodating me during a tight schedule, and to Chelsi White for your patient direction regarding the operation of the equipment.

Also, thank you to those organizations that recognized the scientific potential in this work and generously funded my research. Specifically, thank you to the Belt Association, Sigma Xi, the Tobacco Root Geological Society and the SME Snake River Chapter.

Thank you to all of my past instructors at Idaho State University for your role in furthering my geologic training and increasing the depth of my knowledge. Each of your unique contributions to my education are reflected in the quality of this work.

Finally, thank you to my wife Michelle for your everlasting and unwavering support of my education. Thank you for always being gracious and willing to uproot our family and move from city to city and from state to state as needed these past ten years. We are finally done!

Table of Contents

Appendices

Plates

List of Figures

List of Tables

Abstract

In the Tendoy and Beaverhead Ranges of southwest Montana, the Maiden Peak and Bloody Dick gneiss units are both interpreted as orthogneisses. U-Pb zircon analysis of quartzofeldspathic gneiss in Maiden Peak found two distinct zircon age-populations. Within one sample, the oldest zircons were dated to the Neoarchean (ca. 2789 Ma, Beartooth orogeny), with Paleoproterozoic metamorphic rims (ca. 2497 Ma, Tendoy orogeny). Two other samples returned Paleoproterozoic U-Pb zircon crystallization ages of 2477 ± 25 Ma and 2483 ± 23 Ma. These two dates are encompassed in the ca. 2497 Ma metamorphic age peak from the older sample, which is interpreted to indicate that magmatism was concurrent with metamorphism.

Geologic mapping of the Bloody Dick gneiss has revealed four orthogneiss units. The oldest unit is the banded gneiss, which contains ca. 2476 Ma zircon cores and ca. 1761 Ma metamorphic rims. Zircons in the banded gneiss unit of the Bloody Dick gneiss and the quartzofeldspathic gneiss in Maiden Peak have statistically indistinguishable U-Pb zircon ages of ca. 2478 Ma and Hf model ages of ca. 2950 Ma. Hornblende orthogneiss intruded at ca. 1878-1900 Ma and is isotopically intermediate to juvenile (initial εHf of +1 to -7). This unit was subsequently intruded at 1802 ± 17 Ma by an isotopically juvenile (initial εHf of +3 to -3), felsic magma body, mapped as felsic orthogneiss. The Bloody Dick gneiss was exhumed in the hanging wall of the Monument thrust (the eastern strand of the Beaverhead Divide fault) during the Late Cretaceous, as shown by a zircon (U-Th)/He age of 72.4 ± 1.5 Ma. A portion of this fault was reactivated as a normal fault in Cenozoic time.

Similarities in U-Pb ages and initial εHf isotopic values (+2 to -4) of ca. 2478 Ma gneisses in the Bloody Dick and Maiden Peak areas suggests that they fundamentally belong to the same basement province. Younger hornblende gneiss and felsic orthogneisses are Paleoproterozoic and suggest input of isotopically juvenile material (initial εHf values of +3 to -7). This is similar to rocks from the Little Belt Mountains, which were interpreted to result from arc magmatism above the northwest-dipping subduction of oceanic lithosphere beneath the Medicine Hat block during the 1860 to 1790 Ma Great Falls orogeny. This correlation of arc-related rocks between the Little Belt Mountains and the Bloody Dick gneiss suggests that the Great Falls tectonic zone projects into southwest Montana. This work also establishes that the Neoarchean and Paleoproterozoic country rocks to this magmatic arc have similarities to the Wyoming province.

Chapter I: Introduction

This work seeks to further understand the Bloody Dick gneiss, a 12 km^2 exposure of enigmatic rock at the mouth of Bloody Dick Canyon, as well as quartzofeldspathic gneisses exposed near Maiden Peak in the Tendoy Range, Beaverhead County, Montana (Figures 1 and 2). In order to more fully appreciate and recognize the regional context and geological histories of these rocks, field mapping of the Bloody Dick Creek area, petrography, as well as U-Pb, Lu-Hf, and (U-Th)/He zircon analysis was conducted on samples from the Bloody Dick gneiss and similar gneisses exposed near Maiden Peak. See Figure 1 for a map of regional basement architecture surrounding the location of this study and Figure 2 for a map of regional mountain ranges. See Table 1 for the definitions of tectonic provinces and orogenies discussed in this work.

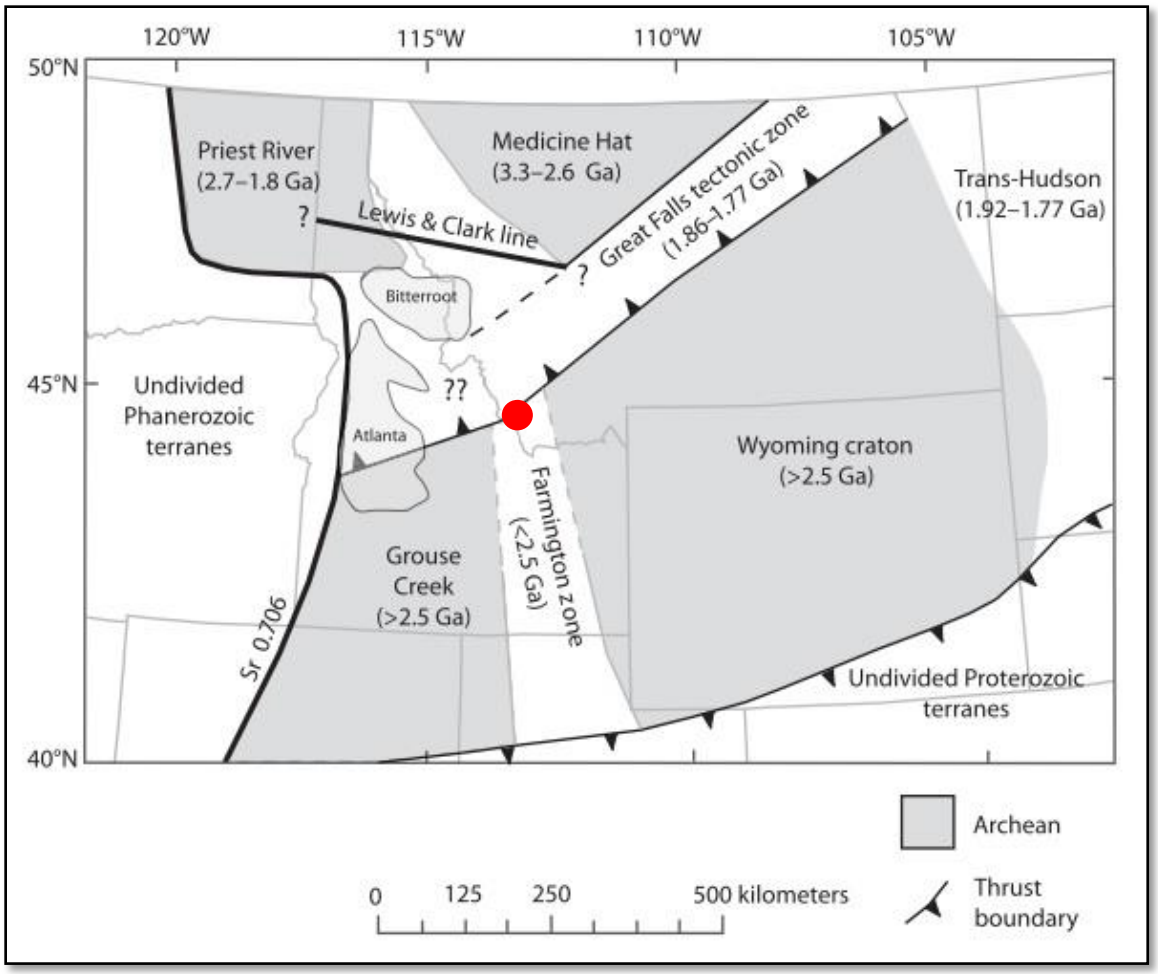

Figure 1: Configuration of regional basement architecture. Note the Farmington zone, Wyoming craton and the Great Falls tectonic zone near the Bloody Dick gneiss in southwest Montana. The study area is highlighted with a red dot. Note that the Wyoming craton and Medicine Hat block are separated by the Great Falls tectonic zone. Modified from Gaschnig et al. (2013).

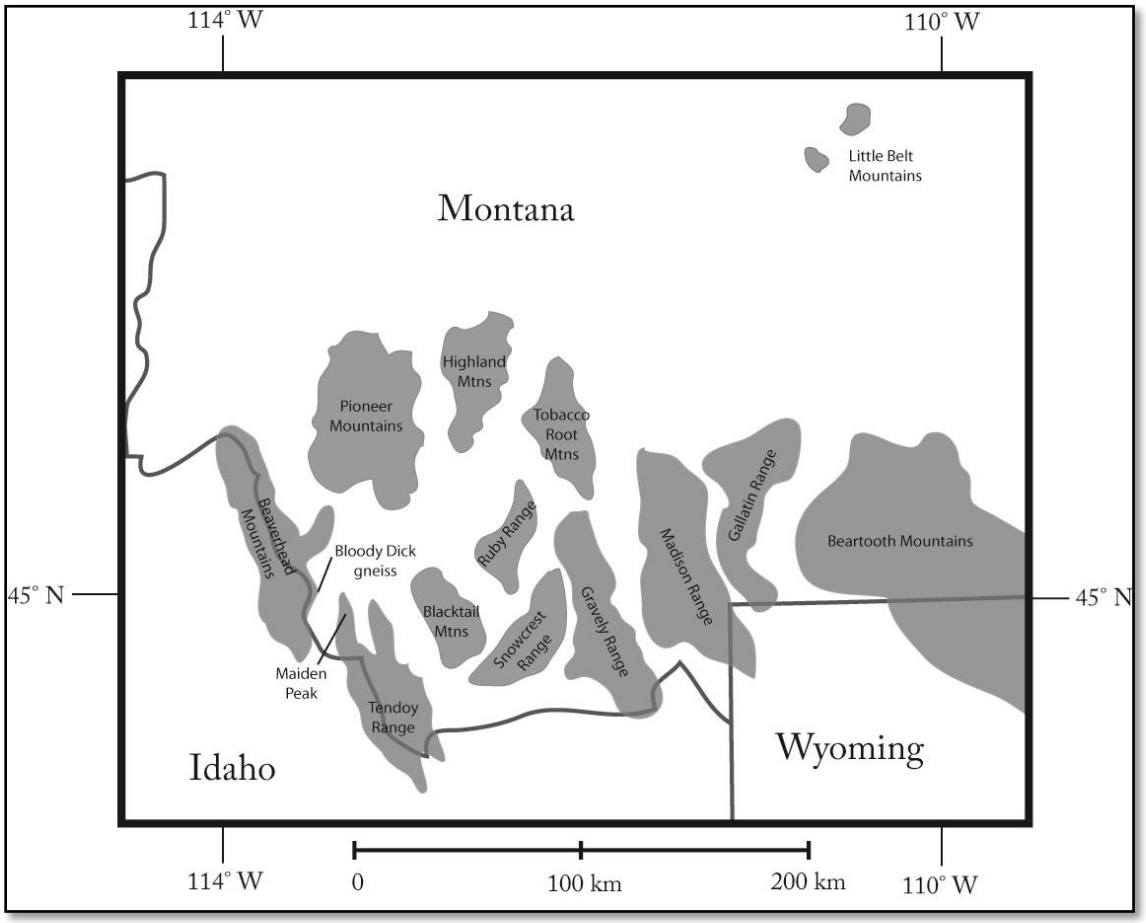

Figure 2: Map of regional mountain ranges across eastern Idaho, southwest Montana and northwest Wyoming. Note the locations of the Bloody Dick gneiss within the southern Beaverhead Mountains and Maiden Peak in the northern Tendoy Range.

Tectonic provinces	Definition	Age/timing	Major workers
Wyoming craton	An Archean crustal block primarily exposed in Wyoming and southwest Montana. The northwestern margin contains a geochemically distinct subdivision known as the Montana metasedimentary province. The craton is bounded by the Great Falls tectonic zone to the north and the Farmington zone to the west.	3500-2500 Ma	Chamberlain et al., 2003 Foster et al., 2006 Wooden and Mueller, 1988
Montana metasedimentary province	A subdivision of the Wyoming craton. Also called the Montana metasedimentary terrane, it is dominated by middle Archean gneisses intercalated with metasedimentary rocks, but also contains late Archean plutons.	3500-2500 Ma	Chamberlain et al., 2003 Mogk et al., 1992 Mueller et al., 1996
Medicine Hat block	An Archean terrane in northwestern Montana and southern Alberta known only from borehole and geophysical data. Its southern margin is bounded by the Great Falls tectonic zone, while its western margin is ambiguous it extends at least as far west as the Belt basin.	3300-2600 Ma	Ross et al., 1991 Villeneuve et al. 1993
Farmington zone	A north-south trending zone along the western margin of the Wyoming craton defined and spatially constrained by the presence of ca. 2450 Ga crustal formation and ca. 1680 metamorphism.	ca.2450 and ca. 1680 Ma	Mueller et al., 2011
Great Falls tectonic zone	A NE-SW trending zone of isotopically juvenile, Paleoproterozoic arc material which formed above a north dipping subduction zone. Spatially constrained between the Wyoming craton and the Medicine Hat block.	1860-1790 Ma	Mueller et al., 2016 O'Neill and Lopez, 1985 Vervoort et al., 2015
Orogenies			
Beartooth	A Neoarchean orogenic episode which resulted in tight folding of the preexisting metasedimentary rocks and the intrusion of tonalitic to granitic plutons within the western Wyoming craton.	ca 2700 Ma	Reid et al., 1975 Skinner et al., 1969
Tendoy/Beaverhead	A thermotectonic event along the western margin of the Wyoming craton that resulted in crustal formation and metamorphism of the Montana metasedimentary terrane. Migmatization indicates a high metamorphic grade and regional monazite of this age suggests that the metamorphism was widespread. Quartzo-feldspathic gneiss of this age is found within the Montana sedimentary province and the Farmington zone.	2550-2455 Ma	Cramer, 2014 Jones, 2008
Great Falls	The closure of the Medicine Hat ocean, associated arc magmatism and crustal anatexis during the initial burial of the northwestern margin of the Wyoming craton.	1860-1790 Ma	Harms et al., 2004 Mueller et al., 2016
Big Sky	The youngest phase of the Great Falls orogeny. Specifically, the foreland directed deformation, metamorphism and partial melting of the northwestern Wyoming craton.	1790-1720 Ma	Cheney et al., 2004 Condit et al., 2015 Harms et al., 2004

Table 1: General description of tectonic provinces and orogenies mentioned in this work.

Archean basement rock is discontinuously exposed across much of southwest Montana and Wyoming in Late Cretaceous and Tertiary basement-involved uplifts. These rocks are distinguished and spatially constrained into distinct tectonic provinces or crustal blocks (Foster et al., 2006) based on their ages and geochemistry. The Wyoming craton (see Table 1) has been subdivided by Chamberlain et al. (2003) into subprovinces based

on further variations in age and geochemistry within this cratonic block. Based on these subdivisions, much of the exposed basement gneiss in southwest Montana falls within the Montana metasedimentary subprovince, which spans the northwestern margin of the Wyoming craton. Basement rocks throughout the region are locally overprinted and metamorphosed by at least four Archean and Paleoproterozoic orogenies (see Table 1) that contributed to the early crustal formation and assembly of Laurentia.

Neoarchean and earliest Paleoproterozoic events, such as the Beartooth and Tendoy orogenies, respectively (Table 1), involved magmatism and metamorphism of much of the northwest Wyoming cratonic crust, while the later Paleoproterozoic Great Falls-Big Sky orogeny also metamorphosed the northwest margin of the Wyoming craton, specifically the Montana metasedimentary province.

Across southwestern Montana, basement exposures of Archean and Paleoproterozoic metasedimentary and metaigneous rocks of the Wyoming craton were highly metamorphosed between ca. 1780 and 1720 Ma (Harms et al., 2004; Cheney et al., 2004; Condit et al., 2015) in a northeast-trending belt of deformation associated with the Great Falls orogeny. Part of the assembly of Laurentia, this regional event involved the closure of an ocean basin, arc-related magmatism, and the subsequent collision of the Wyoming craton with the Medicine Hat block to the north (Mueller et al., 2016). Spatially constrained between these two blocks, the Great Falls tectonic zone contains this ca. 1860 Ma to 1790 Ma, isotopically juvenile arc material.

Previous workers have interpreted the Bloody Dick gneiss to be Archean in age (Geach, 1972; Coppinger, 1974; Hansen, 1983), possibly associated with other regional exposures of Archean basement rock of the Wyoming craton across southwest Montana

(VanDenburg et al., 1998). However, one recent U-Pb analysis of 100 zircon grains from the Bloody Dick gneiss revealed a strong, Paleoproterozoic, ca. 1878 Ma zircon age peak with 3 to 4 minor age peaks clustered around ca. 2500 Ma (Sherwin et al., 2016). Given prior authors' interpretation of a portion of the Bloody Dick gneiss as a paragneiss, the ca. 1850-1860 Ma zircons were interpreted to reflect a distal provenance of these rocks (Link et al., 2016). Alternatively, they could have been derived from the Great Falls tectonic zone, a proximal source.

The southwestern projection of the Great Falls tectonic zone into southwest Montana and eastern Idaho is ambiguous and was recently questioned by Gaschnig et al. (2013). It was recognized that an examination of the Bloody Dick gneiss has the potential to further constrain the spatial distribution of the Great Falls tectonic zone if an affinity between it and the Bloody Dick gneiss could be demonstrated.

The northern margin of the Bloody Dick gneiss is constrained by the Monument thrust, a poorly understood fault that accommodated over 5 km of stratigraphic separation. The fault was hypothesized to be the along-strike equivalent of the eastern strand of the Beaverhead Divide fault system and Cabin thrust (Lonn et al., 2016; Skipp, 1988).

Chapter II: Geologic Setting

Archean and Proterozoic Crustal Formation

The Wyoming craton is an Archean crustal block discontinuously exposed in basement uplifts across southwest Montana and much of Wyoming (Table 1, Figure1). This craton has been subdivided by Chamberlain et al. (2003) into temporally and geochemically distinct subprovinces, which aid in the interpretation of craton formation. Much of southwest Montana is included in the Montana metasedimentary province (Table 1), which is the northwestern subprovince of the Wyoming craton. Based on U-Pb zircon ages, early workers (Skinner et al., 1969; Reid et al., 1975) recognized a regional metamorphic and plutonic age of ca. 2700 Ma to have occurred during the Beartooth orogeny (Table 1). This Neoarchean orogenic episode resulted in tight folding of the preexisting metasedimentary rocks and the intrusion of tonalitic to granitic plutons within the Wyoming craton. Later work by Wooden and Mueller (1988) refined and constrained the age of the Beartooth orogeny to 2780 Ma based on Pb-Pb zircon and monazite and Rb-Sr whole-rock ages from the Beartooth Mountains (Figure 2). These rocks were later intruded and metamorphosed during the Tendoy orogeny.

Kellogg et al. (2003) utilized U-Pb zircon dating of gneisses in the Tendoy Range (Figure 2), which yielded an average $^{207}Pb/^{206}Pb$ date of 2455 ± 9 Ma. Gneisses of a similar age have been found in the Tobacco Root Mountains by Jones (2008), who associated their formation with the Beaverhead orogeny, and in the Ruby Range by Cramer et al. (2014) who refers to this same event as the Tendoy orogeny. These ca. 2450 Ga rocks have been interpreted to reflect early Paleoproterozoic plutonism, resulting in regional metamorphism (Baldwin et al, 2014).

Previous workers typically referred to the gneiss in the Tendoy Range as the Dillon Granite Gneiss (Heinrich, 1949; Lucchitta, 1966; M'Gonigle, 1965; James and Hedge, 1980; Skipp, 1988), while others refer to it generally as a quartzofeldspathic gneiss (Kellogg et al., 2003) or more completely as the Dillon quartzofeldspathic gneiss (Cramer, 2014; D'Amato, 1994; Garihan and Okuma, 1974; James, 1990 and Jones, 2008). M'Gonigle and Hait (1997) and James (1990) do not use the name Dillon Granite gneiss, stating that such a name is poorly constrained and defined. In addition to the Bloody Dick gneiss (Everson Creek and Coyote Creek 7.5' quadrangles, this study focuses in part on gneiss within Maiden Peak of the Tendoy Range (Jeff Davis 7.5' quad; M'Gonigle and Hait, 1997) which is herein referred to as the quartzofeldspathic gneiss.

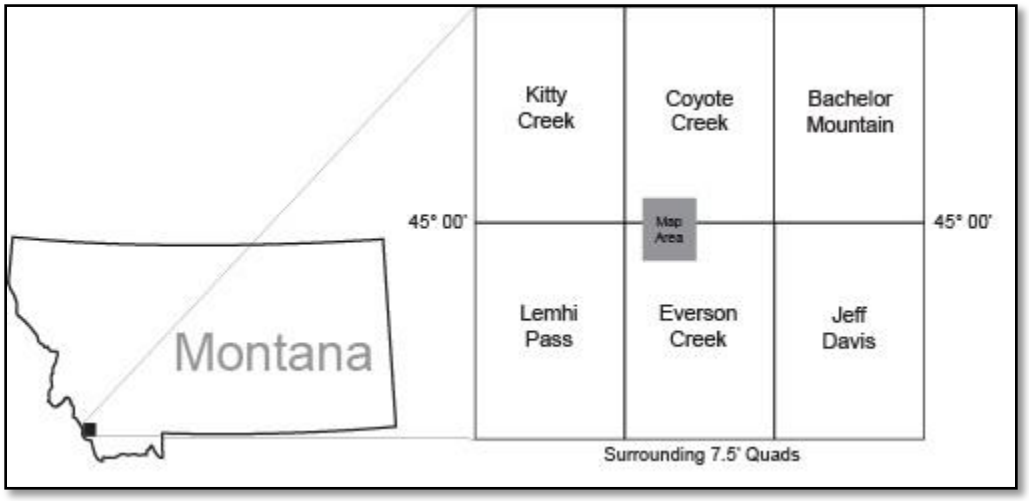

Figure 3: Location of the Bloody Dick gneiss map (Plate 1) and surrounding 7.5' quads.

Great Falls Orogeny

Originally called the Big Sky orogeny (Harms et al., 2004), Mueller et al. (2016) used the term "Great Falls" orogeny to specifically refer to the ca. 1860 – 1790 Ma closure of the Medicine Hat ocean, associated arc magmatism, and the burial of the

Montana metasedimentary terrane beneath the overriding Medicine Hat block. The Great Falls orogeny has been interpreted to result from Paleoproterozoic plate convergence during closure of the Medicine Hat ocean and the subsequent collision of the Medicine Hat block and the Wyoming craton (Figure 1; Harms et al., 2004; Foster et al., 2006; Mueller et al., 2016). Mueller et al. (2016) define the "Big Sky" orogeny as the latest phase of the Great Falls orogeny that is characterized by 1790 – ca. 1720 metamorphism, deformation, and partial melting within the Montana metasedimentary terrane.

Medicine Hat Ocean and Subduction

Given the name "Medicine Hat ocean" by Mueller et al. (2016), this Paleoproterozoic ocean basin separated the encroaching Medicine Hat block from the Wyoming craton (Figure 1). In an attempt to image the subsurface structure of the Great Falls orogenic belt, geophysical data along a north-south seismic line between central Wyoming and northern Alberta were obtained by Gorman et al. (2002). The seismic data were interpreted to reflect the presence of two northwest dipping seismic reflectors. Based on its northeast striking orientation, location relative to the Wyoming craton, the Great Falls tectonic zone, and the Medicine Hat block, Harms et al. (2004) interpret the seismic reflector to be a Paleoproterozoic cryptic suture between the Wyoming craton and Medicine Hat block, associated with the Big Sky orogeny.

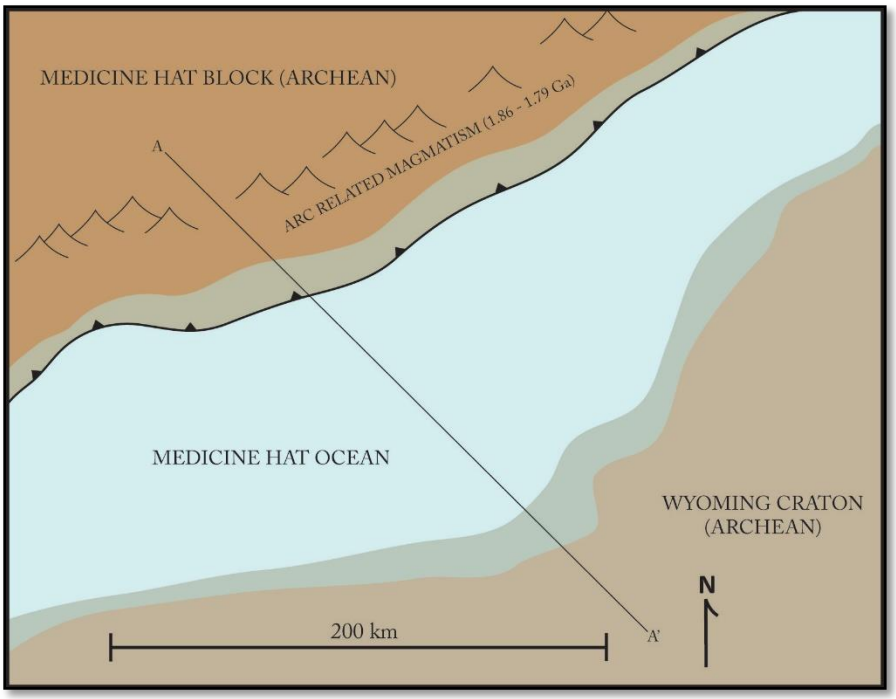

Figure 4: Schematic map of one possible convergent geometry between the Medicine Hat block and Wyoming craton during the Paleoproterozoic assembly of western Laurentia. Note that the Medicine Hat block is the overriding plate and contains the convergent magmatic arc. See Figure 5 below for A – A' cross section.

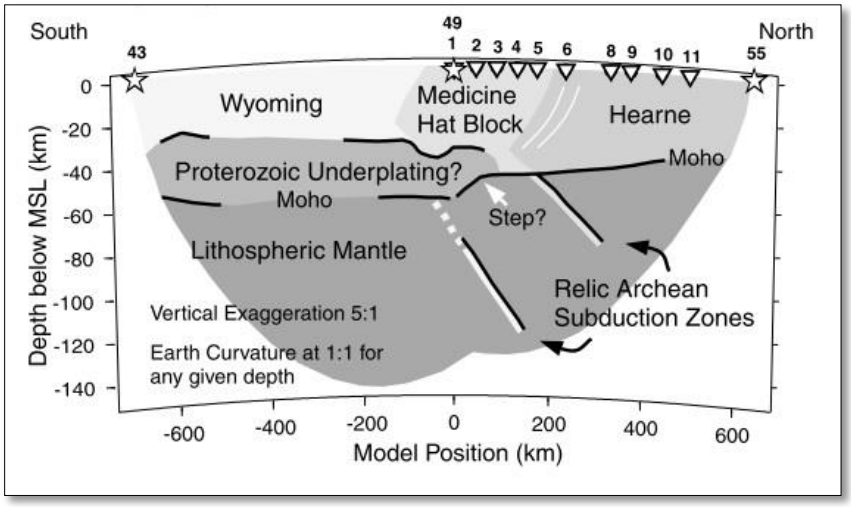

Figure 5: Cross-sectional interpretation of seismic data across a north-south transect through Alberta, Montana and Wyoming (Gorman et al., 2002).

Timing for the closure of this ocean is constrained to between 1.86 and 1.79 Ga based on U-Pb zircon dates from igneous rocks in the Little Belt Mountains (Figure 2) that have been interpreted to reflect subduction-related arc magmatism (Mueller et al., 2002). These authors also interpreted Sm-Nd isotope analysis of these rocks to suggest that this magmatic arc was derived from an isotopically juvenile, depleted mantle source (Figures 6a and 6b), which is typical of subduction-related magmatic arcs (Thompson et al., 1984). A very minor component of inherited zircon cores or xenoliths in this rock are evidence for at least some intrusion or involvement of Archean continental crust (Mueller et al., 2002).

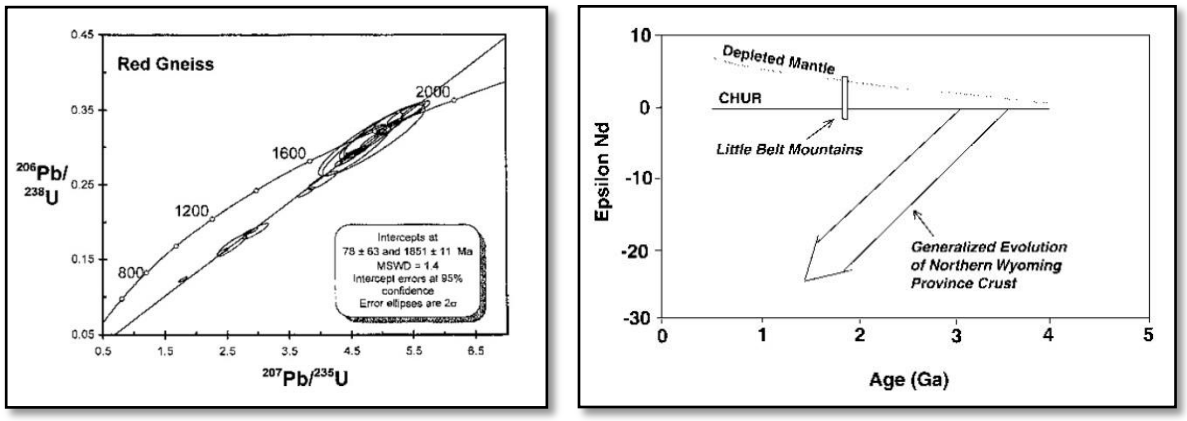

Figures 6a and 6b: 6a. 1851 ± 11 Ma U-Pb zircon dates from rocks in the Little Belt Mountains that are interpreted to be arc-related. **6b.** Sm-Nd isotopic data indicate that the material is isotopically juvenile and was derived from the mantle in the Paleoproterozoic as opposed to being derived from older, more isotopically evolved, cratonic material (Mueller et al., 2002).

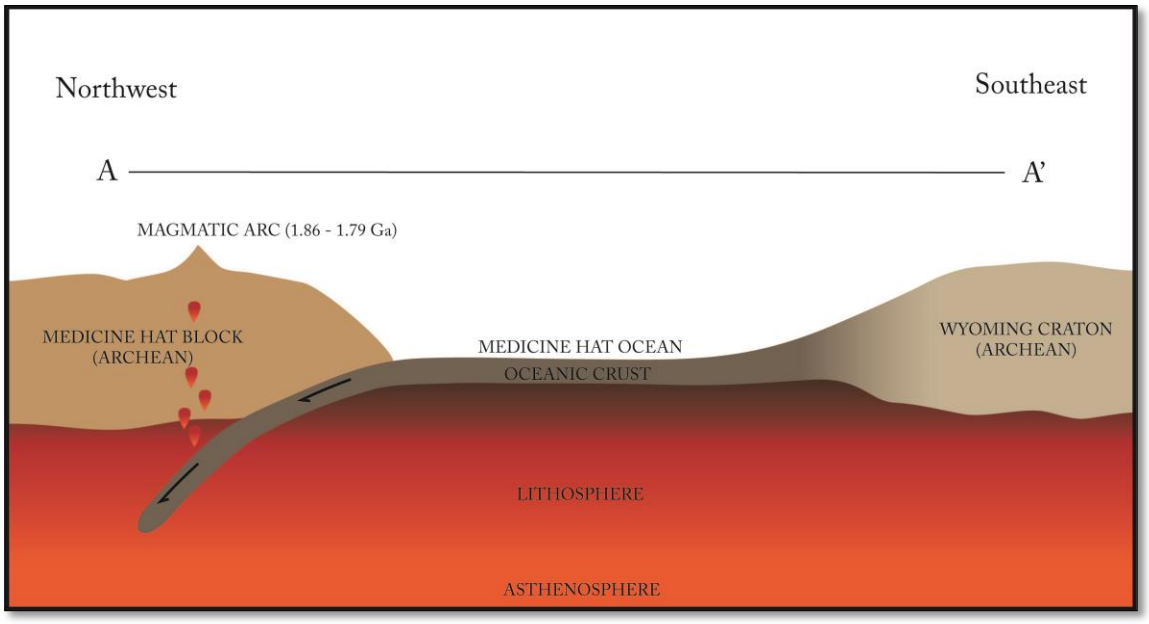

Figure 7: Schematic cross section between A and A' (see Figure 2) of the convergent geometry between the Medicine Hat block and the Wyoming craton, which resulted in closure of the Medicine Hat ocean basin.

Geometry and Timing Constraints

Geophysical data provided by Gorman et al. (2002), supports the interpretation by Harms et al. (2004) that the Medicine Hat block was the overriding plate during collision. While radiometric age-dating of igneous zircons from magmatic arc rocks constrain the timing of subduction of oceanic lithosphere, monazite and metamorphic zircons in the Wyoming craton can be used to constrain the timing of collision-related metamorphism between the Wyoming craton and Medicine Hat block.

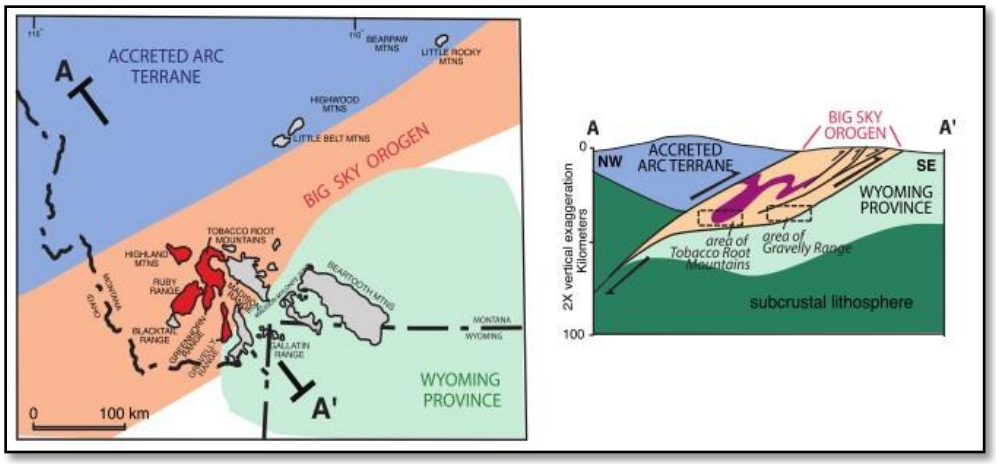

Figure 8: Map and cross-sectional views of the Big Sky orogenic system in southwestern Montana after collision of the Medicine Hat block and Wyoming craton. Note the interpretation that the Wyoming craton and Montana sedimentary terrane was thrust beneath the Medicine Hat block (Harms et al., 2006).

Ages of plutons interpreted to result from arc-related magmatism associated with the Great Falls orogeny constrain closure of the Medicine Hat ocean to ca. 1860 Ma to 1790 Ma (Mueller et al., 2016). After 1790 Ma, initiation of collision between the Wyoming craton and Medicine Hat block and the subsequent metamorphism and underthrusting of the Wyoming craton are constrained by isotopic dating of metamorphic zircons and garnets from the Tobacco Root Mountains, Ruby Range, Highland Range and Madison Range (Figure 2; O'Neill and Lopez, 1985; Mogk, et al., 1992; Harms et al., 2004; Mueller et al., 2005). Evidence for continued orogenic deformation and metamorphism is derived from the growth of metamorphic rims around zircon grains, which continued through 1.73 Ga (Figure 9b) (Condit et al., 2015).

Recent work published by Condit el at. (2015) utilized U-Pb dating of monazite and metamorphic zircons along a linear transect (Y – Y', see Figure 9a) and revealed a trend of metamorphism that becomes younger toward the southeast, with increasing

distance from the Great Falls tectonic zone. This observation has been interpreted to reflect the foreland progression of high-grade metamorphism in the Wyoming craton as the Big Sky orogeny propagated toward the southeast (Condit et al., 2015).

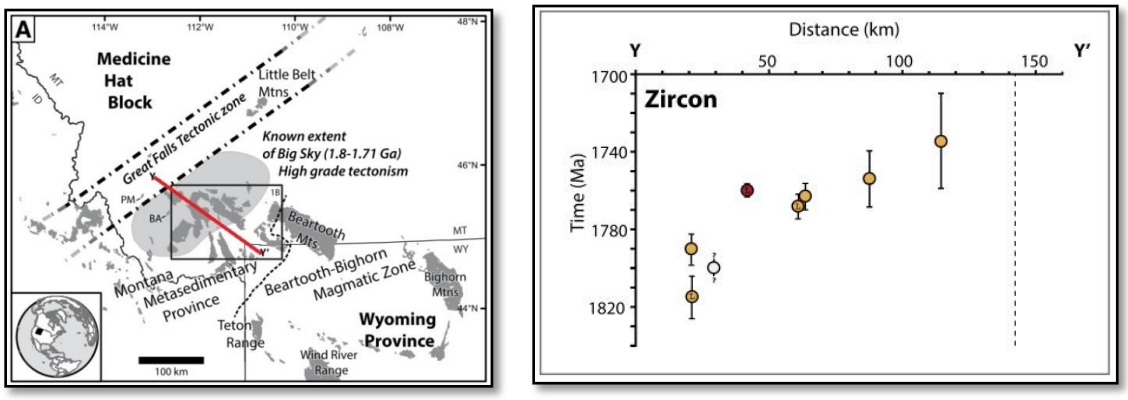

Figures 9a and 9b: Age progression of metamorphic zircon rims across a NW-SE transect between Y and Y'. Interpreted as evidence for the southeastward propagation of high-grade metamorphism during the Big Sky orogeny (Condit et al., 2015).

Ongoing Questions

Though it is generally accepted that the Great Falls tectonic zone represents a suture zone between the Medicine Hat block and Wyoming craton, Vervoort et al. (2015) point out some of the potential flaws with this model, such as the discontinuous nature of Paleoproterozoic magmatism that may be inconsistent with a NE trending, linear, magmatic arc within the Great Falls tectonic zone. The authors also draw attention to the bimodal distribution of 2660 and 1860 Ma zircon ages in orthogneisses of the Clearwater and Priest River complexes in northern Idaho. The authors state that their 4 plutonic, 2660 Ma zircon samples lack xenocrysts or any evidence of older material, while 5 of their 14 zircons of the 1860 Ma age peak do contain inherited 2660 Ma zircon cores. The authors interpret these U-Pb data to reflect a ~2660 Ma plutonic event and a ~1860 Ma

magmatic event related to the Great Falls orogeny that intruded into and incorporated material of the preexisting crust. They point out that this ~1860 Ma zircon age peak is not observed in exposed rock to the south into Idaho or Montana. This observation leaves the 1860 Ma, Great Falls orogeny related zircons in northern Idaho spatially isolated a few hundred kilometers north of the generally accepted suture zone of the orogen.

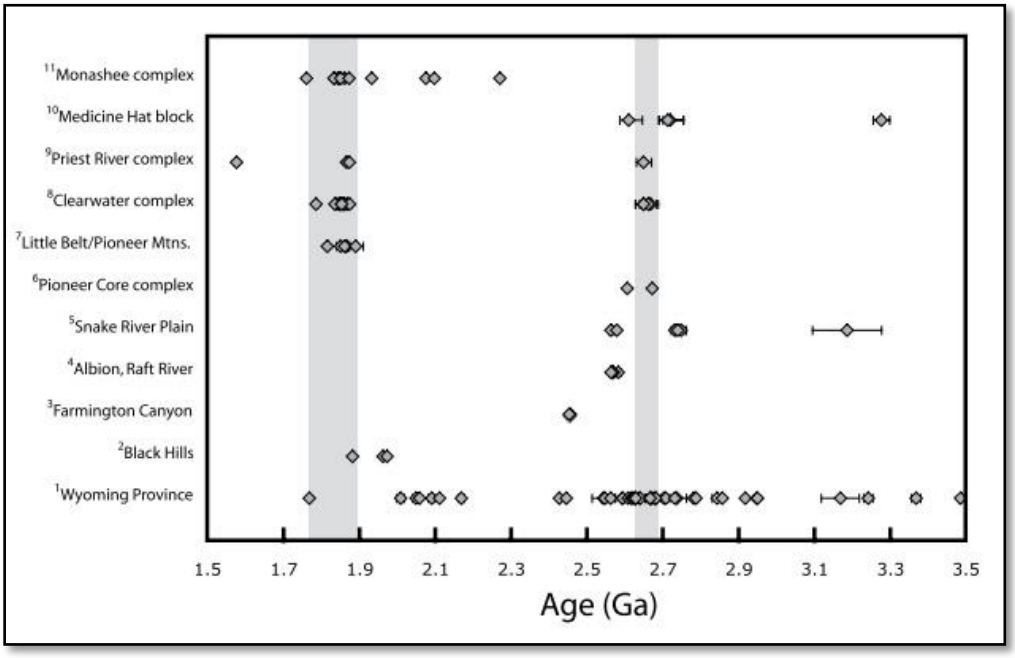

Figure 10: Regional U-Pb zircon dates from locations around the Great Falls tectonic zone (Vervoort et al., 2015).

Metasedimentary rocks of the Montana metasedimentary province are intruded by dikes and sills, dated by Mueller et al. (2002) through U-Pb zircon analysis and were found to have an intrusive age of 2060 Ma. Harms et al. (2004) proposed that continental rifting at this time was the most likely cause of these intrusions based on major element compositions of the dikes and sills that indicate a subalkaline, tholeiitic basalt protolith with rare earth element patterns that are similar to basalts intruded into modern

continental rift settings. The authors further speculate that this rift would have opened up south of the Tobacco Root Mountains, rifting the Montana metasedimentary province from the rest of the Wyoming craton and forming an ocean basin. It is this ocean basin that would later close in the Great Falls orogeny, leading to the collision of the Medicine Hat block with the Wyoming craton, spatially constraining the previously rifted Montana metasedimentary province and arc related Great Falls tectonic zone between the two. Additionally, these authors mention the possibility that the Medicine Hat block was related to the Wyoming craton prior to 2060 Ma rifting based on the observation of others that the Medicine Hat block and Wyoming craton do share a distinct crustal structure (Gorman et al., 2002) and Archean ages (Ross et al., 1991).

Farmington Zone

The Farmington zone is defined and spatially constrained by the presence of 2450-2480 Ma gneiss and 1670 Ma metamorphism (Mueller et al., 2011). However, similar U-Pb zircon ages of ca. 2450 Ma were obtained from gneisses found in the Tendoy Range (Kellogg et al., 2003), in the Tobacco Root Mountains (Jones, 2008), and the Ruby Range (Cramer, 2014). If this 2.45 Ga age peak is also interpreted as a signature of the Farmington zone, it suggests this zone may extend all along the western margin of the Wyoming Craton. This, however, presents difficulties due to the fact that ca. 2450 Ma gneiss in southwest Montana underwent regional, upper amphibolite-facies metamorphism that was concurrent with growth of metamorphic monazite from the Tobacco Root Mountains (Harms et al., 2004), zircons with metamorphic rims from the Tobacco Root Mountains (Jones, 2008) and monazite inclusions in garnet from the Ruby

Range (Baldwin, et al., 2014). Such a regional metamorphic event is generally interpreted as evidence for crustal thickening. Such characteristics are difficult to reconcile with a rifting model and seem to require a thermotectonic, collisional orogenic event at 2.45 Ga along the western margin of the Wyoming Craton in order to account for the high grade of metamorphism. Baldwin et al. (2014) proposed an alternative interpretation of the ca. 2450 Ma gneiss and metamorphism in southwest Montana, correlating it with the Tendoy orogeny, alternatively called the Beaverhead orogeny by Jones (2008).

Belt Basin

Subsidence of the Belt basin began ca. 1470 Ma, in response to crustal thinning during the initial stages of development of an intracontinental rift system in the Rodinian supercontinent (Lyons et al., 2000); extension continued through 1400 Ma. These dates were constrained by U-Pb zircon analysis of 1470 Ma mafic sills in the Prichard Formation that are interpreted by the authors as being syndepositional with this lower Belt unit (Sears et al., 1998). In the upper most Missoula Group, a 1401 ± 6 Ma volcanic tuff (Evans et al., 2000) within the upper Bonner Formation constrains the timing of this very late stage deposition (Hahn and Hughes, 1984). In the central Belt basin, Doughty and Chamberlain (1996) identified 1370 Ma plutons that intrude the upper stratigraphy of the Belt Supergroup, constraining the latest stages of Belt deposition.

Today, Belt basin sedimentary rocks are exposed across the three U.S. states of Washington, Idaho and Montana as well as the Canadian provinces of Alberta and British Columbia. In Bloody Dick Canyon, upper Belt sedimentary rocks are juxtaposed against the older Bloody Dick gneiss by the Monument and Bloody Dick faults (VanDenburg,

1997; Lonn et al., in preparation; Sherwin et al., 2016). Sedimentary rocks of the upper Belt Supergroup are primarily composed of cross-bedded, feldspathic quartzite units with interbedded shale and siltstone and are interpreted as having formed in a Mesoproterozoic, shallow water to fluvial depositional environment (Link et al., 2016). The stratigraphy of the Belt Basin, specifically within the Lemhi subbasin, which is exposed in Bloody Dick Canyon, has most recently been established by Burmester et al. (2016).

Idaho Batholith and Sevier Fold-Thrust Belt

The passive western margin of Laurentia transitioned into a contractional, west-facing convergent margin in the Jurassic with eastward subduction of the Farallon Plate beneath the North American Plate leading to major plutonism (DeCelles, 2004). The exposed roots of the magmatic arc formed during ocean-continent subduction beneath the northern Rockies are exposed in the Idaho batholith, which is predominantly Cretaceous in age, is largely granite and granodiorite in composition, and was intruded at 4 to 25 km depths (Lewis et al., 1987; Gaschnig et al., 2010). Today the batholith is exposed at the surface across central Idaho in two primary lobes: 1) The Atlanta lobe is the southern of the two and crystallized between 100 and 75 Ma, 2) while the more northern Bitterroot lobe is younger, crystallizing between 85 and 65 Ma based on U-Pb dating of igneous zircons (Gaschnig et al., 2010). As previously described, the Idaho batholith intruded through Archean and Paleoproterozoic crust, evident from inherited zircons that can be found within the batholith (Gaschnig et al., 2013).

From Early Cretaceous to early Cenozoic time, the region east of the batholith was subjected to retroarc shortening, which was accommodated by regional thrust faults that propagated progressively eastward (DeCelles, 2004). Contractional deformation reached southwestern Montana by Late Cretaceous time and was dominated by thin-skinned, west or southwest dipping thrusts (DeCelles, 2004). Of these regional thrusts, Skipp (1988) identified and distinguished the Cabin thrust by its unique involvement of crystalline basement rocks that are carried in the hanging wall. She interpreted the incorporation of this basement rock as a defining characteristic of the Cabin thrust and used this interpretation to laterally conjoin the Cabin thrust, east of Maiden Peak, to the Beaverhead Divide fault system μkm to the northwest in Bloody Dick Canyon. This interpretation placed the quartzofeldspathic gneiss of Maiden Peak and the gneiss at the mouth of Bloody Dick Canyon within the same thrust sheet, an interpretation also shared by Lonn et al. (2016).

In southwestern Montana, the southeast-striking, southwest-dipping Cabin-Beaverhead Divide fault cuts through the Beaverhead Range for no less than 30 km until it approaches the mouth of Bloody Dick Canyon. The eastern strand of the Beaverhead Divide fault (ESBDF) cuts up-section to the northeast through Mesoproterozoic, Belt basin quartzite units, placing rocks of the Jahnke Lake Member of the Apple Creek Formation next to older rock of the Swauger Formation in Bloody Dick Canyon (Lonn et al., 2016), a stratigraphic throw between 1000 and 5000 meters (Burmester et al., 2016). However, the ESBDF is interpreted by Lonn et al. (2016) as a thrust, reactivated by a normal fault, suggesting that the original stratigraphic separation was greater than what is observed today. Near the southern end of the ESBDF, the Monument fault splits off to

the east, while the ESBDF continues to the south across Bloody Dick Canyon. The Bloody Dick gneiss is constrained between these faults and over 5 km of stratigraphic separation is suggested along the Monument fault by the presence of basement rocks over the Swauger Formation (Burmester et al., 2016).

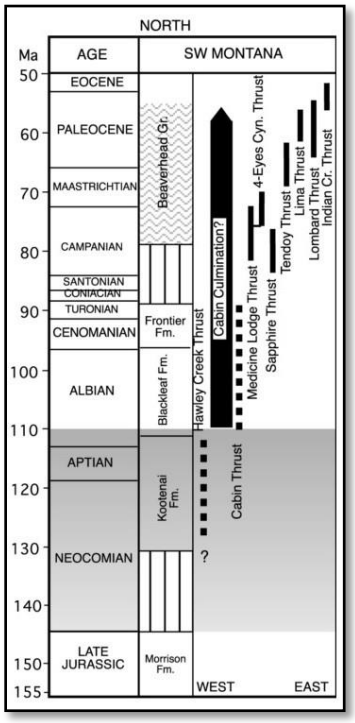

Figure 11: Hypothesized timing of thrusting in southwestern Montana during Sevier orogenesis (DeCelles, 2004).

Challis Volcanism and Extension

Part of an expansive suite of regional Eocene volcanism, the Challis volcanic field covers 25,000 km^3 across Idaho and southwestern Montana. According to Moye et al. (1988), in central Idaho, early volcanic activity was dominated by eruption of mafic and intermediate lava flows that initiated at 51 Ma, followed by the explosive eruption of stratovolcanoes that deposited extensive ash-flow tuffs and felsic localized lava flows between 49 and 44 Ma. Late stage volcanism involved formation of rhyolitic domes that

erupted material through 40 Ma. The dating of Challis volcanic rocks in south-central Idaho was done through $^{40}Ar/^{39}Ar$ analysis of biotite, sanidine and hornblende minerals by Sanford (2005). In southwest Montana, feldspar and biotite were also dated by $^{40}Ar/^{39}Ar$ (M'Gonigle and Dalrymple, 1996).

Volcanism was accompanied by formation of a northeast-trending extensional fault system called the Trans-Challis fault system, as well as associated volcanism which developed contemporaneously (Bennett, 1986). The majority of volcanism occurred between 51 and 45 Ma, with minor plutonic activity continued through 40 Ma (VanDenburg et al., 1998). The initiation of volcanism was attributed to a decrease in the convergence rates between the Farallon Plate and North American Plate (Janecke, 1992).

Near the southern mouth of Bloody Dick Canyon, rocks of the Challis Volcanic Group unconformably overlie the Bloody Dick gneiss and surrounding quartzite units of the Belt basin (see geologic map, Plate 1). Additionally, a diabase intrusion is found to have intruded along the ESBDF (Sherwin et al., 2016). This fault juxtaposed quartzite of the Jahnke Lake Member of the Apple Creek Formation against Bloody Dick gneiss in the footwall. This diabase was dated using $^{40}Ar/^{39}Ar$ methods, which yielded a highly disturbed age spectrum of uncertain geological significance that varied from 200 to 1150 Ma (VanDenburg et al., 1998). Unconformably overlying the Bloody Dick gneiss, the Jahnke Lake Member quartzite, and the diabase, is an aphanitic basalt. An $^{40}Ar/^{39}Ar$ groundmass concentrate yielded an age of 47.51 ± 0.42 Ma (VanDenburg et al., 1998). These results suggest that the basalt was associated with Challis-age volcanism and that normal faulting along the ESBDF occurred before ~48 Ma.

Basin-Range Extension

The most recent structural alteration in the interior region of western North America has been east-west crustal extension facilitated by normal faults. This repeated series of Basin and Range features have been thinning and lengthening the crust across much of the American West since 17 Ma (Proffett, 1977; Rodgers et al., 2002). North of Idaho's eastern Snake River Plain, major normal faults associated with the Basin and Range strike to the north-northwest, forming three ranges, namely the Beaverhead, Lemhi and Lost River Mountains, each separated by a valley of basin-fill deposits derived from the surrounding highlands (Link and Janecke, 1999). The eastern flank of the Beaverhead Mountains contains exposures of the Bloody Dick gneiss in Bloody Dick Canyon, 20 km west of Grant, Montana.

Chapter III: Methods

Geologic Mapping

Field work in southwest Montana began on May 5th, 2016 and continued through June 2nd of the same year. The Bloody Dick gneiss is exposed in two sections on the north and south sides of Bloody Dick Canyon. Geologic mapping was accomplished through the use of 1:24,000 topographic maps of the Coyote Creek and Everson Creek quadrangles upon which geologic contacts, faults, foliations and sample sites were recorded while in the field. Planes and lineations were measured through using a Brunton compass, while locations were provided through the use of a handheld GPS. All notes, observations and measurements were documented in a field book or directly onto the field map when appropriate. Digitization of the field map began in August, 2016 and was accomplished using Adobe Illustrator to create semi-transparent layers and symbols over 1:24,000 topographic base maps. Satellite imagery available through Google Earth was also used to identify breaks in topography, color changes in soil and surface rock, mineral exploration pits and rock outcrops to aid in mapping and corroborate field observations. Specifically, a September 2009 satellite image was particularly useful due to its relatively high contrast, resolution, lighting angle and seasonality.

Construction of the geologic cross section was completed using the finalized geologic map and topographic data. The cross section line was constructed nearly perpendicular to the Monument fault in order to illustrate its true dip angle while also encompassing all of the other major lithologic units and faults relevant to the Bloody Dick gneiss. Interpretations of subsurface geometry were constructed to match surface observations and illustrate regional geologic relationships.

Sample acquisition

While in the field, 27 individual lithologic samples were collected to be used as hand samples, thin sections, or for isotopic analysis. Each sample was collected in an individual bag of non-woven, point bonded polyester material. Upon sample acquisition, each corresponding bag was immediately labeled with a unique identification number, a brief note about the sample and the latitude, longitude and elevation of the collection site. A running log of the same information was also compiled in a field book for organization and accounting purposes.

Petrography

Lithologic samples collected while in the field were cut into 24x46x12 mm billets with the use of a water cooled, diamond blade saw. Oriented samples were notched with the saw blade in their upper-right hand corner to identify their orientation. Unfortunately, the thin sections were mounted backwards by the contract company, placing the notches in the upper-left hand corner and my notes regarding thin section orientation had to be edited by 180°. Consequently, care needs to be taken when reviewing these thin sections to assure that the proper orientation is interpreted as not all notes in the field book were edited by 180°. See Appendix D for the corrected orientation of thin sections.

The billets were sent to Wagner Petrographic in Lindon, Utah where they were mounted on glass slides, cut to 30 μm in thickness, stained with sodium cobaltinitrite ($Na_3Co(NO_2)_6$) to aid in the identification of potassium feldspar, and protected with a transparent cover slip.

The thin sections were analyzed and interpreted with the use of a Nikon Eclipse E400 polarizing microscope and a top-mounted Leica DFC290 camera that was used to capture images of each sample under plane polarized and cross polarized light. Once the present mineral assemblage was determined, relative mineral abundances were estimated under 2X, 10X and 20X magnification with consideration given for mineralogical variations across the 24x46 mm thin section. Relative mineral abundances and deformation fabrics within the rocks were then used to assign each sample a proper lithologic name following the guidelines presented in Schmid et al., (2007). See Appendix D for full petrographic results and images.

Thin sections of oriented samples were used to determine the sense of shear through the identification of sigma and delta structures, S-C fabrics and folds. Interpretation of these structures yields a "top to the right" or "top to the left" sense of shear that was converted into an azimuth.

Zircon Sample Separation

A total of 5 samples were selected for U-Pb dating of zircon grains and the separation process was undertaken at Idaho State University's mineral separation lab between September and December of 2016. Under strictly obeyed laboratory cleaning practices, each sample was broken up using a Braun Chipmunk jaw crusher to reduce the particle size to between 1-2 cm in diameter. The sample was then fed through a rotating disk mill, further reducing the grain size down to a fine sand that was then sieved through a 425 μm screen. Particles that did not pass through the screen were again fed through the disk mill until ~100% of the sample successfully passed through the screen. A hand

magnet was then used to remove iron filings that were introduced into the sample from the jaw crusher and disk mill in an effort to minimize iron oxidation stains on equipment used in subsequent mineral separation steps. Each sample, now reduced to fine sand, was individually passed over a Holman-Wilfley water table that sorted the particles by density. The densest particles were collected in an aluminum foil catch while less dense material was collected in small buckets before being stored in plastic bags. The material in the aluminum foil catch was passed over the table a second time and the material of the greatest density was again collected in a foil catch. Less dense material was collected and stored in a plastic bag. This final collection of the densest material was then dried in a hot air convection oven at between 35 and 45 degrees Celsius.

The dried material typically consisted of between 40 and 60 cm^3, which then underwent further separation of magnetic material through the use of a Frantz barrier-field magnetic separator. This step removed approximately 50-70% of the sample volume, leaving behind a quartz and zircon rich volume of around 15 to 20 cm^3. Final mineral separation was completed by pouring the remaining sample into a separatory funnel containing ~250 mL of methylene iodide (CH_2I_2) and permitting the solution to settle for up to 8 seconds, allowing the denser zircons to quickly sink, while the less dense quartz grains float, or sink more slowly. Between 2 and 4 mL of methylene iodide and zircon grains were drained from the bottom of the separatory funnel into filter paper where the zircons were cleaned with acetone (C_3H_6O) and allowed to dry. With the aid of a microscope and tweezers, a few remaining grains of quartz and metallic material were plucked from the zircon grains, resulting in a collection of >99% zircon crystals.

Zircons were mounted in an epoxy solution within a 2.5 cm plastic ring. Mount #1 contained zircons from samples 02NA16, 03NA16 and 04NA16, all derived from the Maiden Peak area. Each sample was prepared for U-Pb zircon analysis of 30 grains, so approximately 50 zircon grains were selected from each sample. Grains were selected based on their euhedral shape, lack of inclusions, chips or other defects. Mount #2 contained zircons from sample 18NA16 and 25NA16, both from the Bloody Dick gneiss. Given the uncertainty about the protolith of these two samples, the mounts were prepared according to U-Pb zircon analysis guidelines for detrital zircon samples (n=100). Approximately 150-200 grains were randomly poured from the sample vile onto the mount and arranged so that they did not touch or overlap. Each mount also included the U-Pb analysis standards SL and R-33, along with the Hf standards FC, PLES, TEM, 91500, and MT, which are discussed in more detail below. Each 2.5 cm mount was set in epoxy, polished and sent to the LaserChron Center at the University of Arizona in Tucson for imaging. Cathodoluminescence (CL) images for each sample produced unfavorable results, likely due to the relatively old age of the zircon crystals. However, high-resolution backscattered electron images were able to produce acceptable results that allowed for the identification of internal compositional zoning in zircon.

U-Pb Zircon Analysis

Zircons ($ZrSi0_4$) are remarkably robust minerals that do not easily weather and have a high closure temperature (~900° C; Cherniak and Watson, 2000) that permits the crystalline structure to reliably retain radiogenic daughter products produced through time. These properties allow zircons to be reliably used as geochronometers. U-Pb dating

of zircons was used in this study to date the cores and rims of zircon grains in order to constrain their age of crystallization and subsequent metamorphism.

Although the focus of this study is the Bloody Dick gneiss, 3 zircon samples were analyzed from the quartzofeldspathic gneiss (M'Gonigle, 1965) located in Maiden Peak, 20 km southeast of Bloody Dick Canyon, in order to compare and contrast their isotopic properties. Several U-Pb analyses from the Bloody Dick gneiss were recently acquired by Mueller et al. (2016), allowing the current study to focus on 2 samples from the northern and southern portion of the same unit. Therefore, a total of 5 samples were selected for U-Pb analysis in this study.

Target locations selected for U-Pb analysis on specific zircon grains that were carefully selected based on Back-Scattered Electron (BSE) image interpretations of zircon grain morphologies such as cores and rims. In nearly every case, zircon cores were identified by their distinctive zoning, while metamorphic rims appear more homogeneous, lacking such internal zoning, and generally create a more rounded, subhedral crystal surface. If a zircon grain was interpreted as containing a core and a rim, each distinctive phase was targeted for analysis in an attempt to demonstrate differing U-Pb ages between the two. Within each sample, every 30 μm wide laser spot was assigned a unique identification number, starting with 1 and increasing chronologically, followed by the letter C or R, designating each spot as a hypothesized zircon core or a rim. When a rim was not present, the spot was simply assigned the letter C.

U-Pb analysis was completed at the Arizona LaserChron Center at the University of Arizona by Laser Ablation-Inductively Coupled Plasma-Mass Spectrometry (LA-ICP-MS) using a Nu Plasma multicollector mass spectrometer coupled to a New Wave 193

nm ArF laser ablation system equipped with a New Wave SuperCell (Gehrels, 2010). Individual laser ablations were carried out under 6530 mbar, 13.8 kV and each spot was separated by beam train vacuum purge. Each U-Pb spot consisted of 150 laser pulses, forming a 30 μm wide circle. Zircon standards SL (Sri Lanka) and R33 were used to calibrate U-Pb measurements during the analysis.

Following laser ablation, the material was ionized as it passed through the plasma before traveling down a tube and around a ~45° turn. A magnet located on the inside of this turn separates the ionized material according to its mass allowing individual atoms and isotopes to be isolated, collected and counted by the mass spectrometer. The isotopic ratios of $^{206}Pb/^{238}U$, $^{207}Pb/^{235}U$, $^{208}Pb/^{232}Th$ and $^{207}Pb/^{206}Pb$ were then used to determine the crystallization age of the zircon. Each of these hereto mentioned isotopic ratios accumulates at an independent rate based on the half-life of the parent isotope, creating three independent geochronometers contained within the same zircon that can be used to corroborate one another. In the case of $^{207}Pb/^{206}Pb$, the age provided by the ratio of these 2 daughter products is considered to be more reliable for zircons older than 1200 Ma (Martin et al., 2011). See Appendices A and B respectively for annotated BSE images and full U-Pb results.

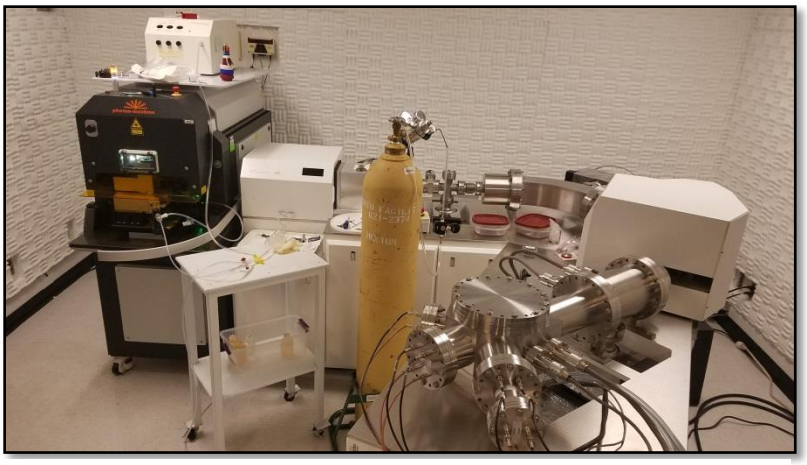

Figure 12: A photo of the Nu ICP-MS at the University of Arizona LaserChron Center on the day it was used for U-Pb analysis of zircons in this study.

Data reduction was completed at the Arizona LaserChron Center using NUagecalc, a Microsoft Excel macro to determine the age and uncertainty of each analysis. Due to the relatively old ages of the 5 samples, the $^{207}Pb/^{206}Pb$ ratio was determined to provide the most reliable ("best fit") age that was subsequently used in the construction of relative probability and concordia plots. Individual zircon spot analyses that produced an error greater than 5%, or were more than 10% discordant were excluded from the results and not used in subsequent interpretations of U-Pb ages. At Idaho State University, a Microsoft Excel macro called Isoplot (Ludwig, 2012) utilized an error input of 2-sigma to construct additional relative probability and linearized probability plots.

Lu-Hf Zircon Isotopic Analysis

Unlike U-Pb dating, which provides a crystallization age of a rock, the Lu-Hf system is used to construct a model age for calculating the time that has elapsed since the material in question was extracted from the earth's mantle. This tool was employed here to permit the identification of isotopically juvenile vs. evolved magmatism, allowing

interpretations to be made regarding the origin of magmatic intrusions. Generally, 5 εHf values from the depleted mantle (DM) are interpreted as isotopically juvenile, εHf values between 5 and -10 are interpreted as intermediate, and values greater than 10 are more isotopically evolved. However, most interpretations of isotopically juvenile vs. evolved magmatism in this work was relative, comparing one sample to another, and making inferences regarding the need to invoke the addition of more isotopically juvenile material as needed to explain observations in the results. ^{176}Lu continually decays into ^{176}Hf, with a half-life of ~35.7 Ga; given that ^{177}Hf is a stable isotope, the ^{176}Hf/^{177}Hf ratio within the mantle is therefore constantly evolving (Bouvier et al., 2008). When material is partially melted and extracted from the mantle, this material becomes relatively enriched in Hf isotopes while most of the Lu remains behind, primarily because of garnet's strong affinity for Lu in mantle rock. The newly differentiated melt now contains very little ^{176}Lu, resulting in a much slower isotopic evolution of its ^{176}Hf/^{177}Hf ratio, while the bulk mantle continues to evolve through time at a high rate. Hf finds its way into the crystalline structure of a zircon ($ZrSiO_4$) because it is often substituted for Zr, which shares a similar ionic charge (+4) and ionic radius. The crystallizing zircon makes no distinction between ^{177}Hf and ^{176}Hf and the final isotopic ratio of Hf within a zircon reflects the Hf ratio contained in the parent material from which the zircon crystallized. By comparing the observed ^{176}Hf/^{177}Hf ratio within a zircon to the mantle's calculated isotopic evolution path, a model age for when that material was extracted from the mantle can be determined (Gehrels, 2012).

One common way that Hf model ages are expressed is in εHf units. This method compares the ^{176}Hf/^{177}Hf ratio of a rock to that of the bulk silicate earth, also known as

the chondritic uniform reservoir (CHUR), derived from the isotopic study of meteorites. The principle states that the isotopic composition of chrondritic meteorites reflects the initial, undifferentiated isotopic composition of the earth given that both formed at the same time, from the same material of our early sun's protoplanetary disk (Bouvier et al., 2008). εHf is defined as $\varepsilon^0Hf = \{[(^{176}Hf/^{177}Hf)^0_{sample} / (^{176}Hf/^{177}Hf)^0_{CHUR}]-1\}x10^4$ and present day values range from +15 to -70 (Gehrels, 2012). Positive εHf values are considered to be juvenile, having been derived directly or nearly directly from the mantle, such as oceanic lithosphere and subduction-related volcanic arcs, which incorporate material from the subducted and partially melted oceanic lithosphere. Negative εHf values, on the other hand, are interpreted as being more evolved, having been derived from the mantle long ago and reworked, melted and recrystallized more recently, producing εHf model ages and U-Pb zircon crystallization ages that may differ by billions of years (Foster et al., 2006). This is most commonly observed in Precambrian cratonic blocks that have had no isotopic interaction with mantle material since their formation, but are still subject to remelting and recrystallization.

Lu-Hf analysis of 4 zircon samples was completed at the University of Arizona LaserChron Center in Tucson in late December, 2016 using the same Nu plasma LA-ICP-MS mentioned previously for U-Pb zircon analysis. Individual laser ablations were carried out at 6528 mbar, 13.6 kV, and each analysis was separated by a 30 second beam train vacuum purge. Each Hf spot consisted of 610 laser pulses forming a circle 50 μm in diameter directly on top of preexisting U-Pb analysis spots. Hf spots were chosen to coincide with U-Pb spots that yielded high concordance, low error and were not located proximal to inclusions or cracks. Hf zircon standards SL (Sri Lanka). R33, MT (Mud

Tank), TEM (Temora), FC, 91500 and PLES (Plesovice) were used to calibrate Hf measurements during the analysis. See Gehrels (2010; 2012) for specific information about these zircon standards and their calibration. Sample 02NA16 was not selected for Hf analysis because of its similar U-Pb age and geographic proximity to sample 03NA16 which was selected for Hf analysis. See Appendix C for full Hf analysis results.

(U-Th)/He Thermochronology Zircon Analysis

The utilization of (U-Th)/He dating provides a useful tool to date thermochronologic events in the geologic past. In this study, the (U-Th)/He system is utilized to determine the amount of time that has passed since the sample in question was exhumed from beneath a certain depth. For this study, one sample in the hanging wall of the Monument fault was analyzed by (U-Th)/He thermochronometry and was hypothesized to establish the timing of thrust-related exhumation in the area.

The radioactive decay of uranium (U) into lead (Pb) involves branching decay via several decay mechanisms, resulting in production of several daughter products; these provide additional opportunities for isotopic analysis beyond common U-Pb zircon dating. See Figure 13 for an illustration of the many steps involved in the decay of ^{238}U into ^{206}Pb.

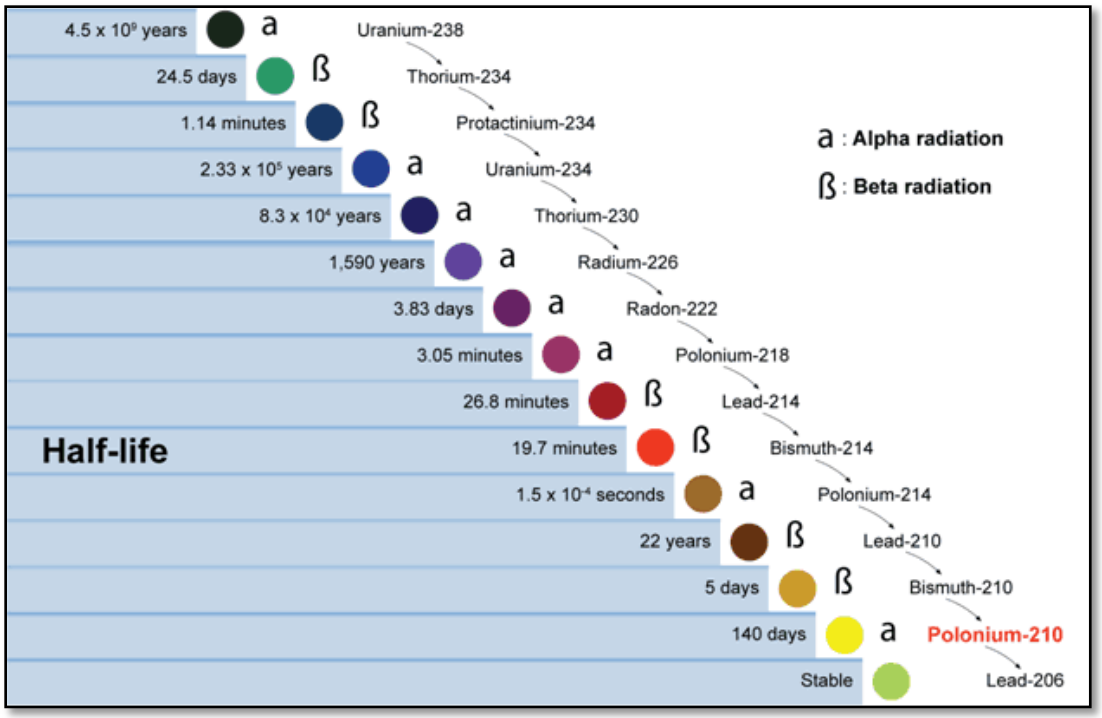

Figure 13: An illustration of decay methods and the respective half-lives of each daughter product produced during the decay of ^{238}U to ^{206}Pb (Canadian Nuclear Safety Commission, 2012).

The half-life of these daughter isotopes ranges from under a second, to a couple hundred thousand years, yet their sum contributes very little to the total ~4.5 billion year half-life of ^{238}U and is well within the typical standard range of error for U-Pb analysis. While the sum of their half-lives may be relatively insignificant, the method by which they decay produces very useful by-products. For example, 8 of the 14 steps concerning the decay of ^{283}U to ^{206}Pb involve α-decay, a radioactive process that ejects a He nucleus—2 protons and 2 neutrons—from a radioactive parent. When this decay takes place within a zircon crystal, the He generally accumulates and its abundance can be measured. However, if the α-decay takes place near the edge of a zircon crystal (17.0 µm for ^{238}U decay, 19.6 µm for ^{235}U, and 19.3 µm for ^{232}Th decay), the resulting He nucleus may be ejected from the crystal (Farley et al., 1996; Hourigan et al., 2005). For this

reason, zircon crystals selected for He analysis must be carefully measured to determine their volume to surface area ratio, which contributes to a factor know as alpha ejection correction (Reiners, 2005).

If the temperature of a rock is above the closure temperature of ~180° C, He can escape from the crystalline structure of a zircon (Reiners et al., 2004). As a rock is exhumed, it passes upward through the natural, surrounding, geothermal gradient and cools as it approaches the surface. Once the surrounding temperature cools below ~180° C, radiogenic He begins to accumulate within the zircon crystal. The known geothermal gradient of a region, combined with (U-Th)/He data, constrains the amount of time that has elapsed since the zircon in question was exhumed above a specific depth and cooled below 180° C (Reiners, 2005).

Six zircons from sample 18NA16 were selected for (U-Th)/He analysis and were measured and sealed in Nb foil packets by Dr. David Pearson at the Idaho State University zircon separation lab before being sent to the University of Arizona for analysis using the methods outlined by Reiners and Nicolescu (2006).

Chapter IV: Results

Description of Map Units

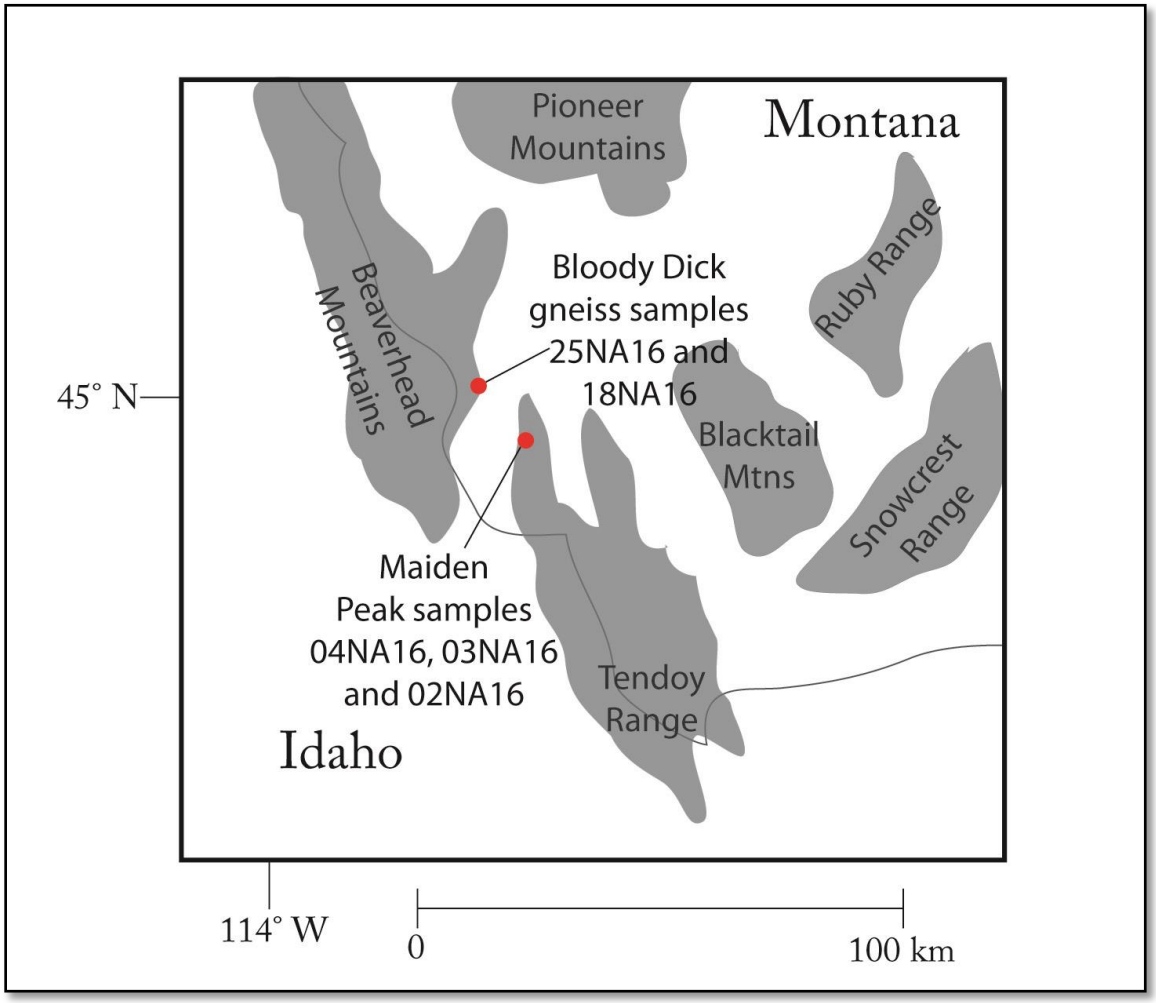

Figure 14: Regional locations of Bloody Dick and Maiden Peak samples.

Maiden Peak

Sample 04NA16 was collected from an outcrop of gneiss southeast of a private ranch called the Mansfield Cow Camp near Jeff Davis peak, part of the greater Maiden Peak area in the northern Tendoy Range (see Table 2 for location). Thin section analysis reveals a relative mineral abundance of 30% quartz, 30% microcline, 20% chlorite, 10% plagioclase and 10% hornblende (See Figure 16 and Table 3).

Figure 15: Quartzofeldspathic gneiss. Maiden Peak 1: Sample 04NA16.

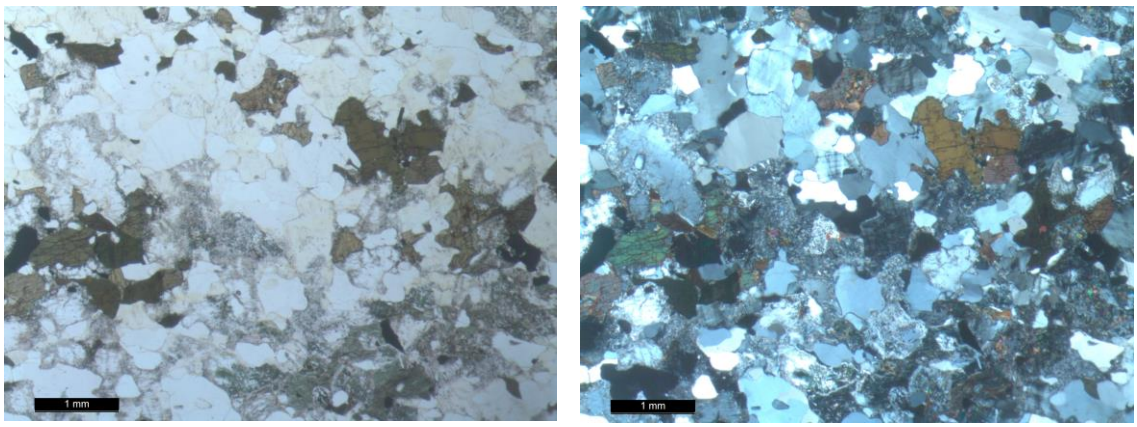

Figure 16: Quartzofeldspathic gneiss. Maiden Peak 1: Sample 04NA16, gneiss in 30 µm thin section. Plane polarized light (left), cross polarized light (right).

Quartzofeldspathic gneiss, Maiden Peak 2, Sample 03NA16:

This sample of moderately foliated, quartzofeldspathic gneiss that was collected from an extensive outcrop and boulder field of gneiss within the Beaverhead-Deerlodge National Forest, southwest of Jeff Davis peak and east of the Chinatown placer mine (see Table 3 for location). Thin section analysis reveals a relative mineral abundance of 40% microcline, 20% quartz, 20% chlorite, 15% plagioclase and 5% calcite in a small vein (See Figure 18 and Table 3).

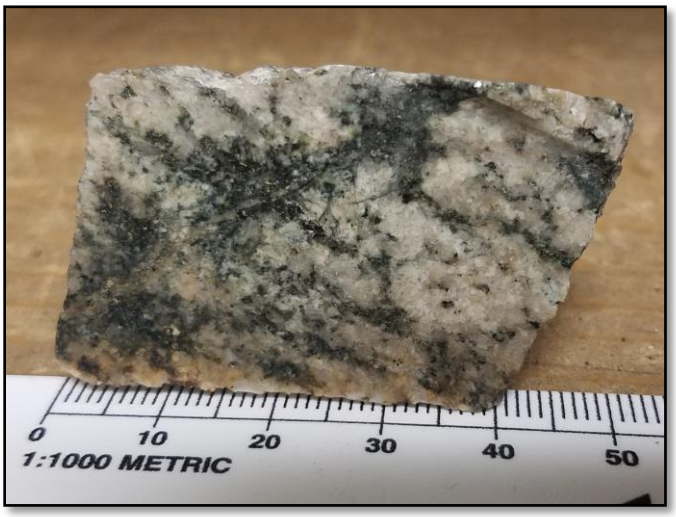

Figure 17: Quartzofeldspathoc gneiss. Maiden Peak 2: Sample 03NA16.

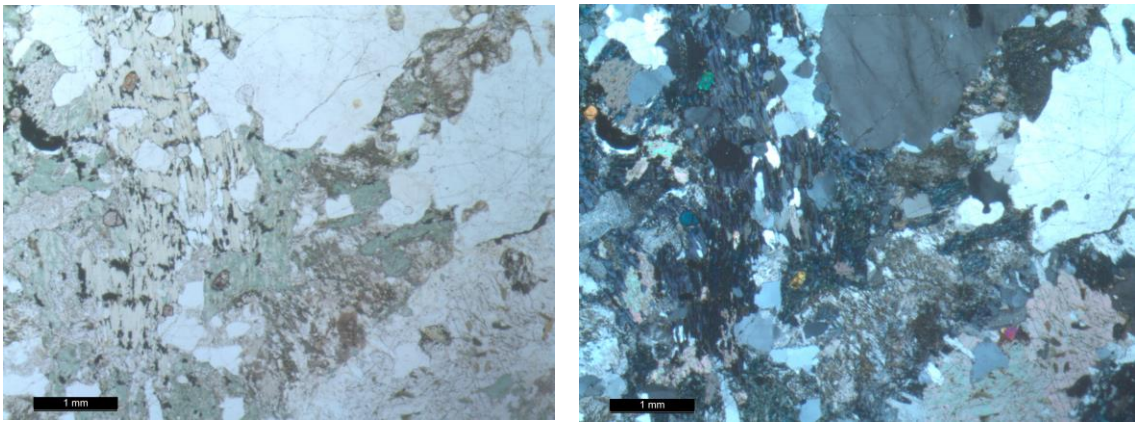

Figure 18: Quartzofeldspathic gneiss. Maiden Peak 2: Sample 03NA16, quartzofeldspathic gneiss in 30 µm thin section. Plane polarized light (left), cross polarized light (right).

Quartzofeldspathic gneiss, Maiden Peak 2, Sample 02NA16:

Sample 02NA16 was collected from a small, 10 meter wide, 1 meter high outcrop of dark grey colored, weakly foliated gneiss exposed in a road cut within the Beaverhead-Deerlodge National Forest, southwest of Jeff Davis peak and east of the Chinatown placer mine (see Table 2 for location). Thin section analysis reveals a relative mineral abundance of 40% plagioclase, 40% hornblende and 20% biotite (See Figure 20 and Table 3).

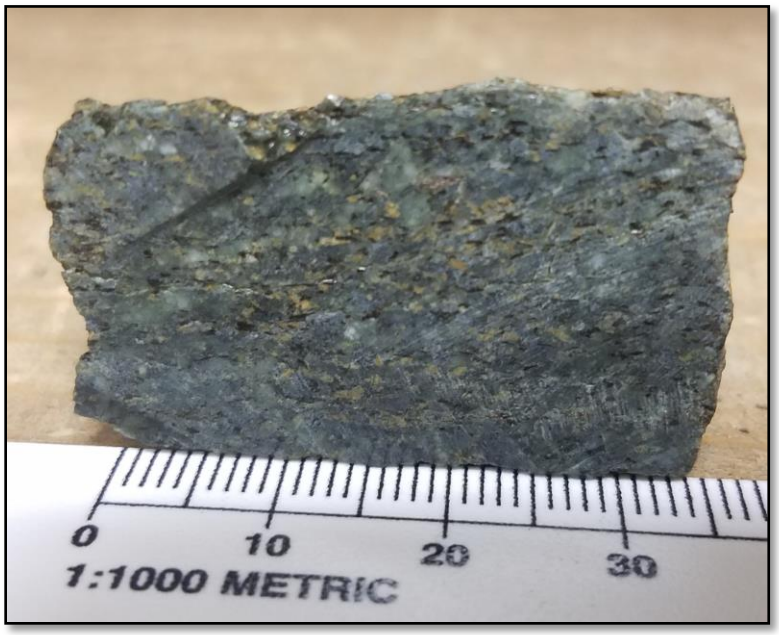

Figure 19: Quartzofeldspathic gneiss. Maiden Peak 2: Sample 02NA16, gabbroic gneiss.

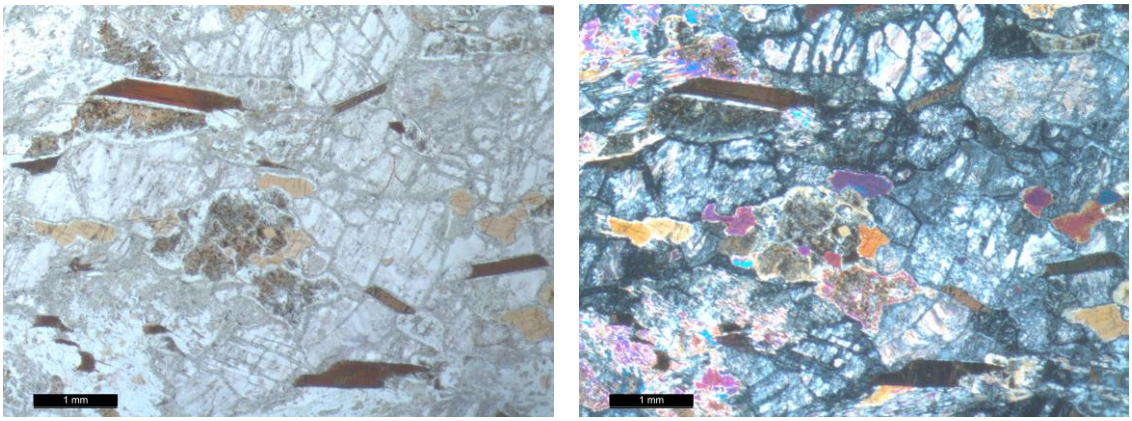

Figure 20: Quartzofeldspathic gneiss. Maiden Peak 2: Sample 02NA16, gabbroic gneiss in 30 µm thin section. Plane polarized light (left), cross polarized light (right).

Bloody Dick Gneiss

Within the Bloody Dick gneiss, 4 map units have identified based on their respective lithology and are presented below in order of decreasing age (see below for isotopic results). These units include:

1. Xgb, banded gneiss, ca. 2476 Ma.
2. Xgh, hornblende gneiss, ca. 1878 – 1900 Ma.
3. Xga, augen gneiss, ca. 1800 – 1900 Ma.
4. Xfg, felsic gneiss, 1802 ± 17 Ma.

Xgb. Banded Gneiss of Bloody Dick Creek

This unit contains well defined, compositional bands up to 1 cm thick containing quartz, plagioclase, biotite and hornblende. Feldspar augen are typically <5 mm in diameter, but one was found to be 2 cm in diameter. This unit is exposed in the southern portion of the Bloody Dick gneiss and is unconformably overlain by rocks of the Eocene Challis Volcanic Group (Tc) and Middle Eocene to Oligocene Bear Creek beds (Tbc) across its southeastern margin. The banded gneiss' contact with the hornblende gneiss is difficult to constrain and poorly exposed.

Sample 25NA16 was collected from an outcrop of highly foliated, banded gneiss along a southwest facing hillside near the southern margin of the Bloody Dick gneiss (see Table 3 for location). Thin section analysis reveals a quartzofeldspathic mineral assemblage of 50% quartz, 25% biotite, 20% plagioclase and 10% hornblende (See Table 4).

Figure 21: Bloody Dick gneiss, banded gneiss (Xgb), sample 25NA16.

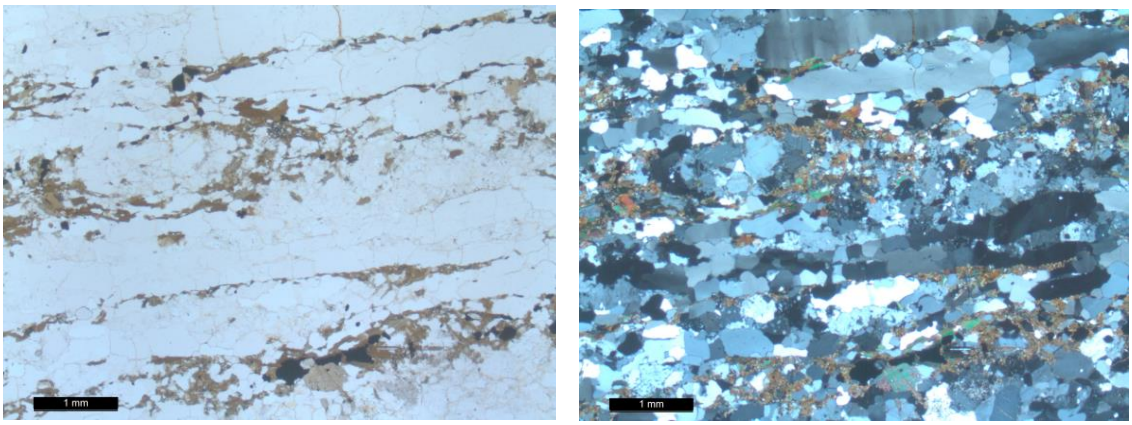

Figure 22: Bloody Dick gneiss, banded gneiss (Xgf), sample 25NA16, gneiss in 30 µm thin section. Plane polarized light (left), cross polarized light (right).

Xgh. Hornblende Gneiss of Bloody Dick Creek

The hornblende gneiss is a moderately foliated, blocky, dark grey to black rock with ~75% hornblende and a minor component of plagioclase and quartz. The hornblende fine grained with a greasy texture. This unit often contains veins of plagioclase that vary widely in abundance and spatial distribution throughout the unit but generally become

more prevalent to the northeast near the contact with the augen gneiss unit (Xga). Some veins contain plagioclase augen 3-6 mm in diameter. At least 2 small, >1 m^2, isolated bodies of biotite schist (05NA16; Figure 25) were also observed within the hornblende gneiss unit, though several more of them are contained within the augen gneiss. The hornblende gneiss was sampled for U-Pb analysis by Mueller et al. (2016) (BDC4 and BDC5). See U-Pb and Hf Results below.

Figure 23: Bloody Dick gneiss, hornblende gneiss (Xgh). This particular outcrop contains no visible plagioclase bands or augen.

Thin section analysis of mineral composition varies by location depending on the local abundance of plagioclase veins and augen. A typical mineral abundance is observed in sample 20NA16 which contains 75% hornblende, 15% plagioclase and 10% quartz (See Figure 24 and Table 3).

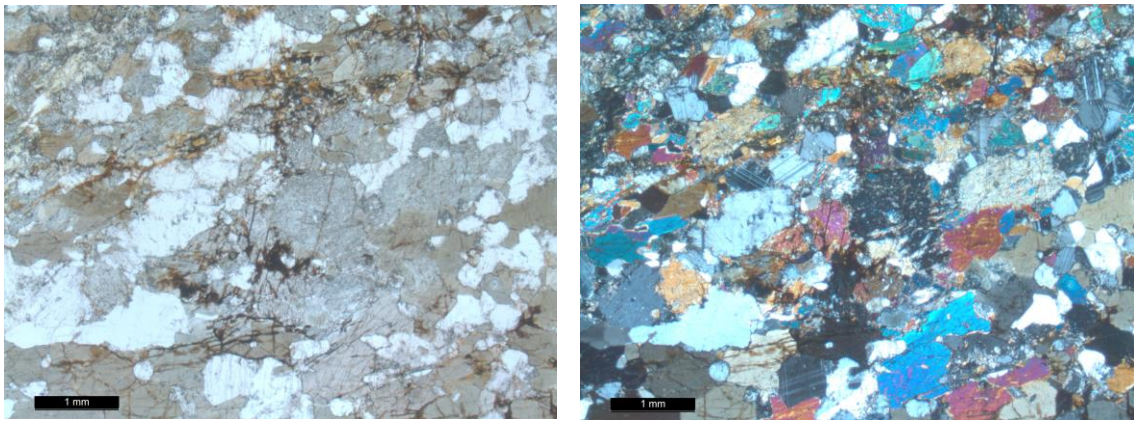

Figure 24: Bloody Dick gneiss, hornblende gneiss (Xgh), sample 20NA16, in 30 µm thin section. Plane polarized light (left), cross polarized light (right).

Xga. Augen Gneiss of Bloody Dick Creek.

North of Bloody Dick Creek, the augen gneiss makes up more than 70% of the Bloody Dick gneiss and is dominated by the presence of 3-6 mm wide plagioclase augen and 3-10 mm wide veins of quartz and plagioclase. Cross cutting relationships suggest that this unit is a highly intruded, migmatized portion of the heretofore-described hornblende gneiss. Inclusions of 10-30 cm wide hornblende gneiss are common and particularly well exposed in an exploratory trench (45.004246° N, 113.347227° W, 7310') dug perpendicular to the ridgeline. The spatial distribution of the augen gneiss is weakly constrained and its southern contact with the hornblende gneiss is highly gradational and variable. Likewise, its contact with the felsic gneiss to the north is similarly gradational. In some locations the contact with the felsic gneiss quickly grades over a 2-4 meter distance, while in other localities the felsic intrusions gradually become more common over a distance of 20-60 meters, eventually dominating the lithology. The augen gneiss was previously sampled for U-Pb zircon analysis by Mueller et al. (2016) (BDC-2 and BDC-6; see U-Pb and Hf Results below) who utilized XRF to determine

elemental geochemistry and classified sample BDC-2 as schist with the following explanation: “BDC-2 (schist) probably has a metavolcanic or metavolcaniclastic protolith that experienced significant alteration (or weathering), which led to increased relative concentrations of Al and Fe and lower Si relative to a typical calc-alkaline composition.”

Small (<1 m^2), isolated exposures of biotite schist were located in at least 3 locations throughout the augen gneiss and its gradational contact with the hornblende gneiss. Sample 05NA16 was collected from one of these exposures of schist and has a relative mineral abundance of 60% biotite, 30% quartz, 5% plagioclase and a small fracture containing calcite that makes up an additional 5%.

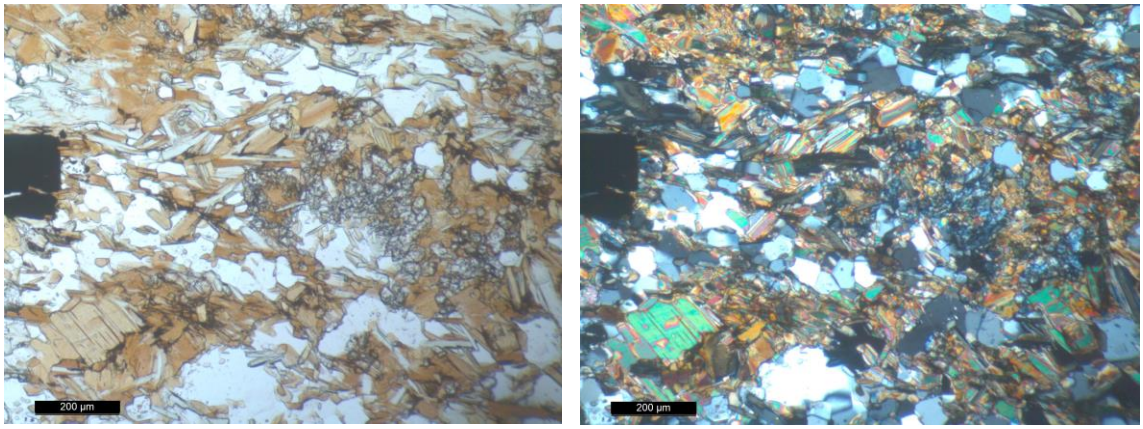

Figure 25: Bloody Dick gneiss, augen gneiss (Xga), schist body, sample 05NA16, in 30 µm thin section. Plane polarized light (left), cross polarized light (right).

Figures 26a and 26b: Bloody Dick gneiss, augen gneiss unit (Xga). The image on the left shows an inclusion of the hornblende gneiss (Xgh) within the augen gneiss. The image on the right shows common size and distribution of the plagioclase sills within the augen gneiss.

Thin section analysis of mineral composition varies by location depending on the local abundance of plagioclase veins, augen and proximity to the felsic gneiss (Xgf) into which it grades. A typical mineral abundance is observed in sample 06NA16 which contains 35% plagioclase, 30% biotite, 20% quartz and 15 % garnet (See Figure 27 and Table 3).

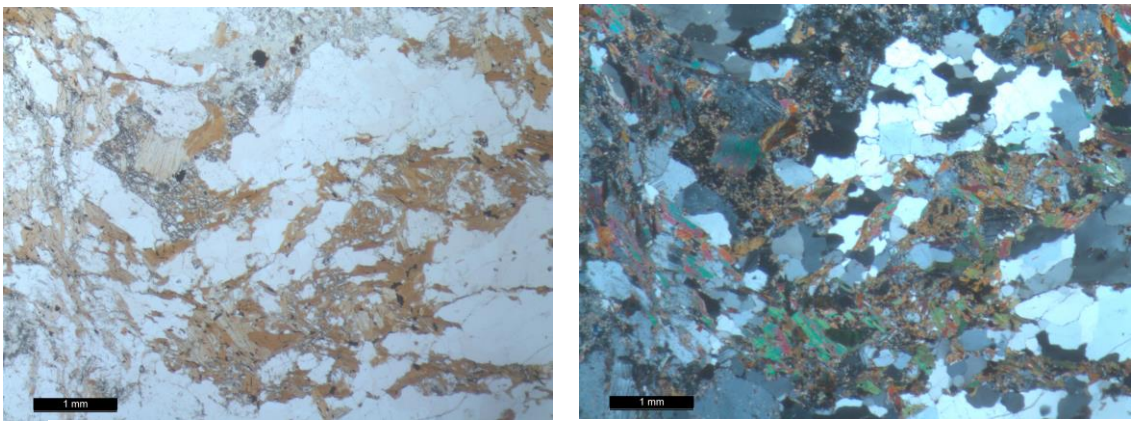

Figure 27: Bloody Dick gneiss, augen gneiss (Xga), sample 06NA16, in 30 µm thin section. Plane polarized light (left), cross polarized light (right).

Xgf. Felsic Gneiss of Bloody Dick Creek.

The highly foliated felsic gneiss is exposed along the northern edge of the Bloody Dick gneiss in a 200 meter wide, 1700 meter long body that is truncated by the Monument fault along the northeast margin of the Bloody Dick gneiss (see geologic map, Plate 1). This unit has a highly gradational contact with the adjacent augen gneiss, however the gradation is only ~5 meters wide near the top of Sullivan Gulch (45.010196° N, 113.347628° W, 7185') and is well exposed. Northwest of Sullivan Gulch the contact is much more gradational and can be up to 50 meters wide. The felsic gneiss is composed primarily of quartzofeldspathic minerals, biotite, chlorite and 2-5 mm wide feldspar augen. Thin section analysis of sample 18NA16 reveals a relative mineral abundance of 35% plagioclase, 35% quartz, 25% biotite, and 5% chlorite (See Figure 29 and Table 3).

Figure 28: The Bloody Dick gneiss, felsic gneiss (Xgf), sample 18NA16 .

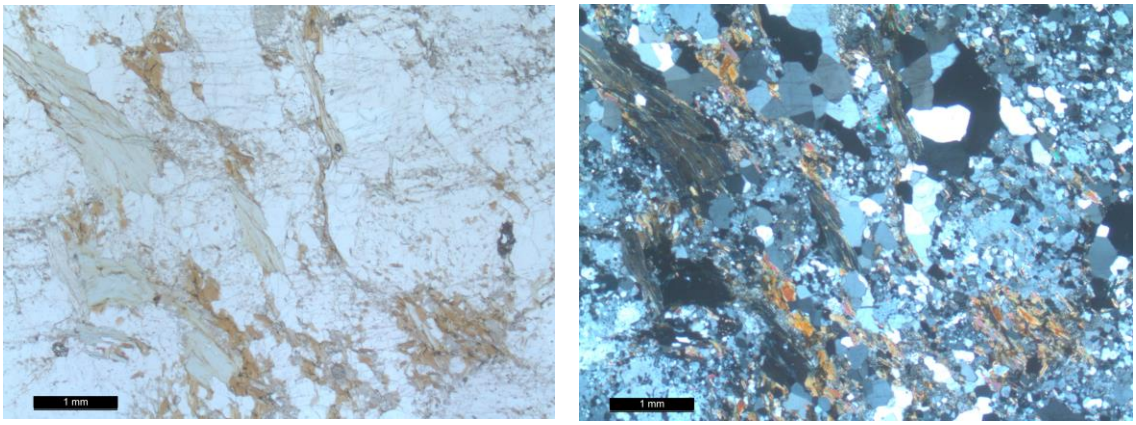

Figure 29: Bloody Dick gneiss, Felsic gneiss (Xgf), sample 02NA16, in 30 µm thin section. Plane polarized light (left), cross polarized light (right).

Miscellaneous Lithologies

Individual outcrops within the Bloody Dick gneiss do not always fit well into one of the above 4 units and are interpreted as being transitional between two units. This is particularly true within the augen gneiss, which varies in lithology and grain size between the hornblende gneiss and felsic gneiss. Constraining the spatial distribution of each unit incorporated dozens of observations to identify large-scale patterns.

A non-foliated diabase intruded the eastern strand of the Beaverhead Divide Fault (ESBDF) (Lonn et al., 2016) and an aphanitic basaltic flow/intrusion covers the diabase, the Bloody Dick gneiss, and the juxtaposed quartzite of the Jahnke Lake member of the Apple Creek Formation.

Thin section analysis of the diabase, sample 26NA16, reveals a relative mineral abundance of 50% hornblende, 30% plagioclase and 20% chlorite (See Figure 30 and Table 4).

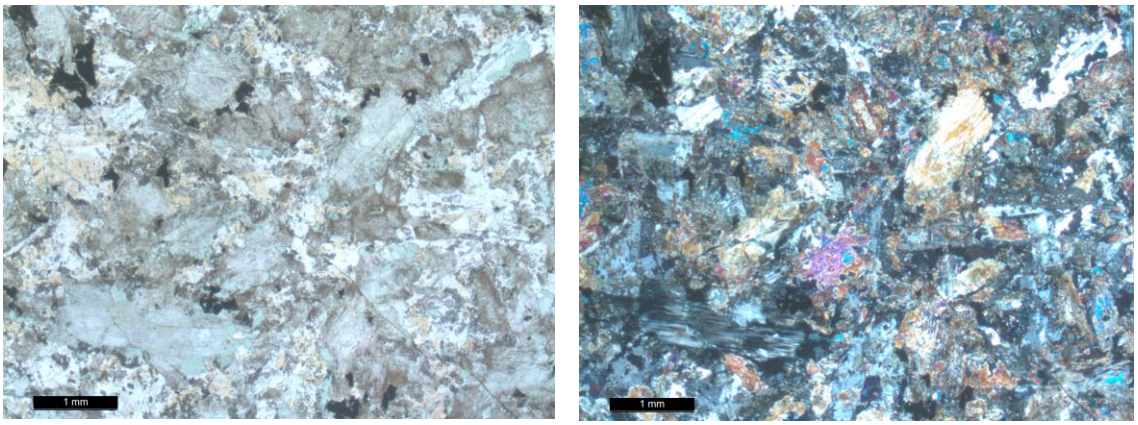

Figure 30: Fault diabase, sample 26NA16, in 30 µm thin section. Plane polarized light (left), cross polarized light (right).

Sample ID	UTM Easting (Z12)	UTM Northing (Z12)	Lat. (north)	Long. (west)	Elev. (ft)	Map Unit	Analysis
01NA16	31600	498621	45.0055	113.3347	7050	Xga	Thin Section
02NA16	32882	497174	44.8786	113.1673	7885	MP2	Thin Section, U-Pb
03NA16	32902	49720	44.8818	113.1648	7830	MP2	Thin Section, U-Pb, Lu-Hf
04NA16	32861	49754	44.9115	113.1712	8195	MP1	Thin Section, U-Pb, Lu-Hf
05NA16	31431	49857	45.0008	113.3560	6470	Xga	Thin Section
06NA16	31431	49857	45.0008	113.3560	6470	Xga	Thin Section
08NA16	31643	49855	45.0001	113.3291	6650	Xga	Thin Section
09NA16	31606	49855	44.9999	113.3338	6784	Xga	Thin Section
11NA16	31572	49855	44.9999	113.3381	7079	Xga	Thin Section
12NA16	31572	49855	44.9999	113.3381	7079	Xga	Thin Section
14NA16A	31579	49865	45.0083	113.3375	7091	Xga	Thin Section
14NA16B	31579	49865	45.0083	113.3375	7091	Xga	Thin Section
17NA16	31431	49857	45.0008	113.3560	6470	Xgh	Thin Section
18NA16	31500	49867	45.0102	113.3476	7185	Xgf	Thin Section, U-Pb, Lu-Hf, (U-Th)/He
19NA16	31502	49861	45.0044	113.3472	7259	Xga	Thin Section
20NA16	31539	49851	44.9958	113.3420	6500	Xgh	Thin Section
21NA16	31563	49836	44.9828	113.3385	6685	Xgh	Thin Section
22NA16	31537	49842	44.9878	113.3420	7052	Xgb	Thin Section
23NA16	31537	49842	44.9878	113.3420	7052	Xgb	Thin Section
25NA16	31505	49829	44.9758	113.3456	7003	Xgb	Thin Section, U-Pb, Lu-Hf
26NA16	31475	49835	44.9809	113.3496	6860	Tgd	Thin Section

Table 2: Sample locations. Map units MP1 and MP2 indicated the sample was collected from the Maiden Peak area and are not a unit within the map of the Bloody Dick gneiss. Also see Appendix B for locations.

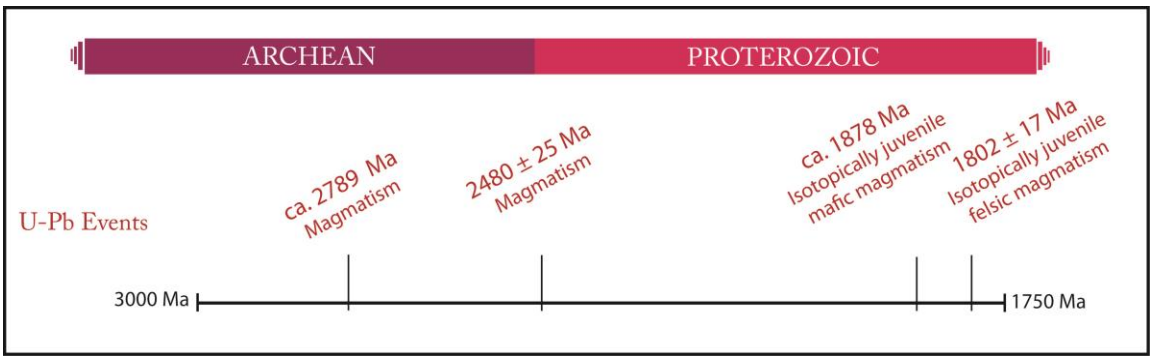

Figure 31: Timeline of events derived from U-Pb and Lu-Hf isotope analysis of zircons from the Bloody Dick gneiss and the quartzofeldspathic gneiss near Maiden Peak.

General Petrographic Results

A total of 21 thin sections aided in the identification of mineral abundances and deformational features. This helped associate individual samples with one of the 4 units in the Bloody Dick gneiss described above. A table of relative mineral abundances has been compiled below (Table 4). Images of each thin section are included in Appendix D.

Mineral assemblages

Samples collected from the Bloody Dick gneiss and from the Maiden Peak area contain mineral assemblages that generally fit into two categories:

1. Quartzofeldspathic gneiss containing abundant, coarse-grained microcline and plagioclase feldspar, quartz, hornblende and biotite with minor components of chlorite and garnet. Minor calcite veins are also present. This includes samples 04NA16 and 03NA16 from Maiden Peak and map units Xgb (banded gneiss), Xga (augen gneiss) and Xgf (felsic gneiss) from the Bloody Dick gneiss.

2. Hornblende gneiss with >75% hornblende and plagioclase veins that often contain 3-6 mm wide plagioclase augen. This includes map unit Xgh (hornblende gneiss) and sample 02NA16 from Maiden Peak.

Sample	Map Unit	Quartz %	Plagioclase %	Microcline %	Biotite %	Hornblende %	Calcite %	Chlorite %	Garnet %	Rock name
01NA16	Xga	30	50		20					Tonalite
02NA16	MP2		40		20	40				Gabbroic gneiss
03NA16	MP2	20	15	40			5 (vein)	20		Quartzofeldspathic gneiss
04NA16	MP1	30	10	30		10		20		Quartzofeldspathic gneiss
05NA16	Xga	30	5		60		5 (vein)			Plagioclase-Quartz-Biotite Schist
06NA16	Xga	20	35		30				15	Garnet-quartz-biotite-plagioclase gneiss
08NA16	Xga	35	35		30					Biotite-quartz-plagioclase gneiss
09NA16	Xga	50	15		30			5		Chlorite-plagioclase-biotite-quartz gneiss
11NA16	Xga	90	9		1					Quartz vein
12NA16	Xga	30	30		35			5		Chlorite-quartz-plagioclase-biotite gneiss
14NA16A	Xga	30				40	10 (vein)	20		Fault gouge
14NA16B	Xga	10				30	60			Calcified fault gouge
17NA16	Xabd	40	50				10 (vein)			Quarts-plagioclase gneiss
18NA16	Xgf	35	35		25			5		Biotite-quartz-plagioclase gneiss
19NA16	Xga	30	40		30					Biotite-quartz-plagioclase migmatite
20NA16	Xgh	10	15			75				Plagioclase-quartz-hornblende gneiss
21NA16	Xgh	15	5			80				Plagioclase-quartz-hornblende gneiss
22NA16	Xgb	40	10	15	20	10		5		Chlorite-biotite-hornblende-feldspathic-quartz gneiss
23NA16	Xgb	40	20	5	25	5		5		Chlorite-biotite-hornblende-feldspathic-quartz gneiss
25NA16	Xgb	50	20		25	5				Chlorite-biotite-hornblende-feldspathic-quartz gneiss
26NA16	Tgd		30			50		20		Diabase

Table 3: Relative mineral abundances observed in thin section with associated rock name and map unit (Plate 1). Map units MP1 and MP2 indicated the sample was collected from the Maiden Peak area and are not a unit within the map of the Bloody Dick gneiss.

General Observations

Calcite

Calcite veins are observed in 4 samples (03NA16, 05NA16, 14NA16A and 17NA16) and calcite makes up 60% of the relative mineral abundance in sample 14NA16B.

Clinozoisite

Sample 14NA16A was collected from an exploratory pit directly on the Monument fault and contains approximately 10% pale blue minerals in thin section, which is interpreted to be clinozoisite (See Appendix D), a low-grade metamorphic mineral in the epidote group that forms in the presence of free calcium (Winkler, 2013). Sample 14NA16B contains 60% calcite and was collected only 2 meters away and 14NA16A contains 10% calcite itself. The low-grade metamorphic conditions required to form clinozoisite may have resulted from retrograde metamorphism during fluid flow along the Monument fault.

U-Pb and Lu-Hf Results

A total of 5 samples were selected for U-Pb and Hf zircon analysis. Within the Bloody Dick gneiss, 2 samples were selected for U-Pb analysis and 3 samples of gneiss were selected from the Maiden Peak. Sample 02NA16 was excluded from Hf analysis due to its similar U-Pb age and close geographic proximity to sample 03NA16. See Table 3 for sample locations. All analyses with greater than 10% discordance were not used in the construction of concordia plots, probability density functions or age determinations. See Appendix A for annotated BSE images of each zircon sample, Appendix B for full

U-Pb results and Appendix C for full Hf results. The following samples have been grouped into their respective map units and are introduced in decreasing age.

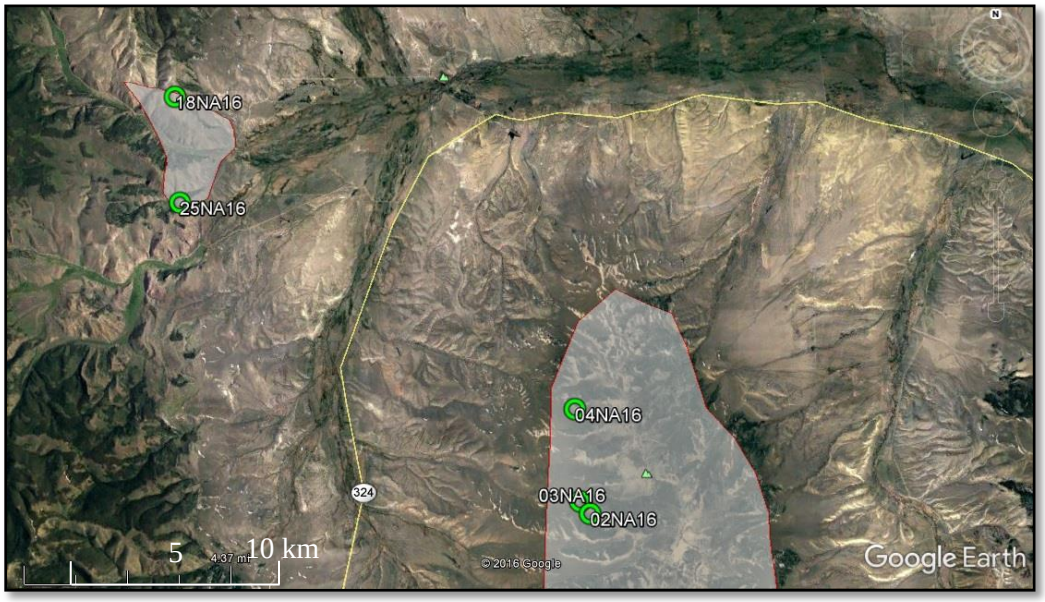

Figure 32: Satellite map of samples selected for U-Pb and Hf analysis (Google Earth, 2017).

Maiden Peak

U-Pb analysis of the 3 zircon samples from the quartzofeldspathic gneiss in the Maiden Peak area produced 2 distinct age populations that will be used herein to categorize these 3 samples into 2 geochronologic units. The first unit is Maiden Peak 1 and contains the oldest zircon sample 04NA16. The second unit is Maiden Peak 2, composed of the two younger zircon samples 02NA16 and 03NA16. These 3 samples are discussed here in the order of decreasing age.

Quartzofeldspathic Gneiss, Maiden Peak 1, Sample 04NA16:

U-Pb zircon analysis of sample 04NA16 utilized a sample size of 38, of which no analyses were found to be greater than 10% discordant and the results indicate the presence of two distinct U-Pb ages. The older population of ages yielded a weighted mean age of ca. 2789 (Figure 33), and was obtained from igneous zircon cores as interpreted from BSE images and for simplicity is referred to in this study as Maiden Peak Population 1 (MP1). Zircon domains that yielded these ages display oscillatory zoning observed in BSE images, U/Th ratio <10, a unimodal crystallization age peak at ca. 2789 Ma, and a quartzofeldspathic mineral composition (See Description of Map Units above). BSE images show that approximately half of the cores also appear to have distinct rims dated to ca. 2497 Ma. The zircon rims do not display zoning and are visually homogeneous in BSE images. The boundary between these two morphological domains is often ambiguous and frequently distorted in a way that appears irregular and contorted. This often made it difficult to discern between cores and rims when choosing the locations for spot analyses. This resulted in an unfortunate number of U-Pb spot analyses that are thought to have overlapped morphological domains, producing several false U-Pb ages (Figure 33) that are interpreted to reflect a mixture of the isotopic ratios between the older cores and younger rims. See Figure 34 for a linearized probability plot that was used to help form this interpretation for mixed ages. Individual zircon grains are subhedral to subrounded, a curious observation for an orthogneiss.

Among the younger (ca. 2497 Ma) zircon rims, 7 of them were found to have U/Th ratios greater than 10. See Figure 35 for an annotated BSE image of zircon grain 17 displaying 2 morphological domains.

Hf analysis of sample 04NA16 reveals two distinct isotopic populations. One temporally associated with the older zircon cores and another, more isotopically juvenile population associated with the zircon rims. The younger zircon population has a higher initial εHf value (+1 to -3) than the projected Hf model age of the ca. 2789 zircons.

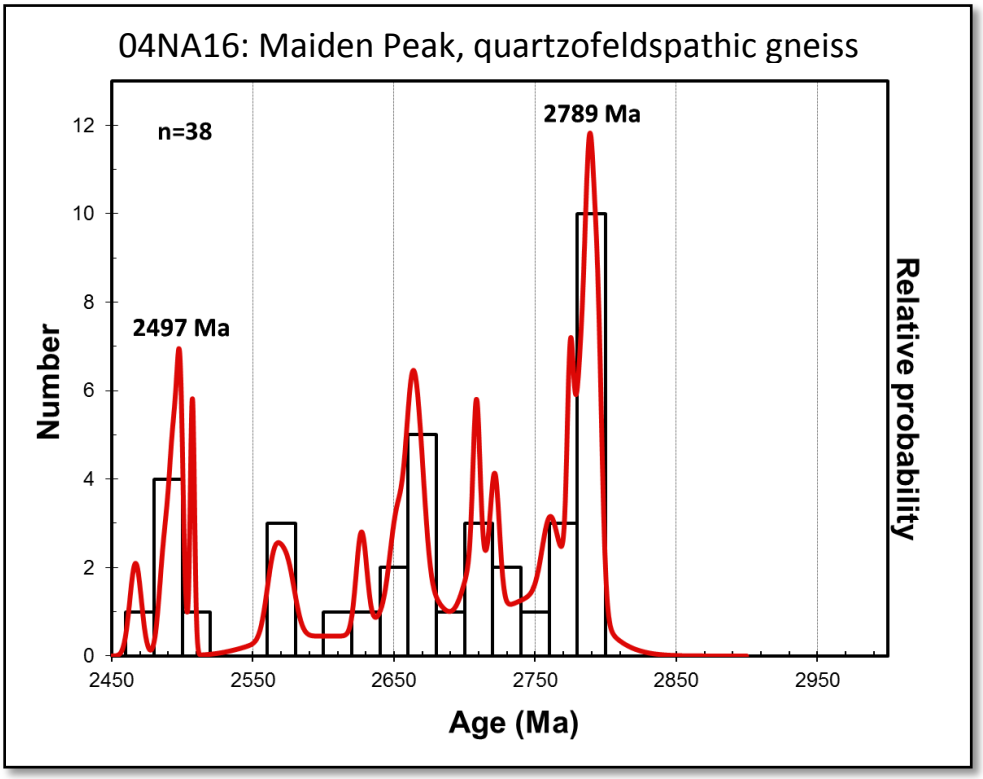

Figure 33: Sample 04NA16 contains two primary U-Pb age peaks at ca. 2789 Ma and ca. 2497 Ma. Smaller peaks between them and interpreted as being the result of spot analyses overlapping age domains within zircon grains. Zircon grain morphologies within this sample were irregular and difficult to interpret. A linearized probability plot aided in this interpretation (see Figure 34). The x-axis represents age (Ma) and the y-axis represents the number of grains. The red curve represents a probability density function associated with the age and error of each analysis. The height of the black boxes corresponds to the absolute number of zircon grains that fall within its age parameters. Analyses with >10% discordance were excluded.

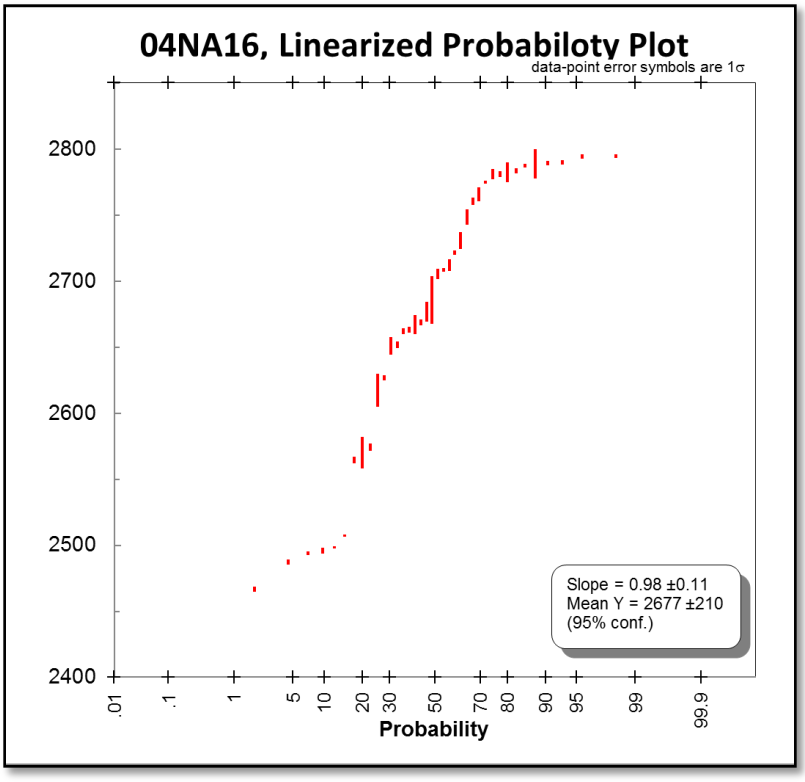

Figure 34: Linearized probability plot constructed from the age and error (Ma) from each analysis. This plot is helpful in differentiating unique zircon age populations from those of mixed domains. A mixed domain occurs when the analysis spot overlaps zircon domains of different ages, producing an apparent age that is a mixture of the two, distinct domains. Each red line represents the age and error (Ma) of an individual analysis. Red lines that plot at shallower slopes suggest zircons of the same age population. This linearized probability plot is interpreted as indicating the presence of two age domains located at the top and bottom of this plot.

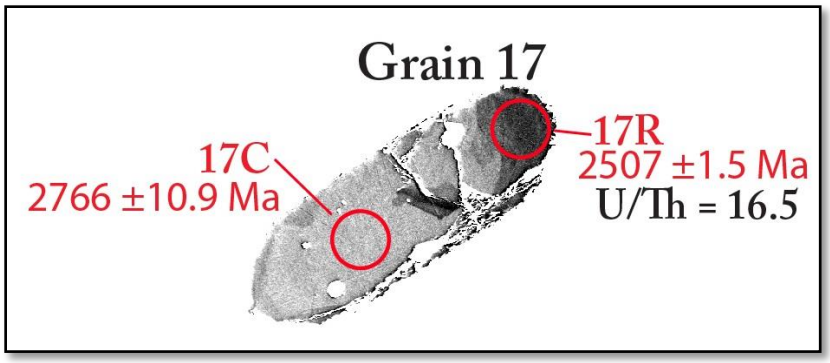

Figure 35: Backscattered electron (BSE) image of grain 17 from sample 04NA16 showing two distinct domains. The zircon core produced a U-Pb age of 2766 ± 10.9 Ma with a partial rim dated to 2507 ± 1.5 Ma. The rim analyses yield high U/Th ratios.

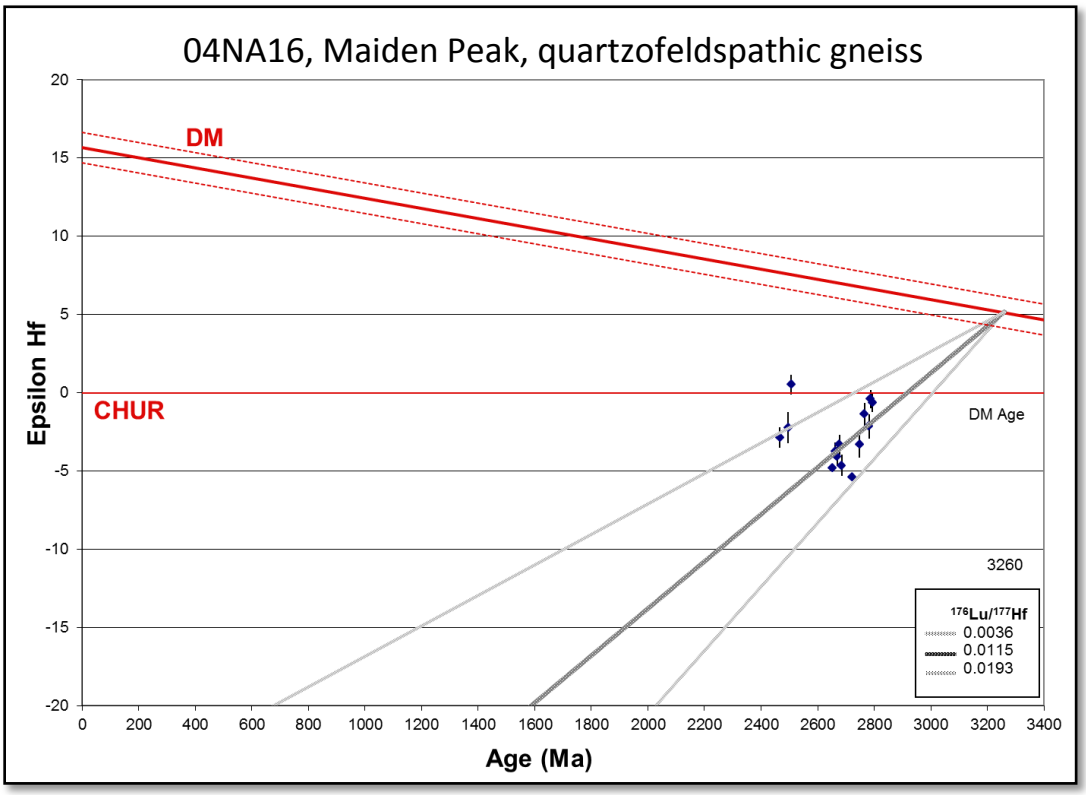

Figure 36: Hf analysis for sample 04NA16 with a Hf model age of 3260 Ma.

Quartzofeldspathic Gneiss, Maiden Peak 2, Sample 03NA16:

With 3 U-Pb analyses greater than 10% discordant from a sample size of 29, sample 03NA16 produced a single U-Pb zircon age of 2483 ± 23 Ma, referred to in this study as Maiden Peak Population 2. BSE images show oscillatory zoning within the subhedral zircon crystals, U-Pb analysis was unable to confirm any significant age difference between zircon cores and rims (Appendix B).

One anomalous zircon analysis (03NA16-2C) produced a U-Pb age date of 1804 ± 11.4 Ma, but was also 16.8% discordant and was therefore not included in the concordia plot or mean age calculation. Another analysis location on this same zircon grain (03NA16-2R; a hypothesized rim) was also found to be greater than 10% discordant.

Hf analysis of 10 zircon grains produced a spread of initial εHf values that range from +2 to -3 (Figure 38).

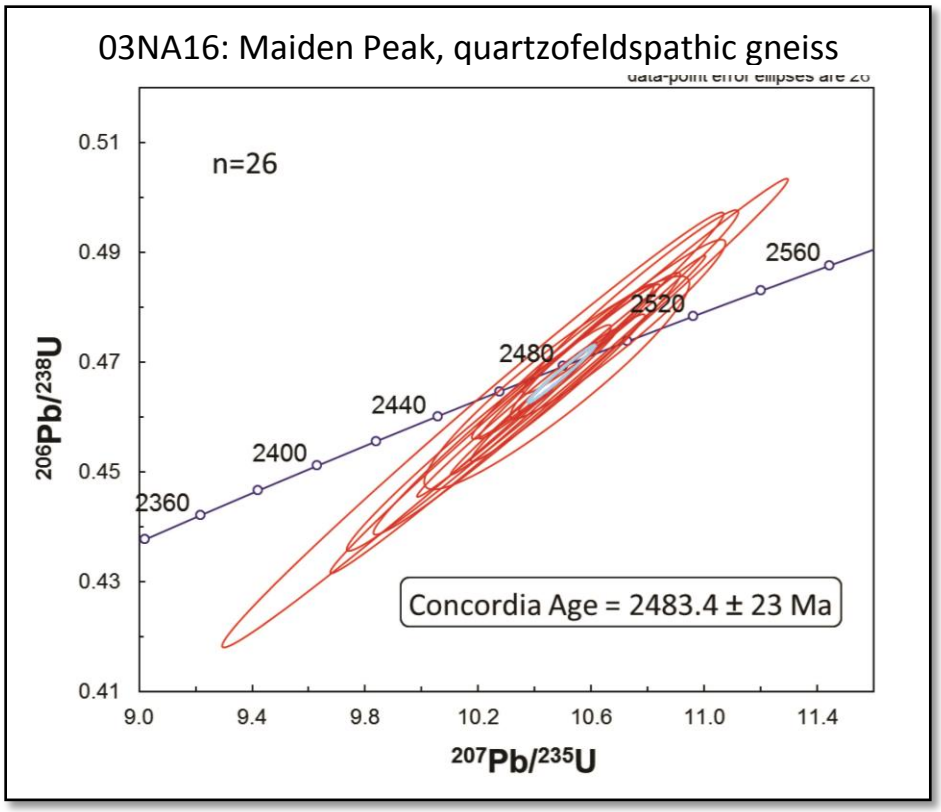

Figure 37: Concordia plot of sample 03NA16. U-Pb zircon analysis reveals a single zircon crystallization age of 2483.4 ± 23 Ma. Red ellipses represent the 2σ error for individual analyses. The blue ellipse is the average age and associated error of all analyses. The width of the A and B axes of this ellipse represent the degree of error. The location where this ellipse crosses the darker blue line is the Concordia age. Analyses with >10% discordance were excluded.

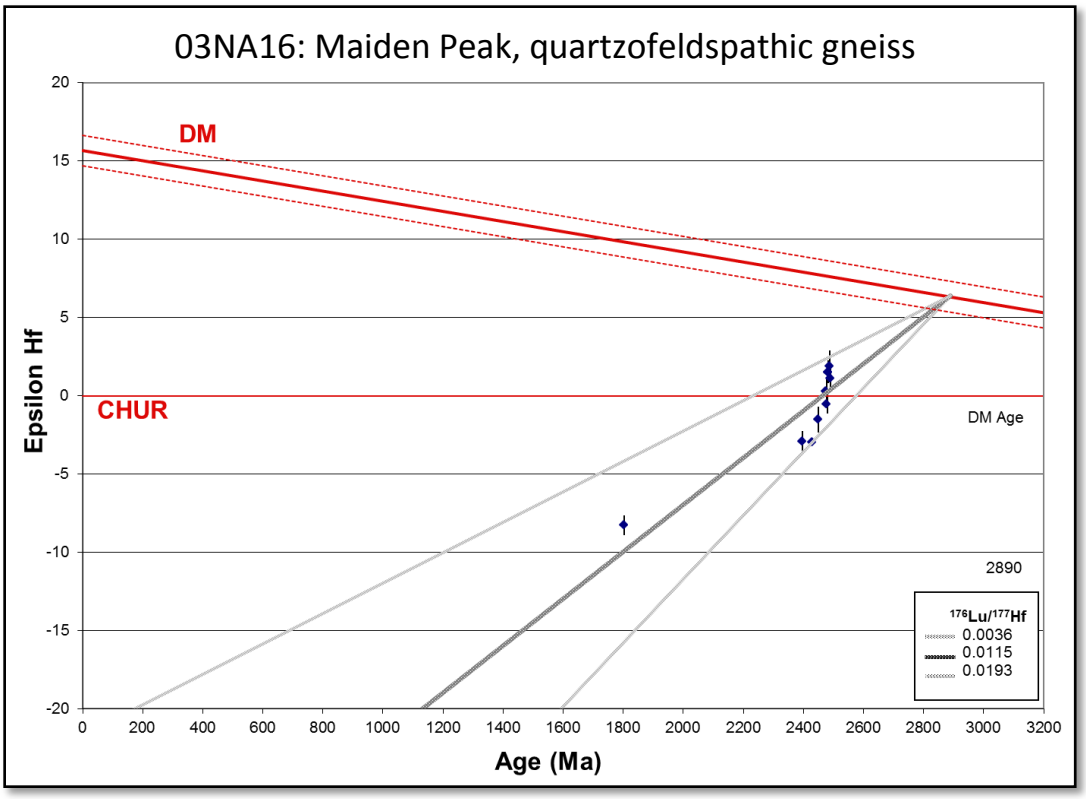

Figure 38: Hf analysis for sample 03NA16 shows 1 isotopic population with an εHf value between +2 and -3, ca. 2480 Ma. One analysis returned an initial εHf value of -8 at 1804 Ma, possibly reflecting new zircon growth at that time derived from the surrounding material.

Quartzofeldspathic Gneiss, Maiden Peak 2, Sample 02NA16:

Sample 02NA16 was selected for 30 spot analyses, of which, 2 spots from a single zircon were found to be greater than 10% discordant. The remaining 28 grain analyses were used to calculate a concordia age of 2477 ± 25 Ma (figure 39) referred to in this study as Maiden Peak Population 2, along with sample 03NA16 as they share the same age. While these two samples were collected only 300 meters apart, sample 02NA16 was selected for U-Pb analysis because it contained an unusual abundance of biotite and hornblende, an attribute that set it apart from other samples collected in the Maiden Peak area (see Petrographic Results below). Like sample 03NA16, note that the age of sample 02NA16 falls within the zircon rim associated age peak measured in sample 04NA16.

BSE images reveal oscillatory zoning within the zircon crystals; however, many of the zircons are highly fractured making morphological boundaries difficult to identify. A few potential core and rim domains were identified, but U-Pb analysis found no significant difference in the ages between them.

This sample was not selected for Hf analysis because of its geographic proximity and similar U-Pb zircon date to sample 03NA16.

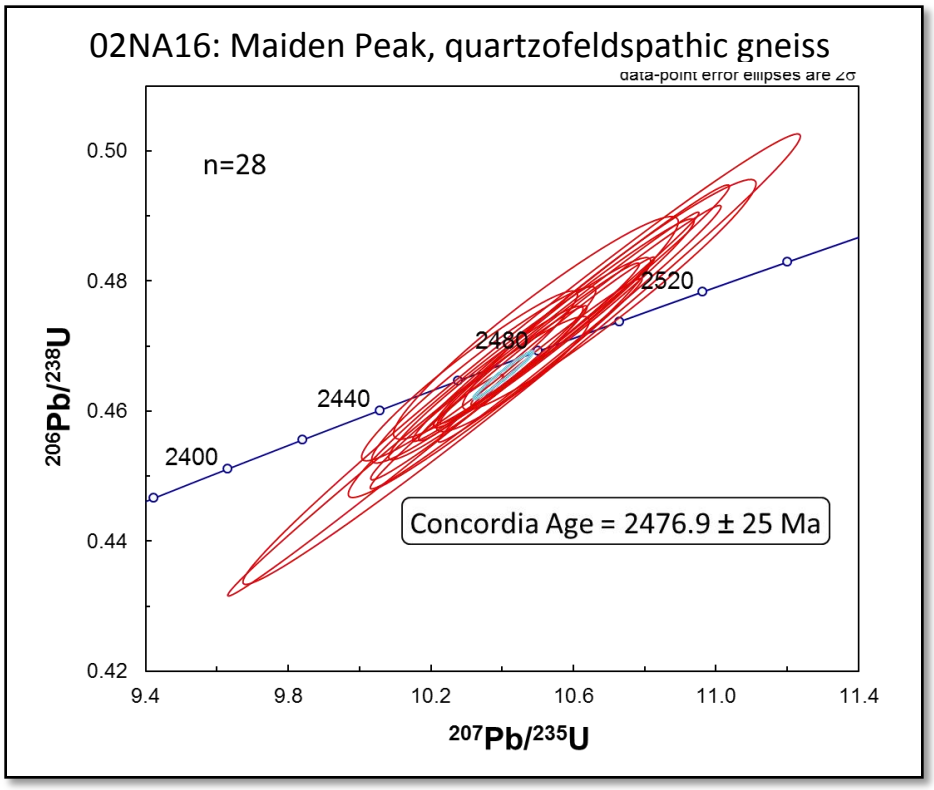

Figure 39: Concordia plot of sample 02NA16. U-Pb zircon analysis reveals a single zircon crystallization age of 2476.9 ± 25 Ma. Red ellipses represent the 2σ error for individual analyses. The blue ellipse is the average age and associated error of all analyses. The width of the A and B axes of this ellipse represent the degree of error. The location where this ellipse crosses the darker blue line is the Concordia age. Analyses with >10% discordance were excluded.

The Bloody Dick Gneiss

Xgb. Banded Gneiss of Bloody Dick Creek

Of the 100 spots selected for U-Pb analysis in this sample (25NA16), 8 were found to be discordant and were not used in age determinations or in the following plots. U-Pb zircon analysis reveals 2 primary age peaks with a few minor peaks in between them (Figure 40). As in sample 04NA16, these small peaks are interpreted to be mixed ages, an inadvertent consequence of the analysis spot overlapping the two distinct age

domains and incorporating isotopic ratios from each (see Figure 41 for a linearized probability plot that was used in this interpretation). BSE images reveal that these 2 zircon morphologies are ambiguous and highly irregular which made it difficult to properly distinguish between them during U-Pb analysis. In an additional similarity to sample 04NA16, zircon crystals appear subhedral to subrounded. The older of the 2 peaks is statistically left-skewed with the greatest number of zircons centered around ca. 2476 Ma. This left-skew may be evidence of multiple zircon forming events around this time, but no further evidence for such an interpretation has been recognized. This older peak and primary zircon population was taken from zircon cores that display oscillatory zoning in BSE images that were also used to identify the presence of distinct zircon growth rims around some of these cores. The smaller and younger U-Pb age peak was derived exclusively from analyses within zircon rims. Where zircon grain morphologies are less irregular, BSE images reveal that the rims lack oscillatory zoning and appear to be nearly homogeneous.

Note that the primary zircon growth event at ca. 2476 Ma is similar in age as samples 03NA16 (2483 ±23 Ma) and 02NA16 (2477 ± 25 Ma) from the Maiden Peak area. Hf analysis of 21 zircon grains reveals two isotopically distinct zircon populations, the older of which (ca. 2476 Ma peak) has a Hf model age of ca. 2900 statistically identical to the Hf model age of sample 03NA16. The younger zircon population (ca. 1761 Ma peak) has a spread of initial εHf values that range from -9 to +4.

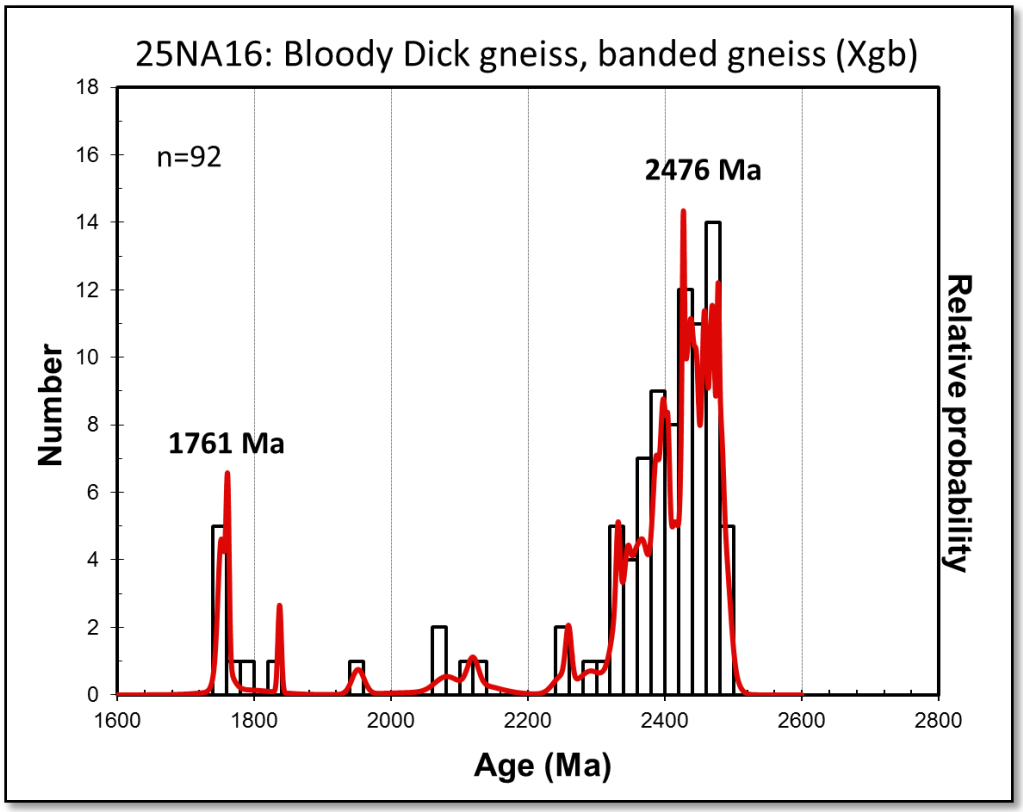

Figure 40: Sample 25NA16 contains two primary U-Pb age peaks at ca. 2476 Ma and ca. 1761 Ma. Smaller peaks between them and interpreted as being the result of spot analyses overlapping age domains within zircon grains. Zircon grain morphologies within this sample were irregular and difficult to interpret. A linearized probability plot aided in this interpretation (see Figure 29). The x-axis represents age (Ma) and the y-axis represents the number of grains. The red curve represents a probability density function associated with the age and error or each individual spot analyses. The height of the black boxes corresponds to the absolute number of zircon grains that fall within its age parameters. Analyses with >10% discordance were excluded.

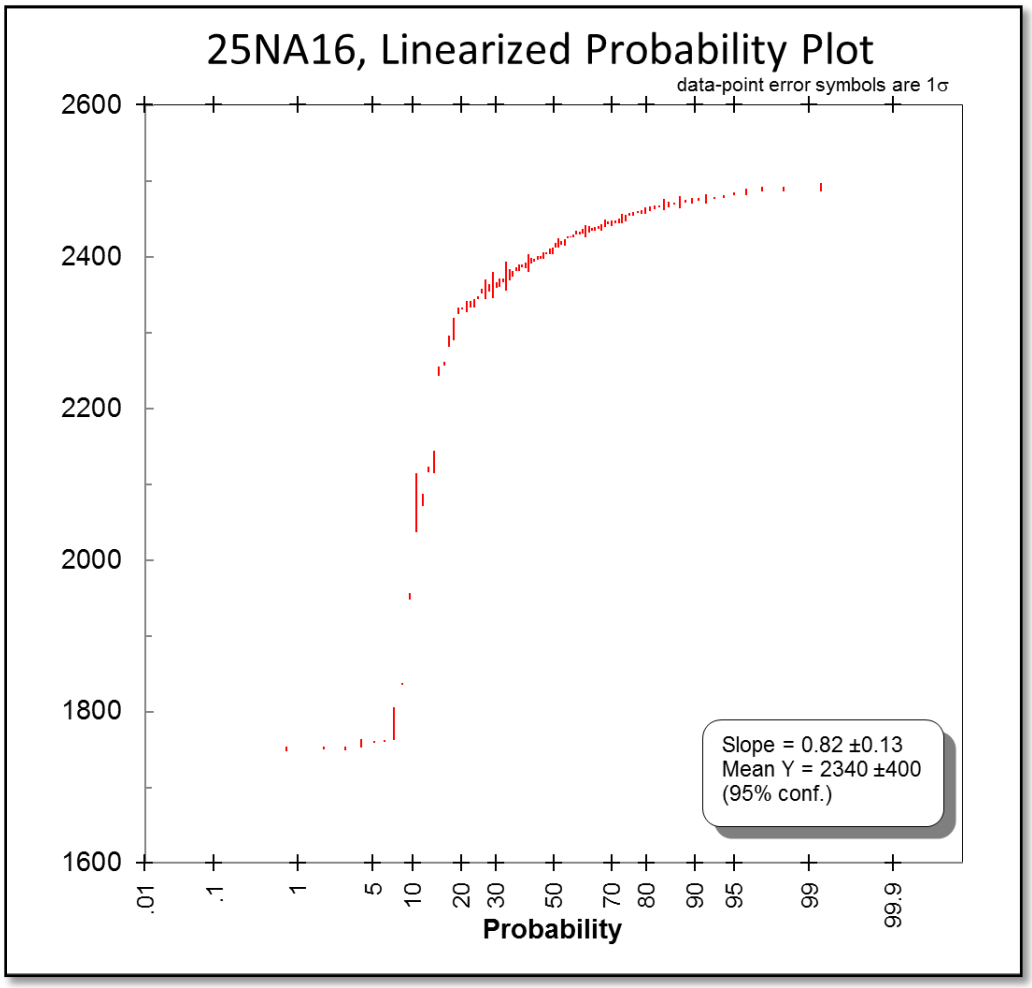

Figure 41: Linearized probability plot constructed from the age and error (Ma) from each analysis. This plot is helpful in differentiating unique zircon age populations from those of mixed domains. A mixed domain occurs when the analysis spot overlaps zircon domains of different ages, producing an apparent age that is a mixture of the two, distinct domains. Each red line represents the age and error (Ma) of an individual analysis. Red lines that plot sub-horizontally indicate zircons of the same age population. This linearized probability plot is interpreted as indicating the presence of two age domains located at the top and bottom of this plot.

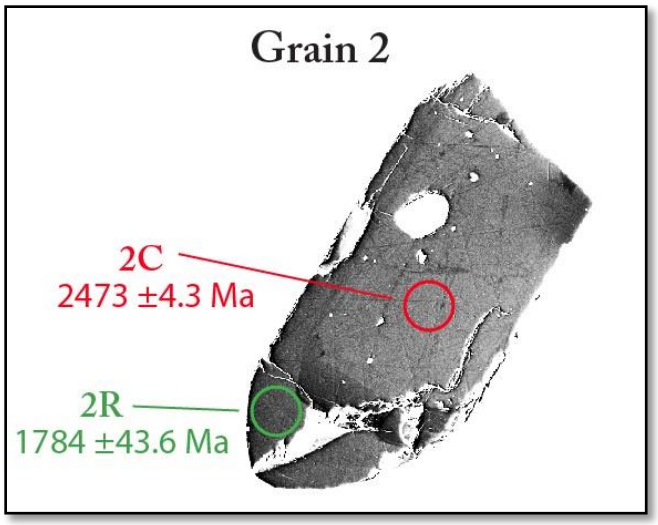

Figure 42: Backscattered electron (BSE) image of grain 2 from sample 25NA16 showing two distinct domains. The zircon core produced a U-Pb age of 2473 ± 4.3 Ma with a partial growth rim dated to 1784 ± 43.6 Ma.

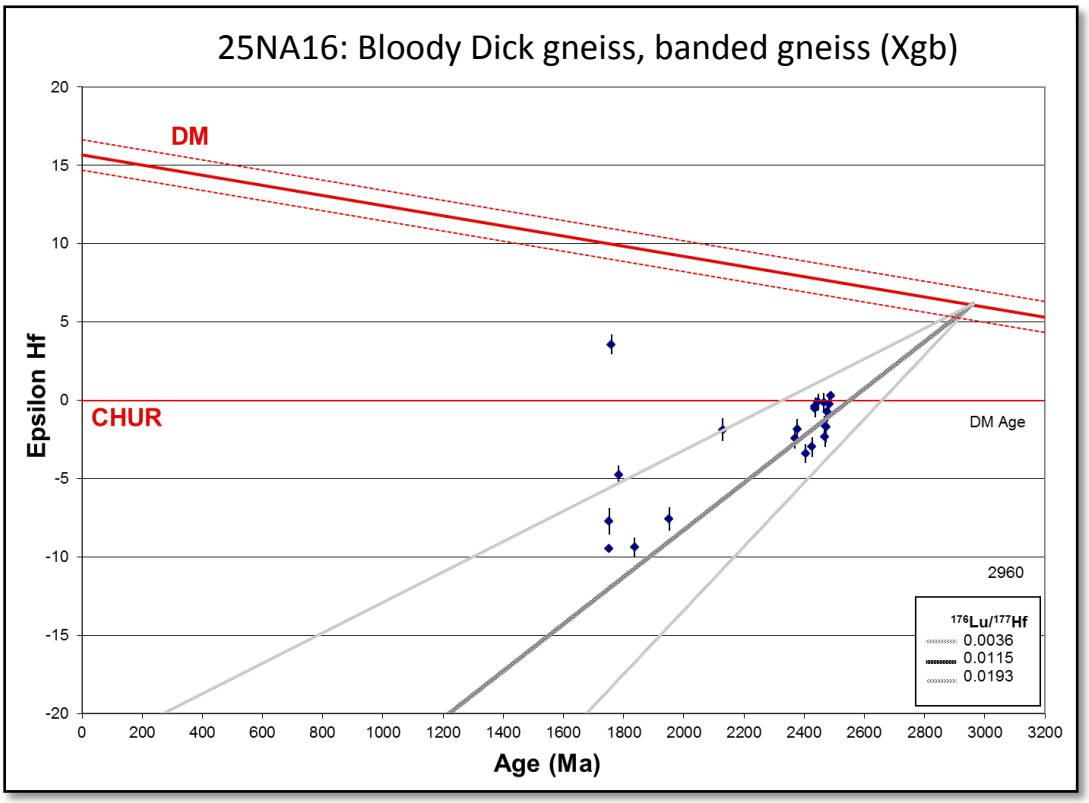

Figure 43: Hf analysis for sample 25NA16 shows 2 isotopically distinct populations. The younger model age with εHf values between +4 and -5.

Xgh. Hornblende Gneiss of Bloody Dick Creek

The U-Pb dating of 100 zircon grains from the hornblende gneiss of the Bloody Dick gneiss (8RL647) by Sherwin et al. (2016) (Figure 44) revealed a primary zircon age peak at 1878 Ma, with minor age peaks clustered around 2500 ± 80 Ma. The presence of multiple age peaks was originally interpreted as evidence of a paragneiss. However, the resultant age populations are very similar to those obtained with the current study; the latter are spatially associated with different growth domains in zircon rather than multiple detrital populations of grains. Thus, it is possible that the older analyses from sample 8RL647 could alternatively have sampled inherited zircon cores or xenocrysts, while the younger, dominant age peak may represent the crystallization age of an igneous protolith. Analysis of CL images taken of this sample (Richard Gaschnig, personal communication, March 2017) were limited by low image resolution. Though it is possible that the sampled rock is indeed a paragneiss, I believe that further work is needed to evaluate the alternative interpretation that the entirety of the Bloody Dick gneiss within the study area represents metamorphosed igneous rock (see the Discussion chapter below). A linearized probability plot (Figure 45) suggests the presence of a distinct zircon population ca. 2500 Ma, ca, 1850 Ma and a small population at ca. 1770 Ma. Zircons within the ca. 1770 population contain U/Th ratios greater than 10.

Hf analysis of zircons from sample 08RL647 (Richard Gaschnig, personal communication, March 2017) found a spread of initial εHf values that range from +1 to -7 between 1800 and 1900 Ma.

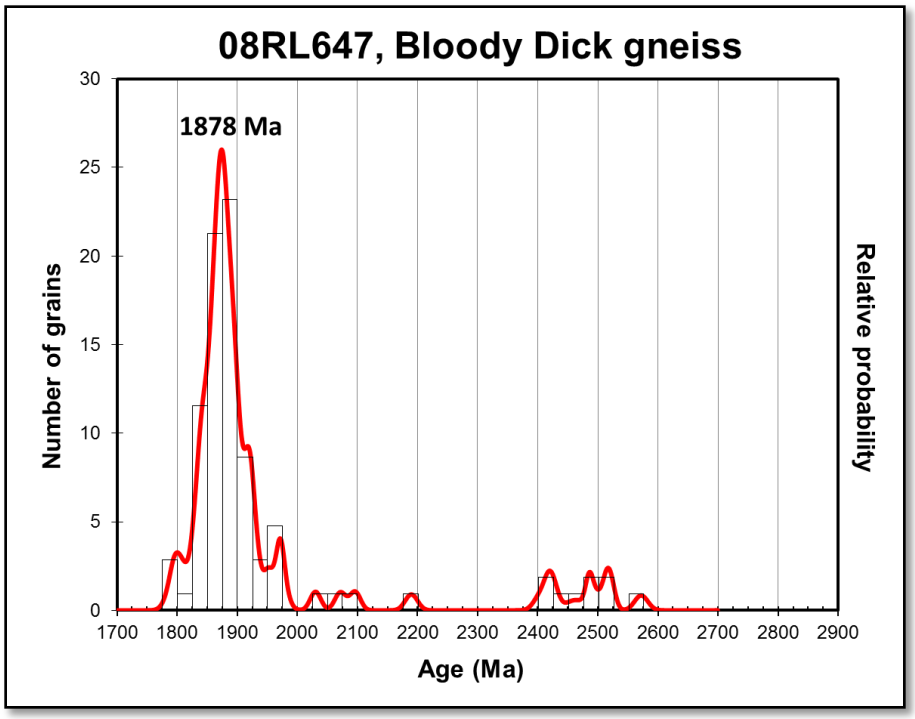

Figure 44: Probability density plot constructed from the U-Pb zircon analysis of sample 08RL647 taken from the hornblende gneiss of the Bloody Dick gneiss (Xgh). Zircon sample size of 100 grains. Sherwin et al. (2016).

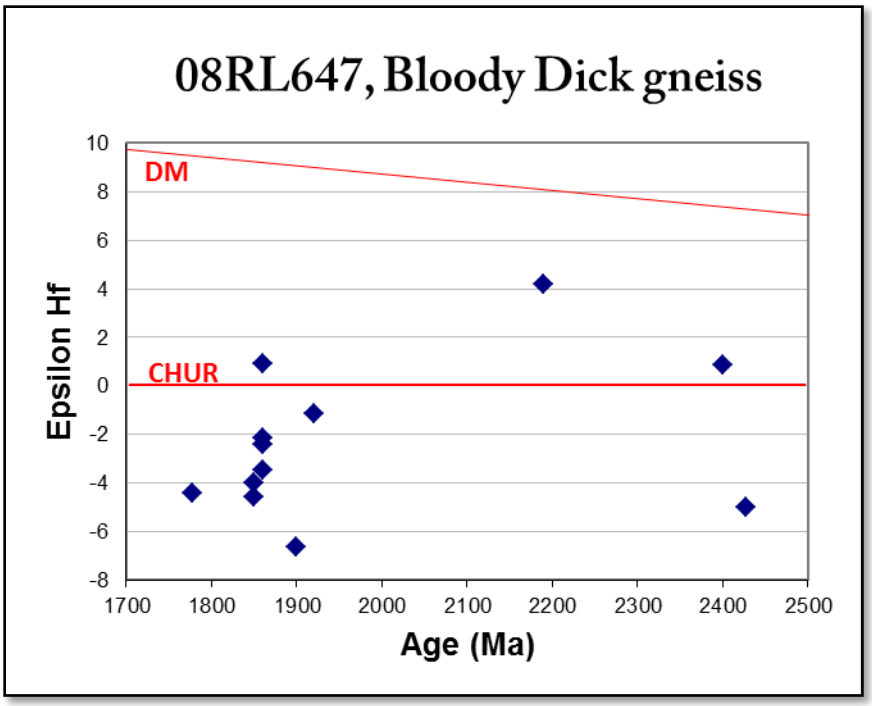

Figure 45: Hf analysis of zircons from sample 08RL647 shows a range of εHf values between +1 and -7 between 1800 and 1900 Ma (Richard Gaschnig, personal communication, March 2017).

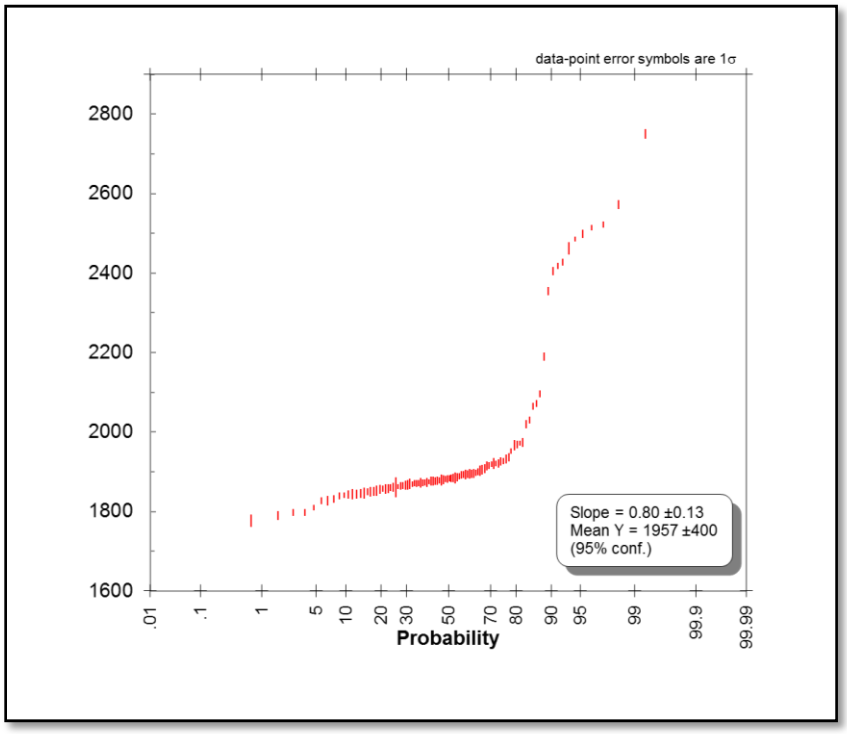

Figure 46: Linearized probability plot of sample 08RL647 suggesting an older zircon population ca. 2500 Ma, another ca. 1850 Ma and a small population at ca. 1770 Ma. Zircons of the ca. 1770 population contain U/Th ratios >10.

Additional U-Pb analyses of the Bloody Dick gneiss were obtained by Mueller et al. (2016), who dated 2 samples of the hornblende gneiss using SHRIMP-RG. These two samples, BDC-4 and BDC-5 yielded ages of 1890 ± 13 Ma (n=10) and 1790 ± 19 Ma (n=7), respectively (Table 4). Mueller et al. (2016) described the younger ca. 1790 Ma sample as a leucosome, suggesting that it may have been collected from a portion of the hornblende gneiss that was partially melted. Two of the seven analyzed zircon grains are 1859 and 1885 Ma, but the small sample size precludes calculating a statistically robust age.

Sample	Age(Ma)		Age (Ma)		Discordance
Spot	206Pb/238U	1s error	207Pb/206Pb	1 s error	%
BDC-4			**Age = 1.89+/-0.013 Ga**		n=10
BDC4-10.1R	1726	7	1777	10	3%
BDC4-4.1R	1729	6	1795	9	4%
BDC4-6.1R	1727	6	1802	12	4%
BDC4-3.1	1817	12	1805	15	-1%
BDC4-11.1R	1788	6	1819	25	2%
BDC4-9.1	1778	16	1844	13	4%
BDC4-6.2C	1909	8	1867	9	-2%
BDC4-4.2C	1915	10	1870	18	-2%
BDC4-12.1	1915	8	1883	9	-2%
BDC4-10.2C	1913	18	1892	21	-1%
BDC4-1.1	1832	11	1893	13	3%
BDC4-14.1	1801	11	1897	15	5%
BDC4-7.1	1780	8	1898	10	6%
BDC4-8.1	1858	7	1904	9	2%
BDC4-11.2C	1901	9	1908	11	0%
BDC4-15.1	1951	11	1974	12	1%
BDC4-5.1	1958	5	1976	6	1%
BDC4-2.1R	1946	5	1980	5	2%
BDC4-13.1	2005	11	2016	155	1%
BDC-5		**Age = 1.79+/-0.019 Ga (Th/U< 0.1)**			n=7
BDC5-5.1	1628	6	1728	9	6%
BDC5-9.1	1733	8	1782	16	3%
BDC5-2.1	1769	6	1786	7	1%
BDC5-7.1R	1812	6	1790	8	-1%
BDC5-6.2T	1808	7	1792	9	-1%
BDC5-8.1	1766	6	1797	6	2%
BDC5-10.1	1763	5	1797	6	2%
BDC5-3.1	1803	5	1800	5	0%
BDC5-4.1	1746	6	1803	7	3%
BDC5-1	1857	11	1859	15	0%
BDC5-6.1	1818	11	1885	12	4%

Table 4:. U-Pb zircon data of sample BDC-4 and BDC-5 by Mueller et al. (2016).

Xga. Augen gneiss of Bloody Dick Creek.

This unit was previously sampled for U-Pb zircon analysis by Mueller et al. (2016; samples BDC-2 and BDC-6; Table 2; Figure 47 and Figure 5). Results show a bimodal distribution of zircon ages, similar to the hornblende gneiss. Sample BDC-2 returned a U-Pb age of 1910 ± 20 Ma (n=8) with 1 zircon grain dated to 2580 Ma. BDC6 returned a U-Pb age date of 1800 ± 60 Ma (n=12) with a single zircon dated to 2351 Ma.

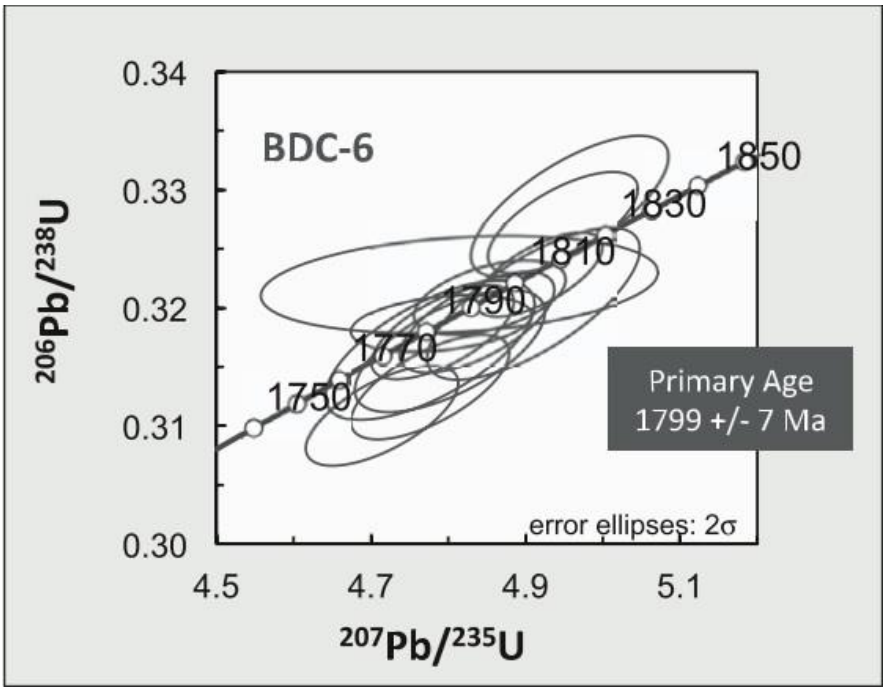

Figure 47: Concordia plot constructed from the U-Pb zircon analysis of sample BDC-6 taken from the augen gneiss unit (Xga) of the Bloody Dick gneiss. Zircon sample size of 12 grains. Mueller et al. (2016).

Sample	Age(Ma)		Age (Ma)		Discordance
Spot	206Pb/238U	1s error	207Pb/206Pb	1 s error	%
BDC-2			**Age = 1.91 +/- 0.02 Ga**		n=8
BDC2-9.1R	1781	6	1783	7	0%
BDC2-1.1R	1816	4	1793	4	-1%
BDC2-7.1	1864	4	1793	5	-4%
BDC2-1.2C	1860	10	1844	21	-1%
BDC2-6.1	1832	6	1865	7	2%
BDC2-3.1	1897	5	1879	6	-1%
BDC2-12.1	1808	14	1896	19	5%
BDC2-8.1	1870	13	1898	16	1%
BDC2-6.2C	1855	48	1902	14	2%
BDC2-2.1	1899	14	1906	16	0%
BDC2-7.2C	1834	18	1909	19	4%
BDC2-10.1	1918	16	1909	19	0%
BDC2-5.1	1916	20	1919	24	0%
BDC2-4.1	2023	10	1970	10	-3%
BDC2-11.1	2359	21	2580	34	9%
BDC-6			**Age = 1.80+/-0.06 Ga**		n=12
BDC6-7.2R	1931	7	1771	56	-9%
BDC6-6.1	1799	8	1773	39	-1%
BDC6-3.1R	1783	5	1783	18	0%
BDC6-5.1	1780	8	1788	11	0%
BDC6-4.1	1832	12	1790	14	-2%
BDC6-14.1	1772	12	1791	16	1%
BDC6-8.1	1825	8	1794	11	-2%
BDC6-12.1R	1794	6	1794	13	0%
BDC6-13.1	1745	9	1799	12	3%
BDC6-1.1	1784	9	1800	12	1%
BDC6-8.1	1772	10	1801	15	2%
BDC6-2.1	1804	7	1807	9	0%
BDC6-10.1	1757	9	1809	12	3%
BDC6-11.1	1791	13	1819	14	1%
BDC6-7.1	2324	11	2351	12	1%

Table 5:. U-Pb zircon data of sample BDC-2 and BDC-6 by Mueller et al. (2016).

Xgf. Felsic gneiss of Bloody Dick Creek.

Of the 41 U-Pb analyses, 3 were greater than 10% discordant and were excluded from the data. Results produced a U-Pb zircon age of 1802 ± 17 Ma. BSE images of the felsic gneiss, sample 18NA16, show euhedral zircon crystals and a lack of any zircon core and ring morphologies.

One anomalous zircon grain (18NA16-15) was found to have a core that was dated to 2258 ± 25 Ma, a date not identified in any sample in this study. Unfortunately, this analysis was 14.8% discordant, so confidence in this result is low. However, this particular zircon grain is most interesting because it was also found to have a rim that was dated to 1618 ± 9.5 Ma, another date not identified in this study, and is only 1.5% discordant. With a discordant core and only one U-Pb analysis with this anomalous date, it is difficult to make any inferences with about this result with any level of confidence.

Hf analysis of 14 zircon grains found a spread of εHf units between +3 and -3, but it is important to note that this variation is bound within the upper and lower statistical limits for this Hf model age.

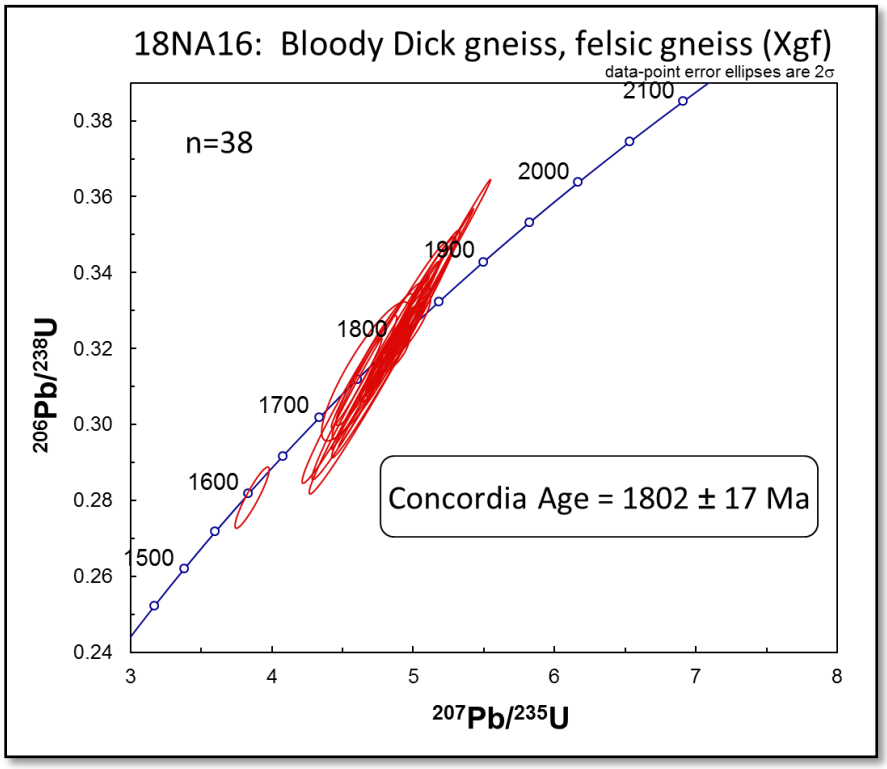

Figure 48: Concordia plot of sample 18NA16. U-Pb zircon analysis reveals a single zircon crystallization age of 1802 ± 17 Ma. Red ellipses represent the 2σ error for individual analyses. The blue ellipse is the average age and associated error of all analyses. The width of the A and B axes of this ellipse represent the degree of error. The location where this ellipse crosses the darker blue line is the Concordia age. Analyses with >10% discordance were excluded.

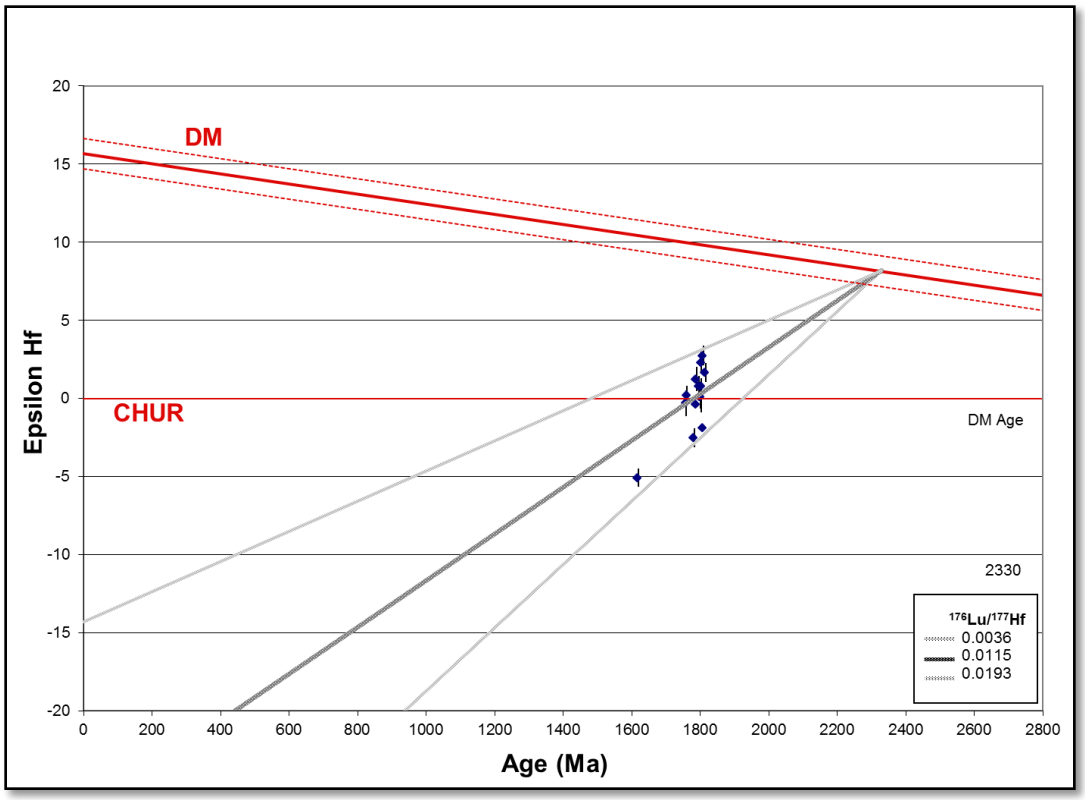

Figure 49: Hf analysis for sample 18NA16 shows 1 isotopic population with an εHf value between +3 and -3, ca. 1760 Ma. One analysis returned an εHf value of -5 at 1619 Ma.

(U-Th)/He Results

Four individual grains were successfully dated from the felsic gneiss (18NA16) using the (U-Th)/He zircon method. The data produced a weighted mean age and 2-sigma error of 72.4 ± 1.5 Ma.

Chapter V: Discussion

Structural Interpretations

Normal faults

The eastern strand of the Beaverhead Divide Fault (ESBDF) (Lonn et al., 2016) forms the western boundary of the Bloody Dick gneiss, but field relations suggest that

this section of the fault may be inactive: South of Bloody Dick Creek, the ESBDF is cut by a small east-west striking normal fault; additionally, unbrecciated diabase is found all along the ESBDF south of Bloody Dick Creek and in discontinuous sections north of the creek. Although $^{40}Ar/^{39}Ar$ dating of this diabase by VanDenburg et al. (1998) was unsuccessful, similar intrusions in the region were dated to 46 ± 2 Ma by Lonn and Lewis (2009). South of Bloody Dick Creek, $^{40}Ar/^{39}Ar$ dating constrained the age of a basalt flow to 47.51 ± 0.42 Ma (VanDenburg et al., 1998), which overlies both the fault diabase and the Bloody Dick gneiss. Not only do all of these observations suggest that the ESBDF is inactive south of Bloody Dick Creek, it constrains the minimum age of activity on the fault to the early-middle Eocene. Near the southern extent of the Bloody Dick gneiss, the ESBDF is covered by rhyolitic rocks of the Challis Volcanic Group and is no longer exposed at the surface south of this location.

Northwest of the Bloody Dick gneiss, the ESBDF was interpreted by Lonn et al. (2016) as a Cretaceous thrust that was reactivated to accommodate Tertiary extension.

Approaching the Bloody Dick gneiss from the northwest, the ESBDF contacts the gneiss in Big Hollow. At this location, the ESBDF divides into its two faults: the Monument thrust on the east and the ESBDF on the west that extends south of Bloody Dick Creek.

A previously unmapped normal fault was identified near the mouth of Sullivan Gulch based on the presence of extensive fault gouge and slickenlines exposed in a road cut. This northwest striking fault is hereto in referred to as the Sullivan fault. There is a lack of significant offset across topography or nearby contacts, but a sufficient number of slickenlines were measured within the fault gouge to identify a northeastward sense of

slip in the hanging wall and a fault plane dipping approximately 57° in the same direction. See Plate 1 for the geologic map, which includes a stereonet of the slickenlines associated with the Sullivan fault.

Foliation and Thrusting

South of Bloody Dick Creek, the foliation generally strikes towards the northwest, dipping down to the northeast at an average of 55°. The general continuity of northwest and southeast-striking foliations throughout the Bloody Dick gneiss and the high-temperature deformational fabrics such as gneissic banding, ductile folding and feldspar augen are interpreted as evidence that the foliation formed during the Big Sky orogeny and therefore long predates the Monument fault. The interpretation of foliation attitudes north of Bloody Dick Creek reveal a syncline and anticline pair with a northwest-trending fold axis. Due to its structural position adjacent to and in the immediate hanging wall of the northwest-striking Monument fault and its northeast vergence, the anticline is interpreted as a fault propagation fold (see Jamison (1987) for the definition) associated with the formation of the Monument fault. Sample 14NA16A was collected from an old exploratory pit that was dug directly on the Monument fault and ductile fabrics are observed in an oriented thin section, which have been interpreted as kinematic indicators preserving a “top to the northeast” sense of shear (Figure 50). This thin section was cut perpendicular to sub-vertical stretching lineations that were observed in the hand sample and other rocks from the exploratory pit. Spatial orientation of this shear direction is interpreted as evidence that the Bloody Dick gneiss is in the hanging wall of the steeply

southwest dipping Monument thrust, which juxtaposed the gneiss next to Belt quartzite of the Swauger Formation.

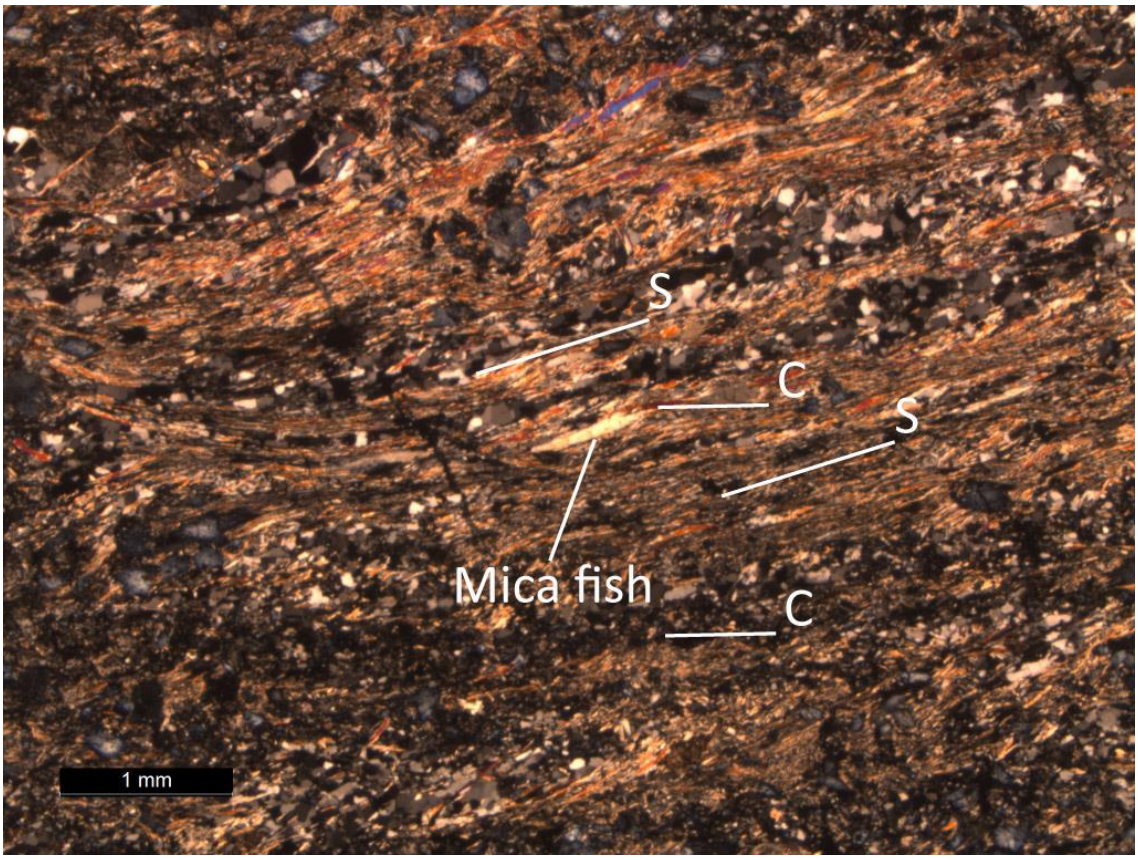

Figure 50: Thin section of sample 14NA16A taken from the Monument fault zone that shows a "top to the right" sense of shear interpreted from the mica fish and S-C fabric. The plane of this oriented thin section is sub-vertical, parallel to sub-vertical stretching lineations, looking towards the southwest (244°), placing the Bloody Dick gneiss to the left and the Swauger Formation to the right.

Cross Section

The geologic map of the Bloody Dick gneiss (Plate 1) indicates that eastern and southern margin of the gneiss are unconformably overlain by Tertiary volcanic and sedimentary rocks while the western and northern margins are fault bounded and juxtaposed next to Mesoproterozoic Belt Supergroup quartzite units. Along with thin

section analysis, the structural interpretation of the geologic map identifies the Monument thrust as the mechanism by which the Bloody Dick gneiss was exhumed, and the ESBDF as a shortcut fault which roots down into the thrust décollement and accommodated crustal extension (Figure 51).

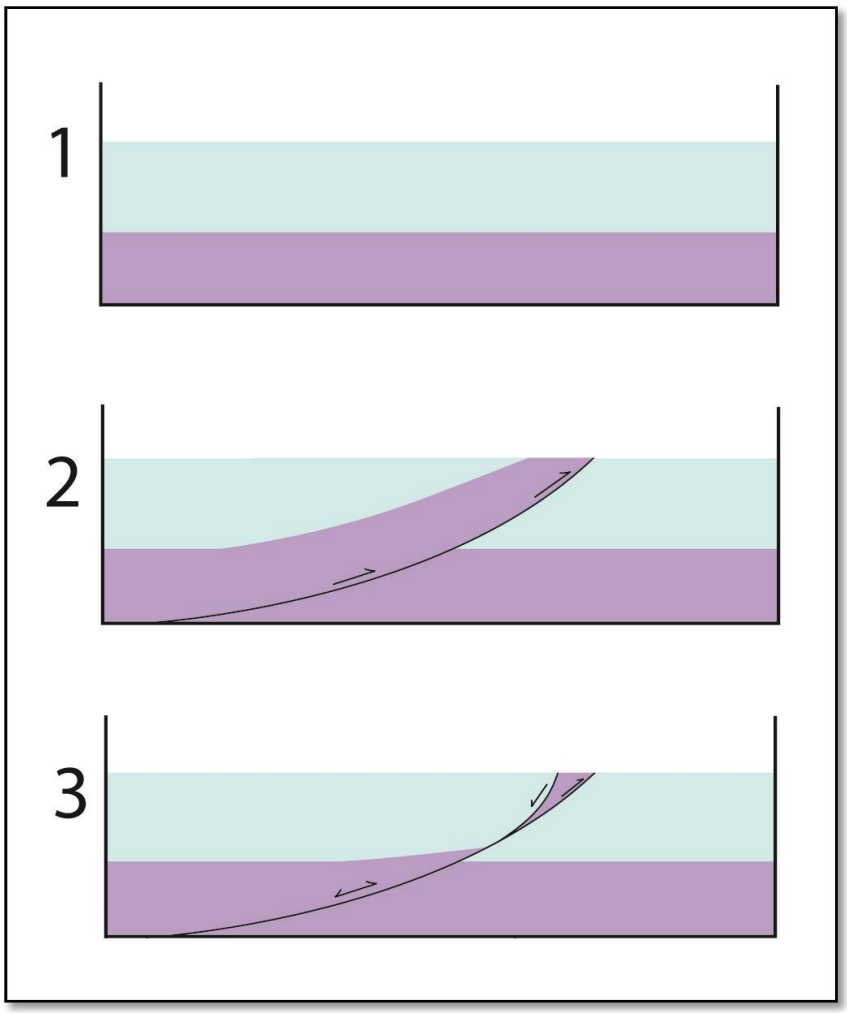

Figure 51: Schematic illustration depicting the formation of a shortcut fault which roots down into the original thrust décollement, abandoning a wedge of stratigraphically deep material at the surface.

Protolith of the Bloody Dick gneiss

Despite the variations in lithology between the 4 units of the Bloody Dick gneiss, thin section analyses suggest that these rocks can be categorized into 2 primary lithologies.

1. Quartzofeldspathic gneiss containing abundant, coarse-grained microcline and plagioclase feldspar, quartz, hornblende and biotite with minor components of chlorite and garnet.
2. Hornblende gneiss with >75% hornblende and plagioclase feldspar veins that often contain 3-6 mm wide augen.

The absence of abundant pelitic minerals and the lack of rounded zircon grains in BSE images from across the Bloody Dick gneiss casts doubt on a potential sedimentary protolith. Additionally, the interpretation of an igneous protolith comes from the following observations:

1. A composition of quartzofeldspathic and hornblende gneiss.
2. The presence of subhedral to euhedral zircon crystals in BSE images
3. Large, typically 5-10 mm plagioclase feldspar grains and augen.
4. Inclusions and intrusive, cross-cutting relationships observed between the hornblende gneiss, augen gneiss and felsic gneiss units.
5. Unimodal zircon populations.
6. Core-rim relationships of ages.
7. U/Th ratios of rims vs. cores, which are consistent with metamorphic and igneous analyses.

The interpretation by Mueller et al. (2016) of small, isolated exposures of schist within the augen gneiss being of a metavolcanic or metavolcaniclastic protolith implies an extrusive environment, but the authors note that their observation of restricted U-Pb zircon ages derived from the Bloody Dick gneiss argue against a sedimentary protolith. Additionally, the extensive, intrusive contact between the hornblende gneiss, augen gneiss and felsic gneiss documented in this study is more simply interpreted as being of a plutonic origin.

Isotopic Interpretations

Maiden Peak, quartzofeldspathic gneiss

U-Pb analysis of zircons from the Maiden Peak area is interpreted as evidence of plutonism at ca. 2789 Ma (Population 1, sample 04NA16; Figure 33), an event associated with the Beartooth orogeny (Wooden and Mueller, 1988) along the western margin of the Wyoming craton. Within this sample is a smaller U-Pb zircon peak at ca. 2497 Ma that was obtained from metamorphic growth rims around ca. 2789 Ma zircon cores. This younger age of ca. 2497 Ma is also found in the U-Pb analysis of two other samples of gneiss from the Maiden Peak area, 03NA16 and 02NA16 (Population 2), which each contain a single zircon crystallization age at 2483 ± 23 Ma (Figure 37) and 2477 ± 25 Ma (Figure 39), respectively. These dates closely resemble the U-Pb age of 2455 ±9 Ma that was derived from the quartzofeldspathic gneiss in Law Creek Canyon in the Tendoy Range, 22 km to the southeast (Kellogg et al., 2003). Across the western margin of the Wyoming craton, U-Pb dates between 2450 and 2480 Ma are closely associated in time

with the Farmington zone, which contains an identical spread of zircon dates (Mueller et al., 2011). However, metamorphism and plutonism of the same age in southwest Montana (Cramer, 2015) is attributed to the Tendoy orogeny (Baldwin et al., 2014). The relationship of this to the Farmington zone is not known at this time.

The U-Pb and Hf isotopic results of Maiden Peak Population 2 (03NA16 and 02NA16) are identical to sample 25NA16 collected from the banded gneiss unit of the Bloody Dick gneiss. This isolated and previously unrecognized unit of the Bloody Dick gneiss contains a primary U-Pb age peak at ca. 2476 Ma and a smaller age peak at ca. 1761 Ma (Figure 40). Combined with a quartzofeldspathic mineral assemblage, this U-Pb and Hf isotope affinity is interpreted as evidence that the banded gneiss is isotopically similar, if not identical, to the quartzofeldspathic gneiss of the Maiden Peak area, establishing the first recognized link between the two bodies.

The Bloody Dick gneiss

In addition to a ca. 2476 Ma age peak, the banded gneiss (25NA16) contains a small ca. 1761 Ma peak that was obtained from what are interpreted as metamorphic zircon growth rims based on high U/Th ratios of up to 21.3 (Wan et al., 2011) within the rims (grain 78). In southwest Montana, high-grade metamorphism between 1780 to 1720 Ma is associated with the Big Sky orogeny (Harms et al., 2004; Cheney et al., 2004; Condit et al., 2015; Mueller et al. 2016), an interpretation shared in this study for the ca. 1761 Ma metamorphic zircon growth peak observed in the banded gneiss.

North of Bloody Dick Creek, no outcrops of the banded gneiss are observed. Instead, the lithology is dominated by a hornblende gneiss dated to ca. 1878 Ma with an

εHf value between +1 and -5 (Richard Gaschnig, personal communication, March 2017) and U-Pb zircon ages of 1890 ± 13 Ma and 1910 ± 20 Ma by Mueller et al. (2016). A linearized probability plot (Figure 46) of sample 08RL647 (Sherwin et al., 2016) suggests the presence of distinct zircon populations at ca. 2500 Ma, ca. 1850 Ma and ca. 1800 Ma. Within the ca. 1800 zircon population, high U/Th ratios suggest that they are metamorphic and may be associated with the intrusion of the felsic gneiss (18NA16) at 1802 Ma ± 17 Ma. This data implies that the older, banded gneiss was either intruded, juxtaposed, or nonconformably overlain by isotopically juvenile, mafic material ca. 1878-1900 Ma. Unfortunately, no contact between these two units could be located.

The mafic, hornblende gneiss was intruded at 1802 ± 17 Ma by felsic, isotopically juvenile material with initial εHf values between +3 and -3. The intrusive contact between the felsic and hornblende gneiss is so gradational and extensive that it has been distinguished in this study as its own unit, called the augen gneiss, which varies from a lightly intruded, hornblende dominated lithology, to a coarse grained, augen rich, felsic lithology with increasing proximity to the felsic gneiss unit. Inclusion of the hornblende gneiss are observed within the augen gneiss in several locations (Figure 26). U-Pb zircon ages from the augen gneiss (Mueller et al. 2016) produce bimodal crystallization dates at either ca. 1900 Ma or ca. 1800 Ma, closely aligning with either the mafic or felsic igneous age, respectively. This bimodal result is interpreted as being dependent on the sample collection location, either incorporating more material from the hornblende gneiss or from the felsic gneiss and its extensive intrusions. However, a relatively small sample sizes of n=7 to n=10 make more detailed interpretations of these U-Pb results ambiguous.

I interpret the robust (U-Th)/He zircon age from felsic gneiss (18NA16) in the hanging wall of the Monument fault to indicate ongoing thrust-induced exhumation during the Late Cretaceous at 72.4 ± 1.5 Ma. A Late Cretaceous age of thrusting during the Sevier orogeny is consistent with previous interpretations by Skipp (1988) and Lonn et al. (2016) who worked in the along-strike equivalents of the Monument thrust along the Beaverhead Divide-Cabin thrust system.

Regional Implications

Current models of the Greats Falls orogeny constrain the timing of subduction-related arc magmatism to between ca. 1860 Ma and 1790 Ma (Harms et al., 2004; Mueller et al., 2016) and the initiation of continental collision to 1790-1780 Ma (Big Sky orogeny) (Cheney et al., 2004; Foster et al., 2006; Condit et al., 2015; Mueller et al., 2016). Given the hypothesized NW dip to the subduction zone (Gorman et al., 2002; Harms et al., 2004), associated arc magmatism is thought to have been confined to the southeastern margin of the overriding Medicine Hat block (Foster et al., 2006).

Within the Bloody Dick gneiss in the current study area, the hornblende gneiss was previously dated to ca. 1900-1878 Ma (BDC4 and BDC5, Mueller et al., 2016; 08RL647, Sherwin et al., 2016) and current results constrain intrusion of the felsic gneiss to 1802 ± 17 Ma (18NA16). Though whole rock Sm-Nd data (Mueller et al., 2016) and zircon Lu-Hf data (08RL647, hornblende gneiss zircon Hf data provided by Richard Gaschnig, personal communication, March 2017; this study) indicate some remobilization of older continental lithosphere, the felsic gneiss requires input of an isotopically juvenile component at ca. 1802 Ma (Figure 52). Similar results from the

Little Belt Mountains of the Great Falls tectonic zone also indicate that ca. 1860 Ma plutons were derived from an isotopically juvenile source. Thus, the similarity of the current results to gneisses from the Little Belt Mountains of the Great Falls tectonic zone suggests that the Great Falls tectonic zone projects into southwest Montana at least as far as the Bloody Dick gneiss, 8 km east of the Idaho state line. A minor component of xenocrysts as old as ca. 2600 Ma within the hornblende gneiss (Mueller et al., 2016) and the felsic gneiss likely indicates that these units intruded through older crust, but a volcaniclastic protolith for the small bodies of schist (Mueller et al., 2016; Sherwin et al., 2016) within the hornblende gneiss cannot be ruled out.

These observations may be reconciled with a model introduced by Harms et al. (2004) in which they propose that the Little Belt arc formed within a rifted fragment of the Wyoming craton.

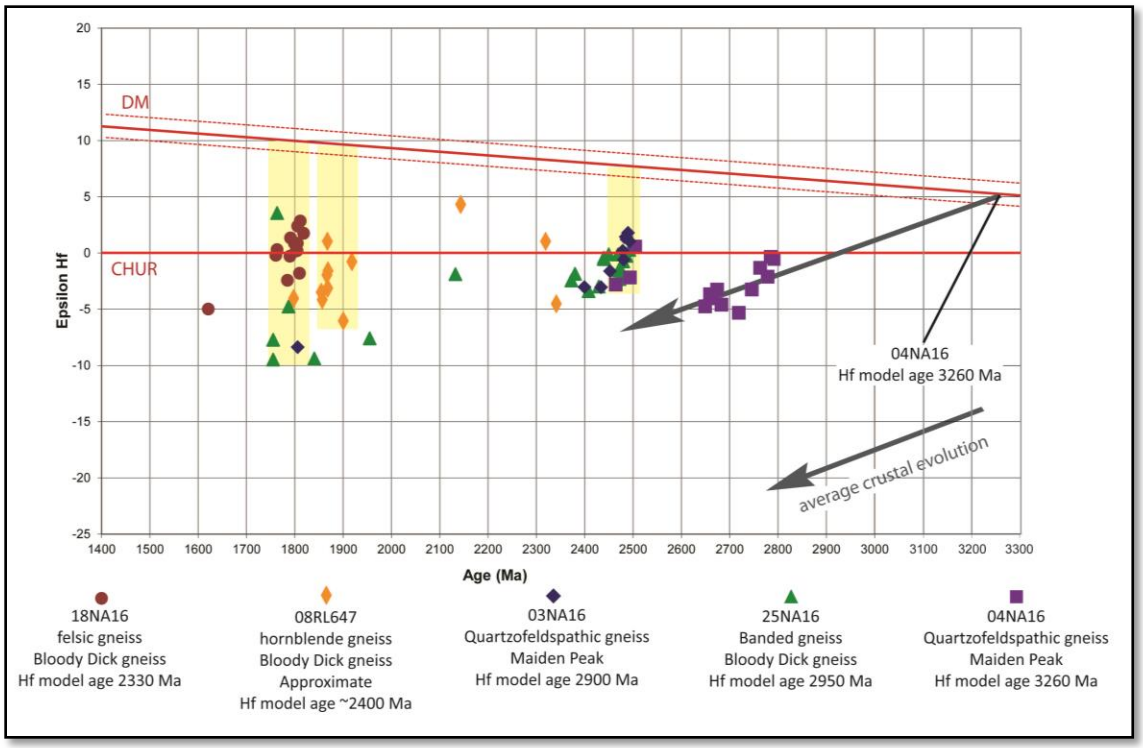

Figure 52: εHf values. Distinct shapes and colors correspond to individual samples. Yellow boxes indicate interpreted mixing of materials with different Hf isotope compositions. Note the average crustal evolution arrows placed over sample 04NA16 (purple squares). Later melts of this material would produce εHf values that plot along the projection of this arrow. Thus, results indicate input of isotopically juvenile material at 1800-1900 Ma, and possibly at ca. 2497 Ma. Sample 08RL647 Hf data provided by Richard Gaschnig, personal communication, March 2017.

Archean and Proterozoic Terranes

The Maiden Peak and Bloody Dick gneiss units contain U-Pb zircon ages and initial Hf isotopic values which suggest that the several samples are part of the Archean Wyoming craton (affected by the 2780 Ma Beartooth orogeny), Farmington zone (affected by the 2550 to 2455 Ma Tendoy orogeny), and the Great Falls tectonic zone (affected by 1790 to 1720 Ma Big Sky orogeny).

Based on its 2789 Ma U-Pb age, sample 04NA16 is temporally correlated with the Beartooth orogeny, an event that affected the Wyoming craton (Skinner et al., 1969; Reid et al., 1975; Wooden and Mueller, 1998).

Within the banded gneiss (25NA16) a U-Pb age peak of ca. 2476 Ma is identical to the U-Pb dates from two samples collected from the quartzofeldspathic gneiss at Maiden Peak, 2483 ± 23 Ma (03NA16) and 2477 ± 25 Ma (02NA16). These units also share statistically identical εHf values of +2 to -4 (Figure 52). This 2476 Ma U-Pb age is closely associated with rocks from the Farmington zone (Mueller et al., 2011), and is contemporaneous with the Tendoy orogeny (Cramer, 2014).

Prior work within the hornblende gneiss lithologic unit of the Bloody Dick gneiss yielded zircons with U-Pb ages of ca. 1900 – 1878 Ma (Mueller et al., 2016; Sherwin et al., 2016); new data indicate that the felsic gneiss (18NA16) is 1802 ± 17 Ma. Each of these two units share U-Pb ages and isotopically juvenile characteristics with the Little Belt Mountains within the Great Falls tectonic zone (Mueller et al., 2002).

Several zircon cores from the ca. 2476 Ma banded gneiss (25NA16) contain metamorphic zircon rims dated to ca. 1761 Ma. These are interpreted to have grown during the Big Sky orogeny (Harms et al., 2004).

The Lemhi Arch, and The Great Divide Megashear

The Lemhi Arch is an east-west oriented uplift within the Lost River, Lemhi and Beaverhead ranges where the Ordovician Summerhouse Formation unconformably overlies Mesoproterozoic or Neoproterozoic to Cambrian strata (Link and Janecke, 1999). The precise location of the of the Lemhi Arch is poorly constrained in southwest Montana, but the region surrounding and west of the Bloody Dick gneiss is interpreted as being within the arch due to the lack of Neoproterozoic to Cambrian strata.

Along the eastern side of the Horse Prairie, among the western foothills of Maiden Peak is a narrow, 200 m thick exposure of the Ordovician Summerhouse Formation (M'Gonigle and Hait, 1997). Although the base of the Summerhouse Formation is not exposed in this location, these workers interpret it to be nonconformably overlying the quartzofeldspathic gneiss. Ruppel (1986) interprets the Summerhouse Formation to have onlapped against the eastern margin of the Lemhi Arch during the Ordovician. This interpretation, with the presence of Summerhouse Formation carbonates west of Maiden Peak, tightly constrains the eastern margin of the Lemhi Arch to this location, a mere 8 km southeast of the Bloody Dick gneiss.

The Great Divide megashear is a theoretical ~500 km long Proterozoic structure described by O'Neill et al. (2007) as accommodating left-lateral strike-slip Mesoproterozoic deformation. The presence of such a structure was interpreted as a possible explanation for the Belt basin and Lemhi sub-basin that were believed to have distinct origins based on differences in their stratigraphy, but were juxtaposed by this megashear. The authors state: "The Bloody Dick segment of the megashear, previously interpreted to be a thrust fault zone (Coppinger, 1974; Ruppel et al., 1993) is a vertical zone of mylonitic rock more than 1.5 km wide. Stretching lineations in the mylonite are subhorizontal, plunging gently both northwest and southeast."

While some vertical foliations and subhorizontal shear do exist within the Bloody Dick gneiss, they are not interpreted in this study as evidence for a regional-scale mylonitic shear zone. Vertical or subvertical foliations are uncommon and only exist along the northern margin of the Bloody Dick gneiss within the limbs of the fault

propagation fold that is associated with the formation of the Monument fault, containing its own vertical stretching lineations (see Structural Results above). Outside of this fold, foliations generally strike to the northwest with an average dip of only 45-55°. I interpret these as having formed along with the augen under high-grade metamorphic conditions during the Big Sky orogeny. I could not find evidence to support the Great Divide Megashear within the Bloody Dick gneiss.

Thrusting and Extension

The interpretation that the banded gneiss unit within the Bloody Dick gneiss is the same material as the quartzofeldspathic gneiss near Maiden Peak requires a mechanism to explain their current spatial separation of only 20 km. I agree that the Bloody Dick gneiss and the quartzofeldspathic gneiss near Maiden Peak are part of the same thrust sheet (Cabin-eastern strand of Beaverhead Divide fault). This agrees with Skipp (1988) and Lonn et al. (2016) who state that the Cabin thrust may be the southeastern continuation of the Beaverhead Divide fault system. Additionally, Skipp (1988) defines the Cabin thrust by its involvement of crystalline basement rocks, primarily, the quartzofeldspathic gneiss in the Tendoy Range. See Figure 53 for a regional map illustrating locations of the Beaverhead Divide fault system and the Cabin thrust. Along the eastern flank of the Tendoy Range, the location of the northern extension of the Cabin thrust becomes ambiguous near the southeastern end of Maiden Peak, but its continuation to the north is required by the continuation of the deeply exhumed quartzofeldspathic gneiss as far north as 44° 57’ 30” (M’Gonigle and Hait, 1997). Restoration of the primarily east-west extension with ~25% north-south extension across the Horse Prairie by VanDenburg et

al. (1998) brings the Bloody Dick gneiss closer to the quartzofeldspathic gneiss in Maiden Peak.

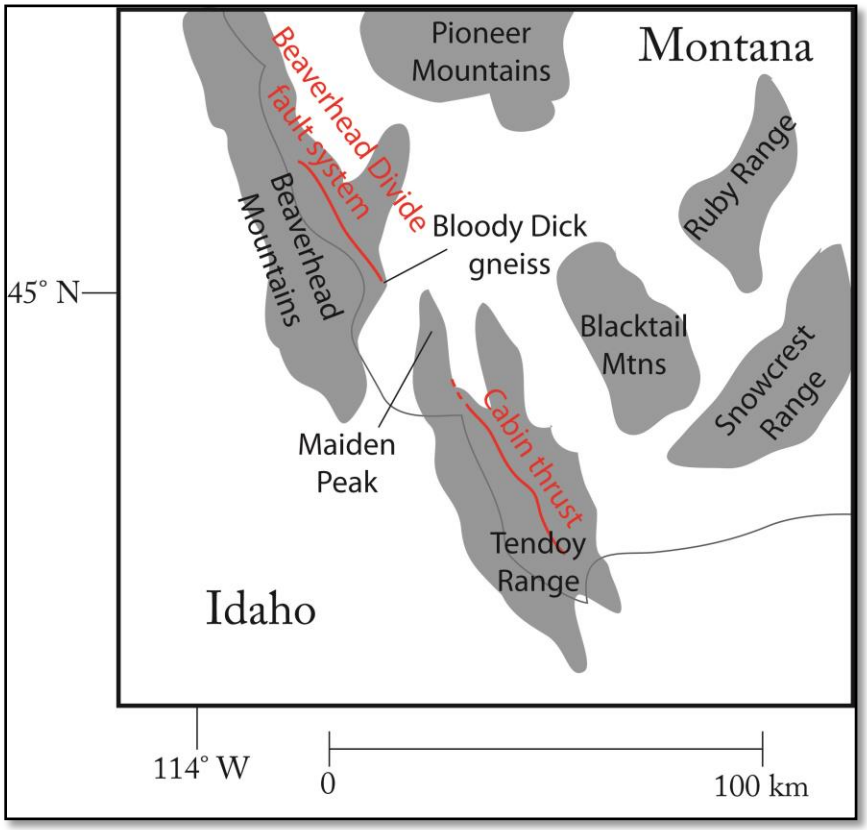

Figure 53: Locations of the Beaverhead Divide fault system and the Cabin thrust relative to the Bloody Dick gneiss and Maiden Peak.

Chapter VI: Conclusions

Within the Tendoy Range of southwest Montana, U-Pb zircon analysis of quartzofeldspathic gneiss near Maiden Peak found two distinct zircon age-populations. Within one sample (04NA16) the oldest zircons were dated to ca. 2789 Ma (interpreted to have formed during the Beartooth orogeny), with ca. 2497 Ma metamorphic rims attributed to plutonism and metamorphism during the Tendoy orogeny. Two other samples (02NA16 and 03NA16) of quartzofeldspathic gneiss from Maiden Peak returned unimodal U-Pb zircon crystallization ages of 2477 ± 25 Ma and 2483 ± 23 Ma. These two dates are encompassed in the ca. 2497 Ma metamorphic age peak (rims) from sample 04NA16, which is interpreted to indicate that magmatism in samples 02NA16 and 03NA16 was concurrent with metamorphism during the Tendoy orogeny. All three of these gneisses are interpreted as being derived from an igneous protolith.

Geologic mapping of the Bloody Dick gneiss has revealed four units of gneiss. Several lines of evidence suggest original igneous protoliths for all gneiss samples studied here, including: unimodal zircon populations with younger, metamorphic overgrowths, the lack of pelitic minerals, abundance of minerals indicative of an originally igneous protolith (e.g., abundant feldspar that is up to 1 cm, abundant hornblende), and euhedral to subhedral zircon grain morphologies. The oldest unit is the banded gneiss (25NA16), which contains ca. 2476 Ma zircon cores and ca. 1761 Ma metamorphic rims with U-Th ratios as high as 21.3. Zircons in the banded gneiss unit of the Bloody Dick gneiss (25NA16) and the quartzofeldspathic gneiss (03NA16) in Maiden Peak share similar quartzofeldspathic minerology and have indistinguishable U-Pb zircon ages of ca. 2478 Ma and initial, juvenile, εHf values of +2 to -4. This is interpreted as

evidence for correlation between the banded gneiss of the Bloody Dick unit and quartzofeldspathic gneiss in Maiden Peak. In the Bloody Dick gneiss, hornblende gneiss (08RL647, BDC4, BDC5) intruded country rock or was erupted at ca. 1878-1900 Ma. This unit was subsequently intruded at 1802 ± 17 Ma by an isotopically juvenile, felsic magma body.

The Bloody Dick gneiss was exhumed in the hanging wall of the Monument thrust (the eastern strand of the Beaverhead Divide fault) during the Late Cretaceous, as shown by a zircon (U-Th)/He age of 72.4 ± 1.5 Ma. North of the Bloody Dick gneiss, a portion of this fault was reactivated as a normal fault in Cenozoic time, though field observations suggest that the section of this fault south of Bloody Dick Canyon has not been recently active.

Similarities in U-Pb and Lu-Hf isotopic values of ca. 2478 Ma gneisses in the Bloody Dick gneiss and quartzofeldspathic gneiss from Maiden Peak suggests that they fundamentally belong to the same basement province. Younger hornblende gneiss and felsic orthogneisses within the Bloody Dick gneiss are Paleoproterozoic in age and isotopically juvenile (initial εHf values of +3 to -7), which is similar to rocks from the Little Belt Mountains, which were interpreted to have formed during arc magmatism above the northwest-dipping subduction of oceanic lithosphere beneath the Medicine Hat block during the 1860 to 1790 Ma Great Falls orogeny. This correlation of arc-related rocks between the Little Belt Mountains and the Bloody Dick gneiss suggests that the Great Falls tectonic zone projects into southwest Montana at least as far as the Bloody Dick gneiss. This work also establishes a crosscutting relationship between these

isotopically juvenile rocks of the Bloody Dick gneiss and the country rock into which they intruded, which has strong affinities to the Wyoming craton.

Works cited

Baldwin, J.A., Cramer, M.A. and Voarino, B., 2014, Late Archean to Paleoproterozoic evolution of the Ruby Range, Montana, and its implications for the growth and modification of the northwestern Wyoming province, Geological Society of America Abstracts with Programs, Vol. 46, No. 5, p.20.

Bennett, E.H., 1986, Relationship of the trans-Challis fault system in central Idaho to Eocene and Basin and Range extensions: Geology, v. 14, p. 481.

Bouvier, A., Vervoort, J.D., and Patchett, P.J., 2008, The Lu-Hf and Sm-Nd isotopic composition of CHUR: Constraints from unequilibrated chondrites and implications for the bulk composition of terrestrial planets: Earth and Planetary Science Letters, v. 273, p. 48–57.

Buhlmann, A.L., Cavell, P., Burwash, R.A., Creaser, R.A., and Luth, R.W., 2000, Minette bodies and cognate mica-clinopyroxene xenoliths from the Milk River area, southern Alberta: Records of a complex history of the northernmost part of the Wyoming craton: Canadian Journal of Earth Sciences, v. 37, p. 1629–1650.

Burmester, R.F., Lonn, J.D., Lewis, R.S., and McFaddan, M.D., 2016, Stratigraphy of the Lemhi subbasin of the Belt Supergroup, *in* MacLean, J.S., and Sears, J.W., eds., Belt Basin: Window to Mesoproterozoic Earth: Geological Society of America Special Paper 522, p.

Canadian Nuclear Safety Commission, 2012, Polonium-210, Retrieved from: http://nuclearsafety.gc.ca/eng/resources/fact-sheets/polonium-210.cfm.

Chamberlain, K., Frost, C., and Frost, R., 2003, Early Archean to Mesoproterozoic evolution of the Wyoming Province: Archean origins to modern lithospheric architecture: Canadian Journal of Earth Sciences, v. 40, p. 1357–1374.

Cheney, J.T., Webb, A., Coath, C., and McKeegan, K., 2004, In situ ion micro- probe 207 Pb/ 206 Pb dating of monazite from Precambrian metamorphic rocks, Tobacco Root Mountains, Montana, in Brady, J.B., Burger, H.R., Cheney, J.T., and Harms, T.A., eds., Precambrian Geology of the Tobacco Root Mountains, Montana: Geological Society of America Special Paper 377, p. 151–179.

Cherniak, D., and Watson, E.B., 2000, Pb diffusion in zircon: Chemical Geology, v. 172, p. 5–24.

Condit, C.B., Mahan, K.H., Ault, A.K., and Flowers, R.M., 2015, Foreland-directed propagation of high-grade tectonism in the deep roots of a Paleoproterozoic collisional orogen, SW Montana, USA: Lithosphere, v. 7, p. 625–645.

Coppinger, W., 1974, Stratigraphy and Structural Study of Belt Supergroup and Associated Rocks in a Portion of the Beaverhead Mountains, Southwest- ern Montana and East-Central Idaho [Ph.D. dissertation]: Oxford, Ohio, Miami University, 224 p.

Cramer, M., 2015, Proterozoic tectonometamorphic evolution of the Ruby Range, SW Montana, USA: Insights from phase equilibria modeling and in situ monazite petrochronology: University of Montana, M.S. thesis, 120 p.

D'Amato, E., 1994, Petrology and geochemistry of the Dillon quartzofeldspathic gneiss, Ruby Range, southwest Montana. Unpublished MS thesis, Kent State University, Kent, OH, 98 p.

DeCelles, P.G., 2004, Late Jurassic to Eocene evolution of the Cordilleran thrust belt and foreland basin system, western USA: American Journal of Science, v. 304, p. 105-168.

Doughty, P.T., and Chamberlain, K.R., 1996, Salmon River arch revisited: new evidence for 1370 Ma rifting near the end of deposition in the Middle Proterozoic Belt basin: Canadian Journal of Earth Sciences, v. 33, p. 1037-1052.

Evans, K.V., Aleinikoff, J.N., Obradovich, J.D., Fanning C.M., 2000, SHRIMP U-Pb geochronology of volcanic rocks, Belt Supergroup, western Montana: evidence for rapid deposition of sedimentary strata: Canadian Journal of Earth Sciences v. 37, p.1287-1300.

Farley, K.A., Wolf, R.A. and Silver, L.T., 1996, The effects of long alpha-stopping distances on (U-Th)/He ages: Geochim Cosmochim Acta 60:4223-4229.

Foster, D.A., and Fanning, C.M., 1997, Geochronology of the northern Idaho Batholith and the Bitterroot metamorphic core complex: Magmatism preceding and contemporaneous with extension: Geological Society of America Bulletin, v. 109, no. 4, p. 379–394.

Foster, D.A., Mueller, P.A., Mogk, D.W., Wooden, J., and Vogl, J.J., 2006, Proterozoic evolution of the western margin of the Wyoming craton: implications for the tectonic and magmatic evolution of the northern Rocky Mountains: Canadian Journal of Earth Sciences, v. 43, p. 1601–1619.

Gaschnig, R.M., Vervoort, J.D., Lewis, R.S., and McClelland , W.C., 2010, Migrating magmatism in the northern US Cordillera: In situ U-Pb geochronology of the Idaho batholith: Contributions to Mineralogy and Petrology, v. 159, p. 863–883.

Gaschnig, R.M., Vervoort, J.D., Lewis, R.S., and Tikoff, B., 2013, Probing for Proterozoic and Archean crust in the Northern U.S. Cordillera with inherited zircon from the Idaho batholith: Geological Society of America Bulletin, v. 125, p. 73–88.

Garihan, J.M. and Okuma, A.R., 1974. Field evidence suggesting a non-igneous origin for the Dillon quartzofeldspathic gneiss, Ruby Range, southwestern Montana. Geological Society of America Abstracts with Programs, 6(6), A510.

Geach, R.D., 1972, Mines and mineral deposits (except fuels) Beaverhead County, Montana: Montana Bureau of Mines and Geology Bulletin 85, 194 p.

Gehrels, G., 2010, U-Th-Pb analytical methods for Zircon (Arizona LaserChron Center, University of Arizona), 11 p.

Gehrels, G., 2012, Hf analytical methods at the (Arizona LaserChron Center, University of Arizona), 13 p.

Gorman, A.R., Clowes, R.M., Ellis, R.M., Henstock, T.J., Spence, G.D., Keller, G.R., Levander, A., Snelson, C.M., Burianyk, M.J.A., Kanasewich, E.R., Asudeh, I., Hajnal, Z., and Miller, K.C., 2002, Deep probe: Imaging the roots of western North America: Canadian Journal of Earth Sciences, v. 39, p. 375–398.

Hahn, G.A., and Huges, G.J., Jr., 1984, Sedimentation, tectonism, and associated magmatism of the Yellowjacket Formation in the Idaho Cobalt Belt, Lemhi County, Idaho, *in* Hobbs, S.W., editor, The Belt: Montana Bureau of Mines and Geology, Special Publication 90, p. 65– 67.

Hansen, P.M., 1983, Structure and Stratigraphy of the Lemhi Pass Area, Beaverhead Range, Southwest Montana and East-Central Idaho [M.S. thesis]: University Park, Pennsylvania, The Pennsylvania State University, 112 p.

Harms, T.A., Brady, J.B., Burger, H.R., and Cheney, J.T., 2004, Advances in the geology of the Tobacco Root Mountains, Montana, and their implications for the history of the northern Wyoming Province, in Brady, J.B., Burger, H.R., Cheney, J.T., and Harms, T.A., eds., Precambrian Geology of the Tobacco Root Mountains, Montana: Geological Society of America Special Paper 377, p. 227–243.

Harms, T.A., Brady, J.B., Cheney, J.T., and College, A., 2006, Exploring the Proterozoic Big Sky Orogeny in Southwest Montana: 19th Annual Keck Symposium, p. 171–176. http://keck.wooster.edu/publications.

Heinrich, E.W., 1949, Sillimanite deposits in the Dillon region, Montana: Montana Bureau of Mines and Geology Memoir 30, 43 p.

Hourigan, J.K., Reiners, P.W. and Brandon, M.T., 2005, U-Th zonation dependent alpha-ejection in (U-Th)/He chronometry, Part I: Theory: Geochim Cosmochim Acta 69:3349-3365.

James, H.L., 1990, Precambrian geology and bedded iron deposits of the southwestern Ruby Range, Montana: U.S. Geological Survey Professional Paper, v. 1495.

James, H.L. and Hedge, C.E., 1980, Age of basement rocks in southwest Montana: Geological Society of America Bulletin, v. 91, p. 11–15.

Jamison, W.R., 1987, Geometric analysis of fold development in overthrust terranes: Journal of Structural Geology, v. 9, no. 2, p. 207–219.

Janecke, S.U., 1992, Kinematics and timing of three superposed extensional systems, east central Idaho: Evidence for an Eocene tectonic transition: Tectonics, v. 11, p. 1121–1138.

Jones, C., 2008, U-Pb geochronology of monazite and zircon in Precambrian metamorphic rocks from the Ruby Range, SW Montana: Deciphering geological events that shaped the NW Wyoming province: 119 p: Kent State University, M.S. thesis.

Kellogg, K.S., Snee, L.W., and Unruh, D.M., 2003, The Mesoproterozoic Beaverhead Impact structure and its tectonic setting, Montana-Idaho: 40Ar/39Ar and U/Pb Isotopic constraints: Journal of Geology, v. 111, p. 639–652.

Lewis, R.S., Kiilsgaard, T.H., Bennett, E.H., and Hall, W.E., 1987, Lithologic and chemical characteristics of the central and southeastern part of the southern lobe of the Idaho Batholith, *in* Vallier, T.L. and Brooks, H.C., eds., Geology of the Blue Mountains Region of Oregon, Idaho, and Washington: The Idaho Batholith and its border zone, U. S. Geological Survey Professional Paper 1436, p. 171-196.

Link, P.K., and Janecke, S.U., 1999, Geology of East-Central Idaho: Geologic Roadlogs for the Big and Little Lost River, Lemhi, and Salmon River Valleys, *in* Hughes, S.S. and Thackray, G.D. eds., Guidebook to the Geology of Eastern Idaho, Pocatello, Idaho Museum of Natural History, p. 295–334.

Link, P.K., Stewart, E. D., Steel, T., Sherwin,J., Hess, L.T., and McDonald, C., 2016, Detrital zircons in the Mesoproterozoic upper Belt Supergroup in the Pioneer, Beaverhead and Lemhi Ranges, MT and ID: The Big White arc: *in* MacLean, J., and Sears, J.D., eds., Belt Supergroup: Window to the Proterozoic World, Geological Society of America Special Paper 522, p. 163–183.

Lonn, J.D., Skipp, Betty, Ruppel, E.T., Perry Jr, W.J., Sears, J.W., Janecke, S.U., Bartholomew, M.J., Stickney, M.C., Fritz, W.J., Hurlow, H.A., and Thomas, R.C., 2000, Geologic map of the Lima 30'x60' quadrangle, Montana Bureau of Mines and Geology Open-File Reports MBMG-408, scale 1:100,000.

Lonn, J.D., and Lewis, R.S., 2009, Late Cretaceous extension and its relation to the thin stratigraphic section in the Philipsburg region: A field trip to Carpp Ridge: Northwest Geology, v. 38, p.141-151.

Lonn, J.D., Burmester, R.F., Lewis, R.S., and McFaddan, M.D., 2016, Giant folds and complex faults in Mesoproterozoic Lemhi strata of the Belt Supergroup, northern Beaverhead Mountains, Montana and Idaho, in MacLean, J.S., and Sears, J.W., eds., Belt Basin: Window to Mesoproterozoic Earth: Geological Society of America Special Paper 522, p. 1–24.

Lonn, J.D., Elliott, C.G., Lewis R.S., Burmester, R.F., McFaddan, M.D., Stanford, L.R., Janecke, S.U., Othberg, K.L., in preparation, Geologic Map of the Salmon 30'x60' quadrangle, Montana and Idaho, Montana Bureau of Mines and Geology.

Lucchitta, B.K., 1966, Structure of the Hawley Creek area, Idaho- Montana: Pennsylvania State Univ. Ph. D. thesis.

Ludwig, K.R., 2012, Isoplot: Berkeley Geochronology Center, Special Publication.

Lyons, T.W., Lupke, J.J., Schrieber, M.E., and Zieg, G.A., 2000, Sulfur geochemical constraints on Mesoproterozoic restricted marine deposition: Lower Belt Supergroup, northwestern United States: Geochimica et Cosmochimica Acta, v. 64, p. 427–437.

Martin, A.J., Burgy, K.D., Kaufman, A.J., and Gehrels, G.E., 2011, Stratigraphic and tectonic implications of field and isotopic constraints on depositional ages of Proterozoic Lesser Himalayan rocks in central Nepal: Precambrian Research, v. 185, p. 1–17.

M'Gonigle, J.W., 1965, Structure of the Maiden Peak area, Montana-Idaho: The Pennsylvania State University, Department of Geosciences, 146 p, Ph.D. thesis.

M'Gonigle J.W., Darlrymple, G.B., 1996, 40Ar/39Ar ages of some Challis Volcanic Group rocks and the initiation of Tertiary sedimentary basins in southwestern Montana, United States Geological Survey Bulletin, v. 2132.

M'Gonigle, J.W., and Hait, M.H., Jr., 1997, Geologic map of the Jeff Davis Peak quadrangle and eastern part of the Everson Creek quadrangle, Beaverhead County, southwest Montana: U.S. Geological Survey Geologic Investigations Map I–2604, scale 1:24,000.

Mogk, D.W., Mueller, P.A., and Wooden, J.L., 1992, The nature of terrane boundaries: An example from the northern Wyoming province: Precambrian Research, v. 55, p. 155–168.

Moye, F.J., Hackett, W.R., Blakey, J.D., and Snider, L.G., 1988, Regional geologic setting and volcanic stratigraphy of the Challis volcanic field, central Idaho, *in* Link, P. K., and Hackett, W.R., eds., Guidebook to the Geology of Central and Southern Idaho: Idaho Geological Survey Bulletin 27, p. 87-97.Mueller, P.A., Wooden, J.L., Mogk, D.W., Nutman, A.P., and Williams, I.S. 1996. Extended history of a 3.5 Ga trondhjemitic gneiss, Wyoming province, USA: Evidence from U–Pb systematics in zircon. Precambrian Research, 78, p. 41–52.

Mueller, P.A., Heatherington, A.L., Kelly, D.M., Wooden, J.L., and Mogk, D.W., 2002, Paleoproterozoic crust within the Great Falls tectonic zone: Implications for the assembly of southern Laurentia: Geology, v. 30, p. 127–130.

Mueller, P.A., Burger, H.R., Wooden, J.L., Brady, J.B., Cheney, J.T., Harms, T.A., Heatherington, A.L., and Mogk, D.W., 2005, Paleoproterozoic metamorphism in the northern Wyoming Province: Implications for the assembly of Laurentia: The Journal of Geology, v. 113, p. 169–179.

Mueller, P.A., Wooden, J.L., Mogk, D.W., and Foster, D., 2011, Paleoproterozoic evolution of the Farmington zone: Implications for terrane accretion in southwestern Laurentia: Lithosphere, v. 3, p. 401–408.

Mueller, P., Mogk, D.W., Wooden, J.L., 2012. Age and composition of crystalline basement in the Armstead anticline, southwestern Montana. Northwest Geology 41, 63-70.

Mueller, P.A., Mogk, D.W., Wooden, J., and Spake, D., 2016, U-Pb ages of zircons from the Lower Belt Supergroup and proximal crystalline basement: Implications for the early evolution of the Belt Basin, *in* MacLean, J.S., and Sears, J.W., eds., Belt Basin: Window to Mesoproterozoic Earth: Geological Society of America Special Paper 522, p. 283–303.

O'Neill, J.M., 1998, The Great Falls tectonic zone, Montana-Idaho: An Early Proterozoic collisional orogen beneath and south of the Belt basin, in Berg, R.B., ed., Belt Symposium III—1993: Montana Bureau of Mines and Geology Special Publication 112, p. 222–228.

O'Neill, J.M., Lopez, D.A., 1985, Character and significance of Great Falls tectonic zone, east-central Idaho and west-central Montana: American Association of Petroleum Geologists Bulletin, v. 69, p. 437–447.

O'Neill, J.M., Ruppel, E.T., and Lopez, D.A., 2007, Great Divide Megashear, Montana, Idaho, and Washington—An Intraplate Crustal-Scale Shear Zone Recurrently Active since the Mesoproterozoic: U.S. Geological Survey Open-File Report 2007-1280-A, 10 p.

Proffett, J.M., 1977, Cenozoic geology of the Yerington district, Nevada, and implications for the nature and origin of Basin and Range faulting: Geological Society of America Bulletin, v. 88, no. 2, p. 247–266.

Reid, R.R., McMannis, W.J., and Palmquist, J.C., 1975, Precambrian geology of North Snowy Block, Beartooth Mountains, Montana: Geological Society of America Special Paper 157, 135 p.

Reiners, P.W., 2005, Zircon (U-Th)/He Thermochronometry: Reviews in Mineralogy and Geochemistry, v. 58, p. 151–179.

Reiners, P.W. and Nicolescu, S., 2006, Measurement of parent nuclides for (U-Th)/He chronometry by solution sector ICP-MS, ARHDL Report 1, http://www.geo.arizona.edu/~reiners/arhdl/arhdl.htm.

Reiners, P.W., Spell, T.L., Nicolescu, S., and Zanetti, K.A., 2004, Zircon (U-Th)/He thermochronometry: He diffusion and comparisons with Ar-40/Ar-39 dating: Geochimica Et Cosmochimica Acta, v. 68, no. 8, p. 1857–1887.

Roberts, H., Dahl, P., Kelley, S., and Frei, R., 2002, New 207 Pb-206 Pb and 40 Ar-39 Ar ages from SW Montana, USA: Constraints on the Proterozoic and Archaean tectonic and depositional history of the Wyoming Province: Precambrian Research, v. 117, no. 1–2, p. 119– 143.

Rodgers, D.W., Ore, H.T., Bobo, R.T., McQuarrie, N., and Zentner, N., 2002, Extension and subsidence of the eastern Snake River Plain, Idaho, in Bonnichsen, B., White, C.M., and McCurry, M., eds., Tectonic and Magmatic Evolution of the Snake River Plain Volcanic Province: Idaho Geological Survey Bulletin 30, p. 121–155.

Ross, G.M., and Parrish, R.R., 1991, Detrital zircon geochronology of metased- imentary rocks in the southern Omineca Belt, Canadian Cordillera: Cana- dian Journal of Earth Sciences, v. 28, p. 1254–1270.

Ruppel, E.T., 1986, The Lemhi Arch: A late Proterozoic and early Paleozoic landmass in central Idaho: Part II. Northern Rocky Mountains. American Association of Petroleum Geologists Bulletin. A115, p. 119–130.

Ruppel, E.T., O'Neill, J.M., and Lopez, D.A., 1993, Geologic map of the Dillon 1x2 degree quadrangle, Idaho and Mon- tana: U.S. Geological Survey Miscellaneous Field Investiga- tions Series Map I–1803–H, scale 1:250,000.

Sanford, R.F., 2005, Geology and stratigraphy of the Challis Volcanic Group and related rocks, Little Wood River area, south-central Idaho: U.S. Geological Survey Bulletin 2064-II, 22 p.

Schmid, R, Fettes, D., Harte, B, Davis E. and Desmons, J., 2007, A systematic nomenclature for metamorphic rocks: How to name a metamorphic rock. Recommendations by the IUGS Subcommission on the Systematics of Metamorphic Rocks. *Recommendations*, web version 01.02.2007.

Sears, J.W., Chamberlain, K.R., and Buckley, S.N., 1998, Structural and U- Pb geochronological evidence for 1.47 Ga rifting in the Belt basin, western Montana: Canadian Journal of Earth Sciences, v. 35, p. 467– 475.

Sherwin, J., Younggren, E.B., Link, P.K., and Gaschnig, R.M., 2016, Geologic map of the Coyote Creek 7.5' quadrangle, southwest Montana: Montana Bureau of Mines and Geology Map GM-67, scale 1:24,000.

Skinner, W.R., Bowes, D.R., and Khoury, S.G., 1969, Polyphase deformation in the Archean basement complex, Beartooth Mountains, Montana and Wyoming: Geological Society of America Bulletin, v. 80, p. 1053-1060.

Skipp, B.,1988, Cordilleran thrust belt and faulted foreland in the Beaverhead Mountains, Idaho and Montana, Interaction of the Rocky Mountain foreland and the Cordilleran thrust belt: *in* Schmidt, C.J., Perry, W.Jr., eds., Interaction of the Rocky Mountain foreland and the Cordilleran thrust belt, Geological Society of America Memoir 171, p. 237–266.

Thompson, R.N., Morrison, M.A., Hendry, G.L., Parry, S.J., Simpson, P.R., Hutchison, R., and Hara, M.J., 1984, An Assessment of the Relative Roles of Crust and Mantle in Magma Genesis: An Elemental Approach: Philosophical Transactions of the Royal Society of London. Series A, Mathematical and Physical Sciences, v. 310, i. 1514, p. 549 LP-590.

VanDenburg, C.J., 1997, Cenozoic tectonic and paleogeographic evolution of the Horse Prairie half-graben, southwest Montana: Logan, Utah, Utah State University M.S. thesis, 151 p., 2 plates.

VanDenburg, C.J., Janecke, S.U., and McIntosh, W.C., 1998, Three-dimensional strain produced by >50 My of episodic extension, Horse Prairie basin area, southwest Montana, United States: Journal of Structural Geology, v. 20, p. 1747–1767.

Vervoort, J.D., Lewis, R.S., Fisher, C., Gaschnig, R.M., Jansen, A.C., and Brewer, R., 2015, Neoarchean and Paleoproterozoic crystalline basement rocks of north-central Idaho: Constraints on the formation of western Laurentia: Geological Society of America Bulletin, v. 128, p. 94–109.

Wan, Y., Liu, D., Dong, C., Liu, S., Wang, S., and Yang, E., 2011, U-Th-Pb behavior of zircons under high-grade metamorphic conditions: A case study of zircon dating of meta-diorite near Qixia, eastern Shandong: Geoscience Frontiers, v. 2, p. 137–146.

Winkler, H.G.F., 2013, Petrogenesis of Metamorphic Rocks: Springer New York.

Wooden, J., Mueller, P.A, 1988. Pb, Sr, and Nd isotopic compositions of a suite of Late Archean, igneous rocks, eastern Beartooth Mountains: implications for crust-mantle evolution. Earth and Planetary Sciences Letters, 87, 59-72.

Appendix A: Annotated backscattered electron (BSE) images

Appendix A includes the backscattered electron images of the five zircon samples; 02NA16, 03NA16 and 04NA16 of the quartzofeldspathic gneiss from the Maiden Peak area. Samples 18NA16 and 25NA16 were collected from the Bloody Dick gneiss in the Beaverhead Range. These BSE images have been annotated to include an illustration of ICP-MS spot location and the accompanying U-Pb date.

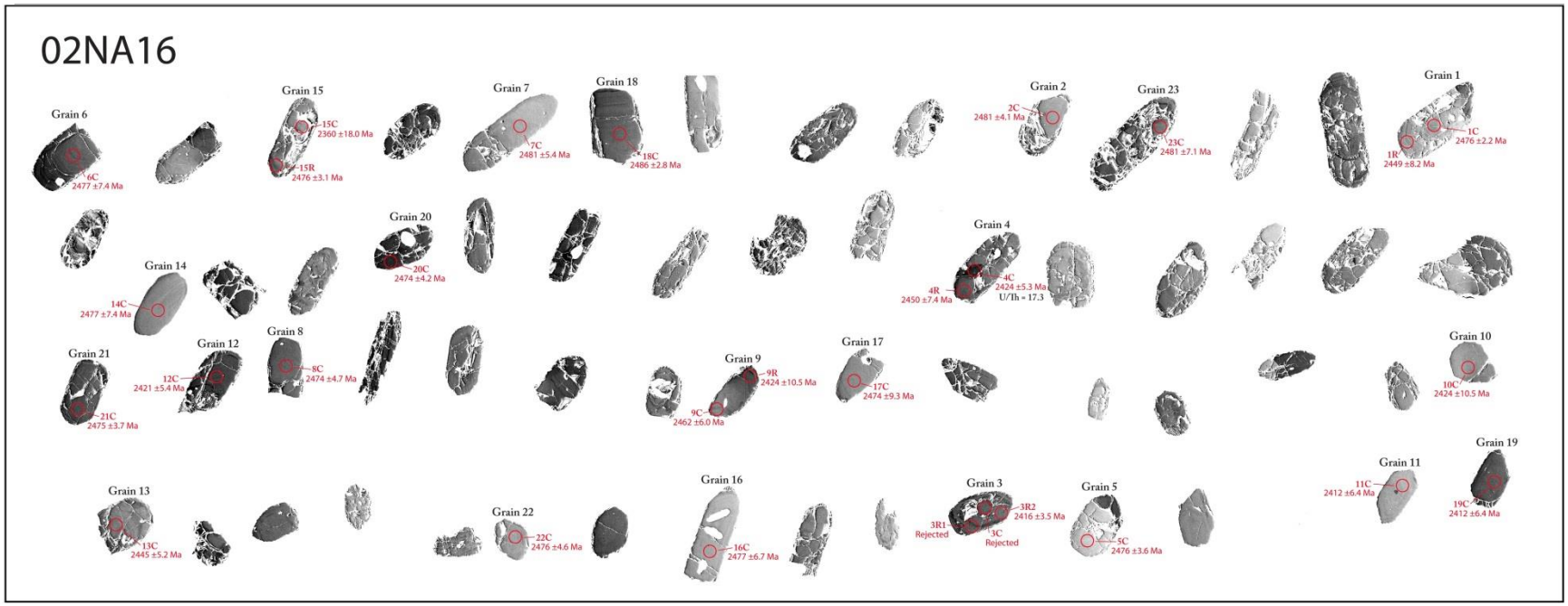
02NA16
Grain 6
6C
2477 ±7.4 Ma
Grain 15
15C
2360 ±18.0 Ma
15R
2476 ±3.1 Ma
Grain 7
7C
2481 ±5.4 Ma
Grain 18
18C
2486 ±2.8 Ma
Grain 2
2C
2481 ±4.1 Ma
Grain 23
23C
2481 ±7.1 Ma
Grain 1
1C
2476 ±2.2 Ma
1R
2449 ±8.2 Ma
Grain 20
20C
2474 ±4.2 Ma
Grain 14
14C
2477 ±7.4 Ma
Grain 4
4C
2424 ±5.3 Ma
U/Th = 17.3
4R
2450 ±7.4 Ma
Grain 8
8C
2474 ±4.7 Ma
Grain 12
12C
2421 ±5.4 Ma
Grain 21
21C
2475 ±3.7 Ma
Grain 9
9R
2424 ±10.5 Ma
9C
2462 ±6.0 Ma
Grain 17
17C
2474 ±9.3 Ma
Grain 10
10C
2424 ±10.5 Ma
Grain 19
19C
2412 ±6.4 Ma
Grain 11
11C
2412 ±6.4 Ma
Grain 13
13C
2445 ±5.2 Ma
Grain 22
22C
2476 ±4.6 Ma
Grain 16
16C
2477 ±6.7 Ma
Grain 3
3R2
2416 ±3.5 Ma
3R1
Rejected
3C
Rejected
Grain 5
5C
2476 ±3.6 Ma

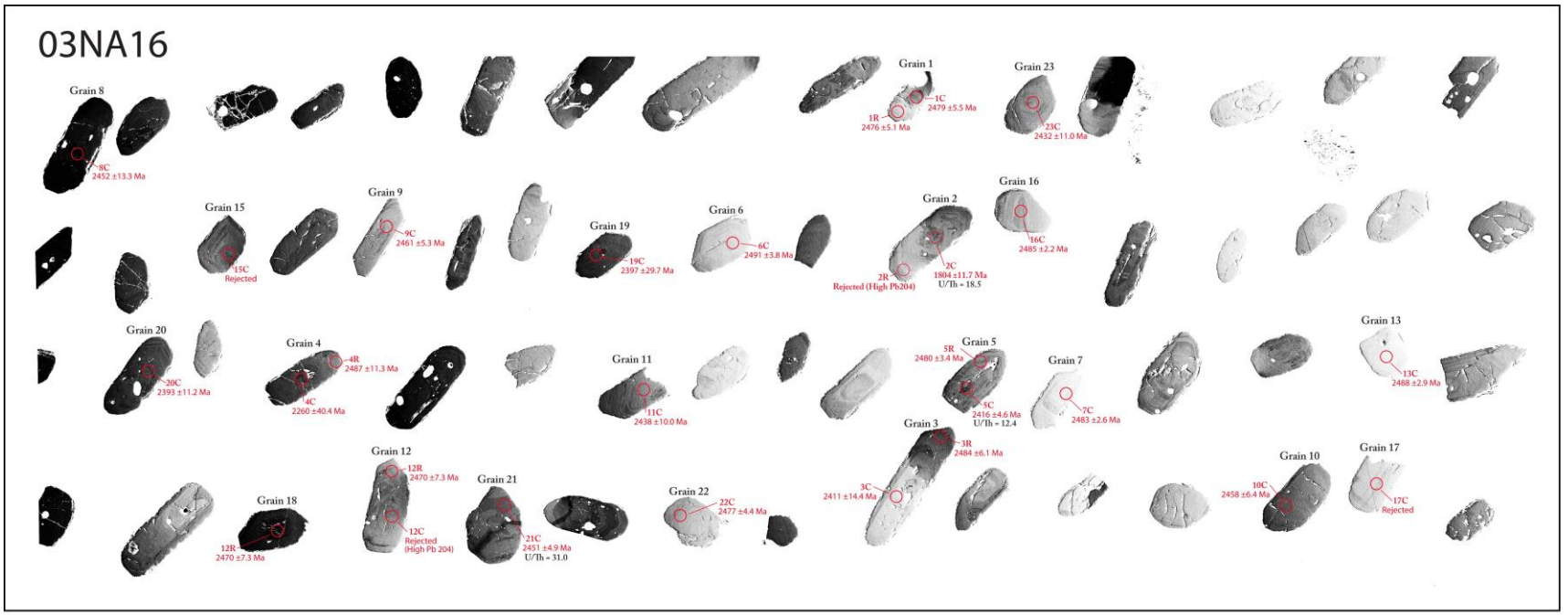
03NA16
Grain 8
8C
2452 ±13.3 Ma
Grain 1
1C
2479 ±5.5 Ma
1R
2476 ±5.1 Ma
Grain 23
23C
2432 ±11.0 Ma
Grain 15
15C
Rejected
Grain 9
9C
2461 ±5.3 Ma
Grain 19
19C
2397 ±29.7 Ma
Grain 6
6C
2491 ±3.8 Ma
Grain 2
2C
1804 ±11.7 Ma
U/Th = 18.5
2R
Rejected (High Pb204)
Grain 16
16C
2485 ±2.2 Ma
Grain 20
20C
2393 ±11.2 Ma
Grain 4
4R
2487 ±11.3 Ma
4C
2260 ±40.4 Ma
Grain 11
11C
2438 ±10.0 Ma
Grain 5
5R
2480 ±3.4 Ma
5C
2416 ±4.6 Ma
U/Th = 12.4
Grain 7
7C
2483 ±2.6 Ma
Grain 13
13C
2488 ±2.9 Ma
Grain 3
3R
2484 ±6.1 Ma
3C
2411 ±14.4 Ma
Grain 12
12R
2470 ±7.3 Ma
12C
Rejected
(High Pb 204)
Grain 21
21C
2451 ±4.9 Ma
U/Th = 31.0
Grain 22
22C
2477 ±4.4 Ma
Grain 18
12R
2470 ±7.3 Ma
Grain 10
10C
2458 ±6.4 Ma
Grain 17
17C
Rejected

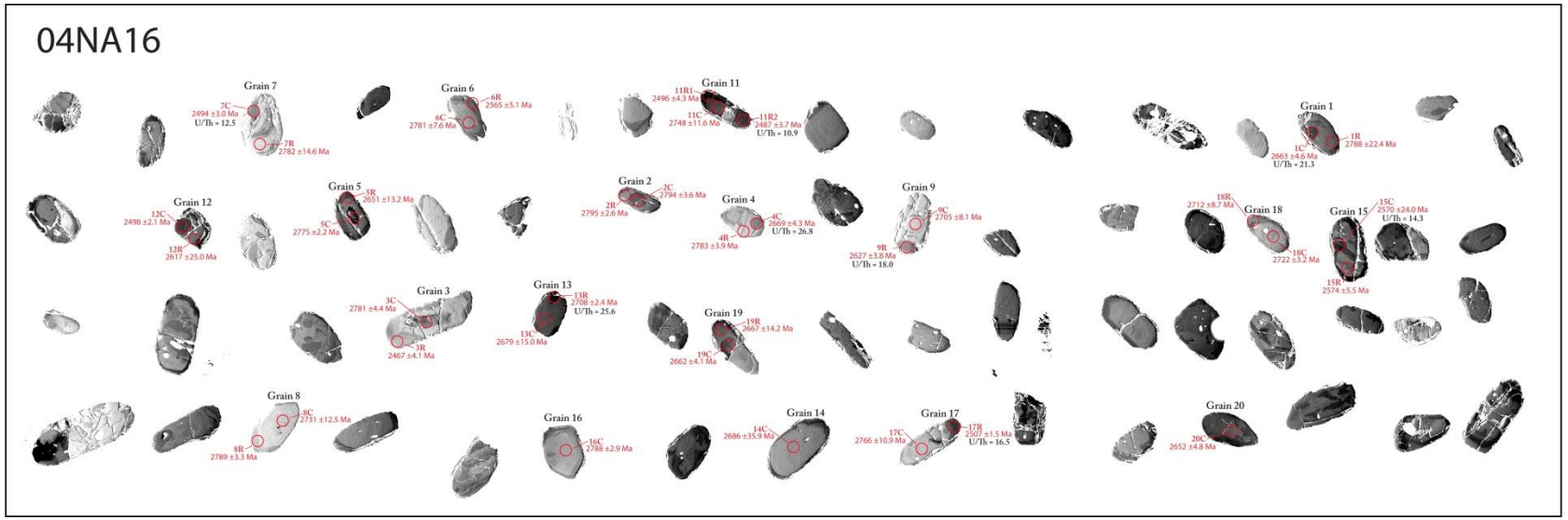
04NA16
Grain 7
7C
2494 ±3.0 Ma
U/Th = 12.5
7R
2782 ±14.6 Ma
Grain 6
6R
2565 ±5.1 Ma
6C
2781 ±7.6 Ma
Grain 11
11R1
2496 ±4.3 Ma
11C
2748 ±11.6 Ma
11R2
2487 ±3.7 Ma
U/Th = 10.9
Grain 1
1R
2788 ±22.4 Ma
1C
2663 ±4.6 Ma
U/Th = 21.3
Grain 12
12C
2498 ±2.1 Ma
12R
2617 ±25.0 Ma
Grain 5
5R
2651 ±13.2 Ma
5C
2775 ±2.2 Ma
Grain 2
2C
2794 ±3.6 Ma
2R
2795 ±2.6 Ma
Grain 4
4C
2669 ±4.3 Ma
U/Th = 26.8
4R
2783 ±3.9 Ma
Grain 9
9C
2705 ±8.1 Ma
9R
2627 ±3.6 Ma
U/Th = 18.0
18R
2712 ±8.7 Ma
Grain 18
18C
2722 ±3.2 Ma
Grain 15
15C
2570 ±24.0 Ma
U/Th = 14.3
15R
2574 ±5.5 Ma
Grain 3
3C
2781 ±4.4 Ma
3R
2467 ±4.1 Ma
Grain 13
13R
2708 ±2.4 Ma
U/Th = 25.6
13C
2679 ±15.0 Ma
Grain 19
19R
2667 ±14.2 Ma
19C
2662 ±4.1 Ma
Grain 8
8C
2731 ±12.5 Ma
8R
2789 ±3.3 Ma
Grain 16
16C
2788 ±2.9 Ma
Grain 14
14C
2686 ±35.9 Ma
Grain 17
17C
2766 ±10.9 Ma
17R
2507 ±1.5 Ma
U/Th = 16.5
Grain 20
20C
2652 ±4.8 Ma


18NA16
Grain 1
1R
2359 ±10.1 Ma
1C
2359 ±10.1 Ma
Grain 3
3R
1797 ±6.3 Ma
3C
Rejected
Grain 19
19R
1798 ±12.7 Ma
19C
1803 ±5.0 Ma
Grain 2
2R
1796 ±4.9 Ma
2C
1753 ±6.0 Ma
Grain 4
4R1
1795 ±5.9 Ma
4C2
1805 ±1.8 Ma
4C1
1802 ±2.8 Ma
4R2
1788 ±4.4 Ma
Grain 5
5R
1802 ±5.5 Ma
5R
1759 ±11.3 Ma
Grain 6
6C
1803 ±4.8 Ma
6R
1793 ±5.9 Ma
Grain 7
7C
1802 ±4.7 Ma
7R
Rejected
Grain 10
10C
1761 ±24.4 Ma
10R
1786 ±5.2 Ma
Grain 8
8C
1804 ±3.1 Ma
8R
1804 ±7.7 Ma
Grain 20
20R
1805 ±3.6 Ma
20C
1786 ±4.8 Ma
Grain 12
12C
1788 ±4.4 Ma
12R
1810 ±4.3 Ma
Grain 13
13C
1814 ±9.9 Ma
13R
1802 ±9.2 Ma
Grain 9
9C
1800 ±2.4 Ma
9R
1783 ±12.5 Ma
Grain 18
18R
1797 ±8.2 Ma
18C
Rejected
Grain 11
11C
1839 ±116.2 Ma
11R
1804 ±9.8 Ma
Grain 15
15R
1619 ±9.5 Ma
15C
2258 ±52.5 Ma
Grain 17
17R
1767 ±12.9 Ma
17C
1777 ±13.3 Ma

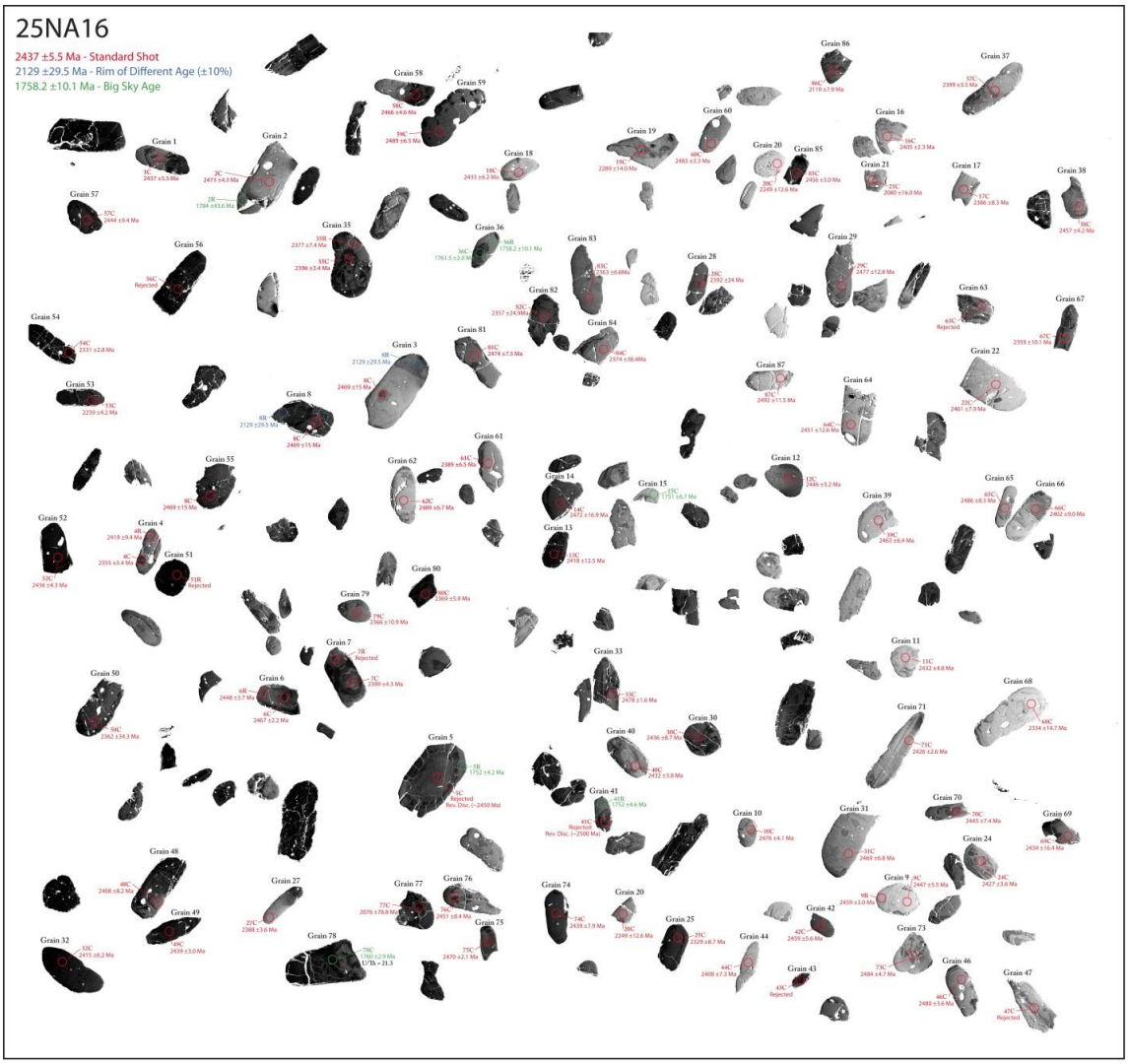
25NA16
2437 ±5.5 Ma - Standard Shot
2129 ±29.5 Ma - Rim of Different Age (±10%)
1758.2 ±10.1 Ma - Big Sky Age

Appendix B: U-Pb Analysis.

Appendix B includes a table of sample locations and U-Pb zircon analysis of samples 02NA16, 03NA16 and 04NA16 of the quartzofeldspathic gneiss from the Maiden Peak area. Samples 18NA16 and 25NA16 were collected from the Bloody Dick gneiss in the Beaverhead Range.

Sample ID	UTM Easting (Z12)	UTM Northing (Z12)	Lat. (north)	Long. (west)	Elev.(ft.)
02NA16	32882	49717	44.8786	113.1673	7885
03NA16	32902	49720	44.8818	113.1648	7830
04NA16	32861	49754	44.9115	113.1712	8195
18NA16	31500	49867	45.0102	113.3476	7185
25NA16	31505	49829	44.9758	113.3456	7003

02NA16				Isotope ratios							Apparent ages (Ma)								
Analysis	U (ppm)	206Pb 204Pb	U/Th	206Pb* 207Pb*	± (%)	207Pb* 235U*	± (%)	206Pb* 238U	± (%)	error corr.	206Pb* 238U*	± (Ma)	207Pb* 235U	± (Ma)	206Pb* 207Pb*	± (Ma)	Best age (Ma)	± (Ma)	Conc (%)
02NA16-17C	162	567366	1.9	6.9519	0.5	7.9737	2.2	0.4020	2.1	0.97	2178.4	38.7	2228.1	19.5	2274.0	9.3	2274.0	9.3	95.8
02NA16-15C	94	187487	2.0	6.6116	1.1	9.3844	1.6	0.4500	1.2	0.75	2395.3	23.8	2376.3	14.6	2360.1	18.0	2360.1	18.0	101.5
02NA16-19C	138	137278	2.3	6.4127	0.4	9.1342	0.7	0.4248	0.6	0.87	2282.4	12.5	2351.5	6.9	2412.1	6.4	2412.1	6.4	94.6
02NA16-3R2	168	139954	2.1	6.3972	0.2	9.5039	1.6	0.4409	1.6	0.99	2354.9	30.9	2387.9	14.5	2416.2	3.5	2416.2	3.5	97.5
02NA16-12C	138	180248	2.1	6.3787	0.3	9.6568	0.9	0.4467	0.8	0.93	2380.8	16.2	2402.6	8.0	2421.1	5.4	2421.1	5.4	98.3
02NA16-4C	676	120122	17.3	6.3682	0.3	9.3122	1.2	0.4301	1.2	0.97	2306.2	22.7	2369.2	11.1	2423.9	5.3	2423.9	5.3	95.1
02NA16-9R	362	62636	2.3	6.3665	0.6	8.4399	3.4	0.3897	3.3	0.98	2121.5	59.6	2279.5	30.4	2424.4	10.5	2424.4	10.5	87.5
02NA16-24C	131	153865	2.3	6.2969	0.4	10.2487	0.9	0.4680	0.9	0.92	2475.0	17.5	2457.5	8.5	2443.0	6.0	2443.0	6.0	101.3
02NA16-13C	170	185311	2.3	6.2888	0.3	9.8792	0.7	0.4506	0.6	0.90	2397.9	12.9	2423.6	6.6	2445.2	5.2	2445.2	5.2	98.1
02NA16-1R	428	36448	1.8	6.2734	0.5	10.1282	1.5	0.4608	1.4	0.94	2443.2	27.9	2446.5	13.4	2449.3	8.2	2449.3	8.2	99.7
02NA16-4R	154	224396	2.6	6.2697	0.4	9.8397	0.9	0.4474	0.8	0.88	2383.8	16.3	2419.9	8.5	2450.3	7.4	2450.3	7.4	97.3
02NA16-9C	241	288476	2.1	6.2252	0.4	10.3084	1.2	0.4654	1.1	0.96	2463.4	23.5	2462.9	11.1	2462.4	6.0	2462.4	6.0	100.0
02NA16-10C	133	239528	2.0	6.2118	0.5	10.4945	1.6	0.4728	1.5	0.95	2495.8	30.6	2479.4	14.4	2466.0	8.0	2466.0	8.0	101.2
02NA16-14C	87	264173	1.8	6.2033	0.4	10.3483	1.2	0.4656	1.2	0.96	2464.1	24.4	2466.4	11.5	2468.3	6.0	2468.3	6.0	99.8
02NA16-20C	242	124990	1.9	6.1834	0.3	10.5932	1.7	0.4751	1.7	0.99	2505.7	35.2	2488.1	15.9	2473.7	4.2	2473.7	4.2	101.3
02NA16-8C	156	159451	1.9	6.1832	0.3	10.3543	1.1	0.4643	1.0	0.97	2458.7	21.3	2467.0	10.0	2473.8	4.7	2473.8	4.7	99.4
02NA16-21C	243	180041	1.7	6.1775	0.2	10.2912	2.6	0.4611	2.6	1.00	2444.3	53.2	2461.3	24.3	2475.4	3.7	2475.4	3.7	98.7
02NA16-22C	156	274257	2.1	6.1749	0.3	10.5730	1.4	0.4735	1.4	0.98	2498.9	28.7	2486.3	13.1	2476.1	4.6	2476.1	4.6	100.9
02NA16-5C	149	71633	1.9	6.1746	0.2	10.3347	1.2	0.4628	1.2	0.98	2452.0	24.1	2465.2	11.1	2476.1	3.6	2476.1	3.6	99.0
02NA16-1C	568	77538	1.4	6.1745	0.1	10.2843	0.5	0.4606	0.5	0.96	2442.0	9.2	2460.7	4.4	2476.2	2.2	2476.2	2.2	98.6
02NA16-15R	241	181713	1.7	6.1744	0.2	10.5053	1.1	0.4704	1.1	0.99	2485.5	22.1	2480.4	10.1	2476.2	3.1	2476.2	3.1	100.4
02NA16-6C	145	291744	1.9	6.1720	0.4	10.4546	3.1	0.4680	3.0	0.99	2474.7	62.1	2475.9	28.3	2476.8	7.4	2476.8	7.4	99.9
02NA16-16C	138	265451	2.2	6.1713	0.4	10.3926	1.7	0.4652	1.6	0.97	2462.3	33.2	2470.4	15.4	2477.0	6.7	2477.0	6.7	99.4
02NA16-11C	192	521468	1.5	6.1608	0.2	10.5702	1.0	0.4723	1.0	0.99	2493.7	20.4	2486.1	9.2	2479.9	2.6	2479.9	2.6	100.6
02NA16-23C	108	179084	2.7	6.1581	0.4	10.7005	1.6	0.4779	1.5	0.96	2518.2	31.6	2497.5	14.6	2480.7	7.1	2480.7	7.1	101.5
02NA16-2C	158	162284	2.0	6.1567	0.2	10.5219	1.9	0.4698	1.9	0.99	2482.8	39.0	2481.9	17.7	2481.0	4.1	2481.0	4.1	100.1
02NA16-7C	84	147163	2.3	6.1563	0.3	10.4301	0.8	0.4657	0.8	0.92	2464.7	15.9	2473.7	7.8	2481.2	5.4	2481.2	5.4	99.3
02NA16-18C	160	391938	2.1	6.1393	0.2	10.5065	1.1	0.4678	1.1	0.99	2474.0	22.6	2480.5	10.3	2485.8	2.8	2485.8	2.8	99.5

03NA16				Isotope ratios							Apparent ages (Ma)								
Analysis	U (ppm)	206Pb 204Pb	U/Th	206Pb* 207Pb*	± (%)	207Pb* 235U*	± (%)	206Pb* 238U	± (%)	error corr.	206Pb* 238U*	± (Ma)	207Pb* 235U	± (Ma)	206Pb* 207Pb*	± (Ma)	Best age (Ma)	± (Ma)	Conc (%)
03NA16-2C	728	9620	18.5	9.0686	0.6	3.9878	4.2	0.2623	4.2	0.99	1501.5	56.2	1631.7	34.5	1803.8	11.7	1803.8	11.7	83.2
03NA16-4C	383	9576	2.2	7.0069	2.3	7.9931	5.1	0.4062	4.5	0.89	2197.5	83.4	2230.2	45.7	2260.4	40.4	2260.4	40.4	97.2
03NA16-20C	283	12106	3.0	6.4838	0.7	8.6723	1.2	0.4078	1.0	0.83	2204.9	17.9	2304.2	10.6	2393.4	11.2	2393.4	11.2	92.1
03NA16-19C	89	292049	2.0	6.4689	1.7	9.2681	4.6	0.4348	4.3	0.93	2327.4	83.1	2364.9	42.2	2397.3	29.7	2397.3	29.7	97.1
03NA16-3C	141	6986	1.7	6.4160	0.8	8.3880	4.4	0.3903	4.3	0.98	2124.3	78.1	2273.9	39.9	2411.2	14.4	2411.2	14.4	88.1
03NA16-5C	601	24720	12.4	6.3968	0.3	8.3100	1.7	0.3855	1.7	0.99	2102.1	29.9	2265.4	15.3	2416.3	4.6	2416.3	4.6	87.0
03NA16-23C	197	30694	1.6	6.3396	0.6	9.4018	1.5	0.4323	1.3	0.90	2316.0	25.8	2378.0	13.5	2431.6	11.0	2431.6	11.0	95.2
03NA16-11C	119	12749	2.7	6.3149	0.6	10.2241	1.4	0.4683	1.2	0.90	2475.9	25.0	2455.3	12.5	2438.2	10.0	2438.2	10.0	101.5
03NA16-21C	543	320452	31.0	6.2691	0.3	10.0717	0.9	0.4579	0.8	0.94	2430.5	17.0	2441.4	8.2	2450.5	4.9	2450.5	4.9	99.2
03NA16-24C	409	11847	2.0	6.2662	0.7	8.3205	4.1	0.3781	4.0	0.99	2067.6	70.8	2266.6	36.8	2451.3	11.1	2451.3	11.1	84.3
03NA16-8C	79	12096	2.7	6.2633	0.8	9.2199	5.3	0.4188	5.2	0.99	2255.1	99.9	2360.1	48.7	2452.1	13.3	2452.1	13.3	92.0
03NA16-10C	206	183245	1.8	6.2402	0.4	10.1991	1.1	0.4616	1.1	0.94	2446.6	21.8	2453.0	10.5	2458.3	6.4	2458.3	6.4	99.5
03NA16-9C	240	41580	2.1	6.2290	0.3	9.7570	0.9	0.4408	0.9	0.94	2354.2	17.1	2412.1	8.5	2461.3	5.3	2461.3	5.3	95.6
03NA16-12R	298	6120	1.9	6.1975	0.4	10.1813	3.6	0.4576	3.5	0.99	2429.1	71.6	2451.4	32.9	2469.9	7.3	2469.9	7.3	98.3
03NA16-1R	119	184102	2.6	6.1750	0.3	10.7390	1.5	0.4809	1.4	0.98	2531.4	29.8	2500.8	13.5	2476.0	5.1	2476.0	5.1	102.2
03NA16-22C	224	170381	2.0	6.1730	0.3	10.4993	1.3	0.4701	1.2	0.98	2483.8	25.3	2479.9	11.6	2476.6	4.4	2476.6	4.4	100.3
03NA16-1C	421	20981	1.5	6.1649	0.3	10.2023	1.9	0.4562	1.8	0.98	2422.6	37.2	2453.3	17.3	2478.8	5.5	2478.8	5.5	97.7
03NA16-5R	288	88344	2.0	6.1600	0.2	10.5220	1.2	0.4701	1.2	0.99	2483.9	25.2	2481.9	11.5	2480.2	3.4	2480.2	3.4	100.2
03NA16-7C	277	63400	1.4	6.1503	0.2	10.3020	1.3	0.4595	1.3	0.99	2437.5	25.5	2462.3	11.7	2482.8	2.6	2482.8	2.6	98.2
03NA16-3R	438	32712	2.1	6.1470	0.4	10.3724	2.1	0.4624	2.1	0.99	2450.2	43.0	2468.6	19.8	2483.7	6.1	2483.7	6.1	98.7
03NA16-18C	519	22051	1.5	6.1463	0.3	10.4865	3.2	0.4675	3.1	1.00	2472.4	64.5	2478.7	29.3	2483.9	5.2	2483.9	5.2	99.5
03NA16-16C	461	365371	1.4	6.1406	0.1	10.5171	0.7	0.4684	0.7	0.98	2476.5	13.7	2481.4	6.3	2485.4	2.2	2485.4	2.2	99.6
03NA16-14C	220	12933	1.6	6.1365	0.4	10.6941	1.5	0.4760	1.4	0.96	2509.6	29.2	2496.9	13.5	2486.6	6.6	2486.6	6.6	100.9
03NA16-4R	124	6669	2.2	6.1349	0.7	10.4781	1.8	0.4662	1.7	0.93	2467.0	34.9	2478.0	17.0	2487.0	11.3	2487.0	11.3	99.2
03NA16-13C	202	548026	1.7	6.1329	0.2	10.5537	1.7	0.4694	1.7	1.00	2481.1	35.8	2484.6	16.2	2487.6	2.9	2487.6	2.9	99.7
03NA16-6C	154	50752	1.5	6.1207	0.2	10.4815	1.2	0.4653	1.2	0.98	2462.9	24.1	2478.3	11.1	2490.9	3.8	2490.9	3.8	98.9

04NA16				Isotope ratios							Apparent ages (Ma)							
Analysis	U (ppm)	206Pb 204Pb	U/Th	206Pb* 207Pb*	± (%)	207Pb* 235U*	± (%)	206Pb* 238U	± (%)	error corr.	206Pb* 238U*	± (Ma)	207Pb* 235U	± (Ma)	206Pb* 207Pb*	± (Ma)	Best age (Ma)	± (Ma)	Conc (%)
04NA16-3R	259	598577	1.3	6.2087	0.2	10.5036	1.1	0.4730	1.0	0.97	2496.6	21.3	2480.2	9.8	2466.8	4.1	2466.8	4.1	101.2
04NA16-11R2	2283	197235	10.9	6.1337	0.2	10.5934	0.9	0.4713	0.8	0.97	2489.1	17.4	2488.1	8.1	2487.3	3.7	2487.3	3.7	100.1
04NA16-7C	886	352725	12.5	6.1101	0.2	10.6649	0.8	0.4726	0.7	0.97	2495.0	15.4	2494.4	7.1	2493.8	3.0	2493.8	3.0	100.0
04NA16-11R	1139	28427	8.5	6.1023	0.3	10.7944	1.4	0.4777	1.3	0.98	2517.4	27.7	2505.6	12.6	2496.0	4.3	2496.0	4.3	100.9
04NA16-12C	790	373127	8.4	6.0935	0.1	10.7972	0.7	0.4772	0.7	0.99	2515.0	15.0	2505.8	6.8	2498.4	2.1	2498.4	2.1	100.7
04NA16-17R	1148	457167	16.5	6.0622	0.1	10.8278	0.9	0.4761	0.9	1.00	2510.1	19.6	2508.5	8.8	2507.1	1.5	2507.1	1.5	100.1
04NA16-6R	489	406009	5.4	5.8575	0.3	11.2836	1.0	0.4794	1.0	0.95	2524.5	20.1	2546.8	9.4	2564.7	5.1	2564.7	5.1	98.4
04NA16-15C	599	249291	14.2	5.8380	1.4	11.2786	1.7	0.4775	0.9	0.55	2516.6	19.6	2546.4	16.0	2570.3	24.0	2570.3	24.0	97.9
04NA16-15R	91	22076	1.2	5.8239	0.3	10.9601	0.6	0.4629	0.6	0.86	2452.5	11.3	2519.7	6.0	2574.3	5.5	2574.3	5.5	95.3
04NA16-12R	340	422498	4.5	5.6758	1.5	12.2908	2.0	0.5059	1.3	0.65	2639.3	27.6	2626.9	18.5	2617.3	25.0	2617.3	25.0	100.8
04NA16-9R	498	270736	18.0	5.6431	0.2	12.2433	1.0	0.5011	1.0	0.98	2618.5	21.5	2623.2	9.6	2626.9	3.8	2626.9	3.8	99.7
04NA16-5R	193	375471	2.4	5.5614	0.8	13.0683	1.0	0.5271	0.6	0.61	2729.3	13.6	2684.6	9.5	2651.1	13.2	2651.1	13.2	102.9
04NA16-20C	93	180650	2.1	5.5587	0.3	12.1202	1.5	0.4886	1.4	0.98	2564.8	30.2	2613.8	13.6	2651.9	4.8	2651.9	4.8	96.7
04NA16-19C	286	72324	1.2	5.5251	0.2	12.6108	1.3	0.5053	1.3	0.98	2636.7	28.5	2651.0	12.6	2662.0	4.1	2662.0	4.1	99.0
04NA16-1C	537	562302	21.3	5.5207	0.3	12.5780	0.9	0.5036	0.8	0.95	2629.3	18.3	2648.6	8.4	2663.3	4.6	2663.3	4.6	98.7
04NA16-19R	76	157356	1.3	5.5085	0.9	12.6401	1.5	0.5050	1.3	0.83	2635.2	27.6	2653.2	14.4	2667.0	14.2	2667.0	14.2	98.8
04NA16-4C	631	306449	26.8	5.5026	0.3	12.8726	1.0	0.5137	1.0	0.97	2672.5	21.1	2670.4	9.4	2668.7	4.3	2668.7	4.3	100.1
04NA16-13C	25	58174	1.2	5.4758	0.9	12.6929	2.1	0.5041	1.9	0.91	2631.3	42.0	2657.1	20.2	2676.8	15.0	2676.8	15.0	98.3
04NA16-14R	44	121958	1.3	5.4466	2.2	13.4645	3.3	0.5319	2.5	0.76	2749.4	56.0	2712.8	31.3	2685.6	35.9	2685.6	35.9	102.4
04NA16-9C	55	131674	1.2	5.3818	0.5	13.1181	3.8	0.5120	3.8	0.99	2665.3	82.3	2688.2	35.9	2705.4	8.1	2705.4	8.1	98.5
04NA16-13R	441	182433	25.6	5.3721	0.1	13.4609	1.4	0.5245	1.4	0.99	2718.1	30.3	2712.5	13.0	2708.4	2.4	2708.4	2.4	100.4
04NA16-18R	412	498241	6.3	5.3595	0.5	13.7758	1.1	0.5355	1.0	0.88	2764.5	22.0	2734.4	10.5	2712.3	8.7	2712.3	8.7	101.9
04NA16-18C	166	190933	0.9	5.3297	0.2	13.0559	0.9	0.5047	0.9	0.98	2633.8	18.5	2683.7	8.3	2721.5	3.2	2721.5	3.2	96.8
04NA16-8C	180	337892	1.7	5.2999	0.8	13.3375	2.3	0.5127	2.2	0.94	2668.0	47.0	2703.8	21.6	2730.7	12.5	2730.7	12.5	97.7
04NA16-11C	87	69568	1.2	5.2431	0.7	13.8466	1.6	0.5265	1.5	0.90	2726.8	32.6	2739.3	15.4	2748.4	11.6	2748.4	11.6	99.2
04NA16-10C	352	44493	0.8	5.2052	0.3	14.3332	1.1	0.5411	1.1	0.96	2788.1	24.5	2772.0	10.7	2760.3	5.5	2760.3	5.5	101.0
04NA16-17C	65	74395	1.1	5.1883	0.7	14.2346	1.6	0.5356	1.5	0.91	2765.2	32.8	2765.5	15.2	2765.7	10.9	2765.7	10.9	100.0
04NA16-5C	611	49231	0.8	5.1596	0.1	14.7823	2.4	0.5532	2.4	1.00	2838.3	56.1	2801.3	23.3	2774.8	2.2	2774.8	2.2	102.3
04NA16-6C	89	130590	1.3	5.1406	0.5	14.2091	5.0	0.5298	5.0	1.00	2740.5	111.3	2763.8	47.5	2780.8	7.6	2780.8	7.6	98.5
04NA16-3C	632	199331	1.5	5.1395	0.3	14.5227	1.5	0.5413	1.5	0.98	2789.1	34.1	2784.5	14.6	2781.2	4.4	2781.2	4.4	100.3
04NA16-7R	65	27298	1.2	5.1357	0.9	14.2539	1.4	0.5309	1.1	0.77	2745.3	23.9	2766.7	13.2	2782.4	14.6	2782.4	14.6	98.7
04NA16-4R	176	363414	0.8	5.1324	0.2	14.4968	1.9	0.5396	1.9	0.99	2781.9	42.8	2782.8	18.1	2783.4	3.9	2783.4	3.9	99.9
04NA16-16C	156	342421	0.9	5.1197	0.2	14.5540	0.8	0.5404	0.8	0.97	2785.2	17.2	2786.5	7.4	2787.5	2.9	2787.5	2.9	99.9
04NA16-1R	63	244962	1.1	5.1162	1.4	14.7050	1.8	0.5456	1.2	0.66	2807.0	27.1	2796.3	17.2	2788.6	22.4	2788.6	22.4	100.7
04NA16-8R	221	1046803	1.3	5.1137	0.2	14.7857	0.9	0.5484	0.9	0.98	2818.4	20.2	2801.5	8.6	2789.4	3.3	2789.4	3.3	101.0
04NA16-10R	222	20025	1.4	5.1122	0.2	15.1787	0.7	0.5628	0.7	0.97	2878.1	16.2	2826.5	6.9	2789.9	2.9	2789.9	2.9	103.2
04NA16-2C	449	390691	0.8	5.0981	0.2	14.9597	1.0	0.5531	1.0	0.98	2838.2	23.5	2812.7	10.0	2794.4	3.6	2794.4	3.6	101.6
04NA16-2R	255	472912	1.4	5.0972	0.2	15.1376	0.8	0.5596	0.8	0.98	2865.0	17.7	2823.9	7.4	2794.7	2.6	2794.7	2.6	102.5

18NA16				Isotope ratios							Apparent ages (Ma)								
Analysis	U (ppm)	206Pb 204Pb	U/Th	206Pb* 207Pb*	± (%)	207Pb* 235U*	± (%)	206Pb* 238U	± (%)	error corr.	206Pb* 238U*	± (Ma)	207Pb* 235U	± (Ma)	206Pb* 207Pb*	± (Ma)	Best age (Ma)	± (Ma)	Conc (%)
18NA16-15R	277	107833	3.7	10.0284	0.5	3.8603	1.3	0.2808	1.2	0.92	1595.3	16.6	1605.4	10.3	1618.8	9.5	1618.8	9.5	98.5
18NA16-2C	253	13984	2.9	9.3231	0.3	4.5995	1.6	0.3110	1.6	0.98	1745.7	23.7	1749.2	13.2	1753.4	6.0	1753.4	6.0	99.6
18NA16-5C	344	9087	3.7	9.2949	0.6	4.5487	3.0	0.3066	2.9	0.98	1724.2	44.6	1739.9	25.1	1758.9	11.3	1758.9	11.3	98.0
18NA16-10C	128	3822	1.3	9.2830	1.3	4.6640	2.7	0.3140	2.4	0.87	1760.4	36.7	1760.8	22.8	1761.2	24.4	1761.2	24.4	100.0
18NA16-17R	131	19118	1.9	9.2532	0.7	4.7252	2.3	0.3171	2.2	0.95	1775.6	34.7	1771.7	19.7	1767.1	12.9	1767.1	12.9	100.5
18NA16-17C	1466	44297	3.5	9.2035	0.7	4.7464	2.7	0.3168	2.7	0.96	1774.2	41.1	1775.5	23.1	1777.0	13.3	1777.0	13.3	99.8
18NA16-9R	130	53204	1.9	9.1747	0.7	4.7588	4.1	0.3167	4.0	0.99	1773.4	62.3	1777.7	34.2	1782.7	12.5	1782.7	12.5	99.5
18NA16-20C	2354	180410	3.8	9.1604	0.3	4.8067	1.1	0.3193	1.0	0.97	1786.5	16.3	1786.1	9.1	1785.5	4.8	1785.5	4.8	100.1
18NA16-10R	113	143090	1.7	9.1602	0.3	4.7824	1.0	0.3177	0.9	0.96	1778.6	14.7	1781.8	8.3	1785.6	5.2	1785.6	5.2	99.6
18NA16-12C	487	167058	4.3	9.1493	0.2	4.7903	1.5	0.3179	1.5	0.99	1779.3	22.6	1783.2	12.4	1787.7	4.4	1787.7	4.4	99.5
18NA16-4R2	215	92983	1.7	9.1488	0.2	4.7671	3.0	0.3163	3.0	1.00	1771.7	45.7	1779.1	24.9	1787.8	4.4	1787.8	4.4	99.1
18NA16-1C	378	103352	2.6	9.1428	0.2	4.7332	1.0	0.3139	1.0	0.98	1759.7	15.1	1773.1	8.4	1789.0	3.7	1789.0	3.7	98.4
18NA16-1C2	328	64601	2.2	9.1329	0.2	5.0089	1.4	0.3318	1.4	0.98	1847.0	22.0	1820.8	11.8	1791.0	4.5	1791.0	4.5	103.1
18NA16-6R	177	182366	1.7	9.1228	0.3	4.8719	0.9	0.3223	0.9	0.94	1801.2	13.5	1797.4	7.7	1793.0	5.9	1793.0	5.9	100.5
18NA16-4R	138	122414	1.6	9.1155	0.3	4.8669	0.9	0.3218	0.8	0.93	1798.3	12.5	1796.5	7.3	1794.5	5.9	1794.5	5.9	100.2
18NA16-2R	155	310570	1.4	9.1104	0.3	4.8248	1.4	0.3188	1.3	0.98	1783.8	20.9	1789.2	11.5	1795.5	4.9	1795.5	4.9	99.4
18NA16-1R	167	105155	2.3	9.1040	0.4	4.8635	0.8	0.3211	0.7	0.88	1795.2	10.7	1796.0	6.5	1796.8	6.7	1796.8	6.7	99.9
18NA16-18R	128	43643	2.4	9.1025	0.4	5.0683	1.9	0.3346	1.8	0.97	1860.6	29.5	1830.8	15.9	1797.1	8.2	1797.1	8.2	103.5
18NA16-3R	136	157916	1.9	9.1008	0.3	4.8625	0.7	0.3209	0.6	0.88	1794.4	10.1	1795.8	6.2	1797.4	6.3	1797.4	6.3	99.8
18NA16-19R	93	447939	1.7	9.0961	0.7	4.7975	4.5	0.3165	4.5	0.99	1772.6	69.6	1784.5	38.2	1798.4	12.7	1798.4	12.7	98.6
18NA16-9C	675	305583	7.9	9.0863	0.1	4.8753	0.7	0.3213	0.7	0.98	1796.0	10.4	1798.0	5.7	1800.3	2.4	1800.3	2.4	99.8
18NA16-4C	835	249629	2.3	9.0801	0.2	4.8328	0.6	0.3183	0.6	0.97	1781.2	9.7	1790.6	5.4	1801.6	2.8	1801.6	2.8	98.9
18NA16-7C	693	38751	1.6	9.0785	0.3	4.7956	1.3	0.3158	1.3	0.98	1769.0	19.5	1784.1	10.8	1801.9	4.7	1801.9	4.7	98.2
18NA16-13R	108	77818	2.5	9.0767	0.5	4.9584	0.8	0.3264	0.6	0.78	1821.0	10.1	1812.3	6.9	1802.2	9.2	1802.2	9.2	101.0
18NA16-5R	124	159027	2.3	9.0753	0.5	4.8960	1.8	0.3223	1.8	0.96	1800.7	27.9	1801.6	15.6	1802.5	9.5	1802.5	9.5	99.9
18NA16-19C	401	27254	9.5	9.0731	0.3	4.8498	1.0	0.3191	0.9	0.96	1785.5	14.5	1793.6	8.2	1803.0	5.0	1803.0	5.0	99.0
18NA16-6C	874	56228	1.6	9.0710	0.3	4.8619	1.6	0.3199	1.6	0.99	1789.1	24.8	1795.7	13.6	1803.4	4.8	1803.4	4.8	99.2
18NA16-11R	132	151890	1.6	9.0696	0.5	4.8475	3.6	0.3189	3.5	0.99	1784.2	55.1	1793.2	30.1	1803.7	9.8	1803.7	9.8	98.9
18NA16-8C	496	191357	3.3	9.0677	0.2	4.9485	4.0	0.3254	3.9	1.00	1816.2	62.5	1810.6	33.4	1804.0	3.1	1804.0	3.1	100.7
18NA16-8R	141	212211	1.8	9.0656	0.4	4.8881	0.7	0.3214	0.6	0.82	1796.5	9.5	1800.2	6.2	1804.4	7.7	1804.4	7.7	99.6
18NA16-20R	384	361943	4.0	9.0625	0.2	5.1999	2.7	0.3418	2.7	1.00	1895.2	44.7	1852.6	23.3	1805.1	3.6	1805.1	3.6	105.0
18NA16-4C2	1676	142623	5.5	9.0607	0.1	4.8283	1.2	0.3173	1.2	1.00	1776.5	18.4	1789.8	10.0	1805.4	1.8	1805.4	1.8	98.4
18NA16-14R	127	150457	1.7	9.0498	0.7	4.8615	0.9	0.3191	0.7	0.71	1785.2	10.3	1795.6	7.9	1807.6	12.0	1807.6	12.0	98.8
18NA16-14C	916	325991	4.7	9.0496	0.2	4.9184	0.9	0.3228	0.9	0.99	1803.5	14.7	1805.4	8.0	1807.7	3.0	1807.7	3.0	99.8
18NA16-12R	144	162810	1.6	9.0400	0.2	4.9571	0.9	0.3250	0.9	0.97	1814.2	14.1	1812.0	7.8	1809.6	4.3	1809.6	4.3	100.3
18NA16-13C	1215	18937	7.9	9.0202	0.5	4.9871	1.1	0.3263	1.0	0.87	1820.2	15.5	1817.1	9.4	1813.6	9.9	1813.6	9.9	100.4
18NA16-11C	5	3716	2.5	8.8948	6.4	4.5759	8.5	0.2952	5.6	0.66	1667.5	81.8	1744.9	70.9	1839.0	116.2	1839.0	116.2	90.7
18NA16-15C	211	26885	2.5	7.0155	3.0	6.8326	3.3	0.3477	1.3	0.40	1923.4	22.0	2090.0	29.4	2258.3	52.5	2258.3	52.5	85.2

25NA16				Isotope ratios								Apparent ages (Ma)							
Analysis	U (ppm)	206Pb 204Pb	U/Th	206Pb* 207Pb*	± (%)	207Pb* 235U*	± (%)	206Pb* 238U	± (%)	error corr.	206Pb* 238U*	± (Ma)	207Pb* 235U	± (Ma)	206Pb* 207Pb*	± (Ma)	Best age (Ma)	± (Ma)	Conc (%)
25NA16-15C	158	173076	2.2	9.3374	0.4	4.7613	1.2	0.3224	1.2	0.95	1801.6	18.5	1778.1	10.4	1750.6	6.7	1750.6	6.7	102.9
25NA16-5R	180	292538	2.6	9.3317	0.2	4.7540	3.1	0.3218	3.1	1.00	1798.3	49.1	1776.8	26.3	1751.7	4.2	1751.7	4.2	102.7
25NA16-41R	194	149428	2.7	9.3314	0.3	4.7214	0.7	0.3195	0.7	0.93	1787.4	10.2	1771.0	5.9	1751.7	4.6	1751.7	4.6	102.0
25NA16-36R	134	21707	3.3	9.2987	0.6	4.7462	2.1	0.3201	2.1	0.97	1790.2	32.2	1775.4	17.9	1758.2	10.1	1758.2	10.1	101.8
25NA16-78C	615	77591	21.3	9.2896	0.2	4.6461	1.3	0.3130	1.3	0.99	1755.6	19.7	1757.6	10.8	1759.9	2.9	1759.9	2.9	99.8
25NA16-36C	676	416134	7.1	9.2817	0.1	4.7473	0.8	0.3196	0.8	0.99	1787.6	12.3	1775.6	6.7	1761.5	2.0	1761.5	2.0	101.5
25NA16-2R	146	10650	2.1	9.1697	2.4	4.8025	2.6	0.3194	1.1	0.43	1786.7	17.8	1785.3	22.3	1783.7	43.6	1783.7	43.6	100.2
25NA16-3C	420	851540	6.4	8.9040	0.1	4.9890	0.7	0.3222	0.7	0.98	1800.4	10.2	1817.5	5.6	1837.1	2.5	1837.1	2.5	98.0
25NA16-55C	276	71650	4.1	8.3544	0.5	5.5505	1.5	0.3363	1.5	0.95	1868.9	23.7	1908.4	13.3	1951.7	8.9	1951.7	8.9	95.8
25NA16-77C	303	6757	5.4	7.7910	4.5	6.0868	5.5	0.3439	3.2	0.58	1905.6	52.5	1988.4	47.9	2075.5	78.8	2075.5	78.8	91.8
25NA16-21C	560	263693	8.7	7.7736	0.9	6.7876	2.1	0.3827	1.9	0.90	2088.8	34.1	2084.1	18.7	2079.5	16.0	2079.5	16.0	100.4
25NA16-86C	719	15326	2.4	7.5991	0.5	6.2191	7.9	0.3428	7.9	1.00	1899.9	130.4	2007.1	69.5	2119.3	7.9	2119.3	7.9	89.6
25NA16-8R	307	265980	3.1	7.5577	1.7	6.7373	4.0	0.3693	3.6	0.90	2026.1	62.3	2077.5	35.0	2128.9	29.5	2128.9	29.5	95.2
25NA16-20C	93	106178	2.5	7.0526	0.7	7.7829	3.6	0.3981	3.6	0.98	2160.3	65.4	2206.2	32.7	2249.2	12.6	2249.2	12.6	96.0
25NA16-53C	246	532074	3.4	7.0124	0.2	8.0972	1.4	0.4118	1.4	0.99	2223.2	26.2	2241.9	12.8	2259.1	4.2	2259.1	4.2	98.4
25NA16-19C	366	636975	2.1	6.8926	0.8	8.3763	1.4	0.4187	1.1	0.80	2254.7	20.8	2272.6	12.4	2288.7	14.0	2288.7	14.0	98.5
25NA16-23C	116	131209	2.0	6.8279	1.7	8.1082	2.5	0.4015	1.7	0.71	2176.1	32.2	2243.2	22.3	2305.0	29.8	2305.0	29.8	94.4
25NA16-25C	106	108667	1.6	6.7321	0.5	8.4391	2.3	0.4120	2.2	0.97	2224.3	41.4	2279.4	20.5	2329.2	8.7	2329.2	8.7	95.5
25NA16-54C	377	68155	2.1	6.7233	0.2	8.4823	1.4	0.4136	1.4	0.99	2231.4	26.5	2284.0	12.9	2331.4	2.8	2331.4	2.8	95.7
25NA16-68C	124	206828	3.8	6.7140	0.9	8.8882	1.5	0.4328	1.2	0.82	2318.4	23.9	2326.6	13.7	2333.8	14.7	2333.8	14.7	99.3
25NA16-45C	244	105597	3.3	6.6982	0.5	8.6068	1.0	0.4181	0.9	0.86	2251.9	16.6	2297.3	9.2	2337.8	8.7	2337.8	8.7	96.3
25NA16-72C	156	197387	2.2	6.6969	0.7	8.8919	2.6	0.4319	2.5	0.97	2314.2	48.6	2327.0	23.6	2338.2	11.2	2338.2	11.2	99.0
25NA16-45R	315	149353	2.8	6.6674	0.2	9.0616	1.3	0.4382	1.3	0.98	2342.5	25.8	2344.2	12.2	2345.7	4.1	2345.7	4.1	99.9
25NA16-4C	496	69135	7.0	6.6319	0.3	8.8824	0.9	0.4272	0.9	0.94	2293.2	16.7	2326.0	8.4	2354.9	5.4	2354.9	5.4	97.4
25NA16-82C	119	151994	1.6	6.6231	1.5	9.3868	3.0	0.4509	2.6	0.87	2399.2	51.5	2376.5	27.1	2357.1	24.9	2357.1	24.9	101.8
25NA16-67C	573	14828	2.2	6.6173	0.6	7.9332	8.2	0.3807	8.2	1.00	2079.7	145.9	2223.5	74.3	2358.6	10.1	2358.6	10.1	88.2
25NA16-50C	107	9386	2.1	6.6035	2.0	9.1112	2.6	0.4364	1.6	0.62	2334.3	31.3	2349.2	23.5	2362.2	34.4	2362.2	34.4	98.8
25NA16-83C	111	174976	2.3	6.6007	0.4	9.0253	1.7	0.4321	1.7	0.98	2315.0	33.0	2340.6	15.9	2362.9	6.6	2362.9	6.6	98.0
25NA16-79C	197	657879	2.8	6.5901	0.6	9.1508	1.8	0.4374	1.7	0.93	2338.9	32.9	2353.2	16.4	2365.7	10.9	2365.7	10.9	98.9
25NA16-80C	207	1269624	2.9	6.5780	0.3	9.3166	2.1	0.4445	2.0	0.99	2370.6	40.3	2369.7	18.9	2368.8	5.9	2368.8	5.9	100.1
25NA16-84C	112	147910	1.9	6.5582	2.3	9.7362	2.6	0.4631	1.3	0.51	2453.2	27.0	2410.1	24.1	2373.9	38.4	2373.9	38.4	103.3
25NA16-3R	93	121451	2.1	6.5483	0.9	9.2863	1.8	0.4410	1.5	0.87	2355.3	30.0	2366.7	16.0	2376.5	14.7	2376.5	14.7	99.1
25NA16-35R	175	10619	2.8	6.5452	0.4	8.5953	5.8	0.4080	5.8	1.00	2205.9	108.4	2296.1	53.0	2377.3	7.4	2377.3	7.4	92.8
25NA16-73C	461	75700	7.9	6.5191	0.3	9.3580	1.8	0.4425	1.7	0.99	2361.6	34.2	2373.7	16.1	2384.1	4.7	2384.1	4.7	99.1
25NA16-17C	128	250764	2.1	6.5120	0.5	9.2544	1.1	0.4371	1.0	0.89	2337.6	19.2	2363.5	10.1	2386.0	8.3	2386.0	8.3	98.0
25NA16-27C	113	161202	1.8	6.5053	0.2	9.3428	1.1	0.4408	1.1	0.98	2354.2	21.7	2372.2	10.3	2387.7	3.6	2387.7	3.6	98.6
25NA16-61C	116	128564	1.7	6.5023	0.4	9.3035	0.9	0.4387	0.8	0.91	2345.0	16.5	2368.4	8.5	2388.5	6.5	2388.5	6.5	98.2
25NA16-28C	136	116788	1.6	6.4907	1.4	9.0542	1.7	0.4262	1.0	0.59	2288.7	19.7	2343.5	15.9	2391.5	24.0	2391.5	24.0	95.7
25NA16-26C	96	139023	2.2	6.4793	0.4	9.4607	1.0	0.4446	0.9	0.90	2371.1	17.6	2383.7	9.0	2394.5	7.2	2394.5	7.2	99.0
25NA16-35C	433	60755	2.6	6.4754	0.2	10.1511	3.3	0.4767	3.3	1.00	2513.0	68.0	2448.6	30.3	2395.6	3.4	2395.6	3.4	104.9
25NA16-7C	442	381313	1.1	6.4638	0.3	9.3941	1.8	0.4404	1.8	0.99	2352.4	35.5	2377.3	16.7	2398.6	4.3	2398.6	4.3	98.1
25NA16-37C	233	478908	3.1	6.4619	0.2	9.4059	1.1	0.4408	1.1	0.98	2354.3	21.8	2378.4	10.3	2399.1	3.5	2399.1	3.5	98.1
25NA16-66C	431	50338	4.7	6.4510	0.5	9.7777	1.9	0.4575	1.8	0.96	2428.4	36.4	2414.0	17.3	2402.0	9.0	2402.0	9.0	101.1
25NA16-16C	217	388446	3.4	6.4414	0.1	9.5861	0.7	0.4478	0.7	0.98	2385.6	13.4	2395.8	6.3	2404.5	2.3	2404.5	2.3	99.2
25NA16-44C	65	115868	2.2	6.4302	0.4	9.6595	1.9	0.4505	1.9	0.98	2397.4	38.0	2402.9	17.9	2407.5	7.3	2407.5	7.3	99.6
25NA16-48C	175	40404	1.5	6.4296	0.5	9.3706	1.5	0.4370	1.4	0.94	2337.0	26.9	2375.0	13.3	2407.6	8.2	2407.6	8.2	97.1
25NA16-32C	137	180131	2.1	6.4008	0.4	9.8419	1.8	0.4569	1.8	0.98	2425.8	36.4	2420.1	17.0	2415.2	6.2	2415.2	6.2	100.4
25NA16-13C	447	102509	1.6	6.3896	0.7	9.6826	5.7	0.4487	5.6	0.99	2389.5	112.1	2405.1	52.2	2418.2	12.5	2418.2	12.5	98.8
25NA16-33C	156	83279	2.7	6.3891	0.3	9.7362	0.9	0.4512	0.8	0.93	2400.4	16.9	2410.1	8.4	2418.4	5.6	2418.4	5.6	99.3
25NA16-4R	245	22025	2.5	6.3878	0.6	9.5599	1.4	0.4429	1.3	0.92	2363.6	25.2	2393.3	12.8	2418.7	9.4	2418.7	9.4	97.7
25NA16-71C	561	152977	1.3	6.3615	0.2	9.9403	1.6	0.4586	1.6	1.00	2433.5	31.7	2429.3	14.5	2425.7	2.6	2425.7	2.6	100.3
25NA16-34C	700	177258	1.5	6.3573	0.1	10.3308	3.3	0.4763	3.3	1.00	2511.2	69.2	2464.9	30.8	2426.8	1.4	2426.8	1.4	103.5
25NA16-24C	358	556928	3.1	6.3566	0.2	9.8925	1.3	0.4561	1.3	0.99	2422.2	26.4	2424.8	12.2	2427.0	3.6	2427.0	3.6	99.8
25NA16-11C	230	419035	2.5	6.3392	0.3	9.9671	1.2	0.4582	1.1	0.97	2431.8	22.6	2431.7	10.6	2431.7	4.8	2431.7	4.8	100.0
25NA16-40C	269	121292	4.0	6.3391	0.2	9.8754	1.3	0.4540	1.3	0.99	2413.1	26.8	2423.2	12.4	2431.7	3.8	2431.7	3.8	99.2
25NA16-18C	294	45687	1.4	6.3336	0.4	9.7915	1.2	0.4498	1.2	0.95	2394.3	23.5	2415.4	11.3	2433.1	6.2	2433.1	6.2	98.4
25NA16-69C	88	20662	2.0	6.3324	1.0	10.1159	1.4	0.4646	1.0	0.72	2459.8	20.7	2445.4	12.9	2433.5	16.4	2433.5	16.4	101.1
25NA16-30C	313	202062	3.0	6.3229	0.5	10.1262	1.1	0.4644	0.9	0.87	2458.8	18.9	2446.4	9.8	2436.0	8.7	2436.0	8.7	100.9
25NA16-52C	199	1089198	2.9	6.3229	0.3	9.9855	1.0	0.4579	1.0	0.97	2430.3	20.4	2433.4	9.6	2436.0	4.3	2436.0	4.3	99.8
25NA16-1C	243	46818	5.0	6.3187	0.3	9.3267	1.5	0.4274	1.4	0.98	2294.1	27.6	2370.6	13.4	2437.1	5.5	2437.1	5.5	94.1
25NA16-49C	165	309488	1.5	6.3130	0.2	9.9980	1.2	0.4578	1.2	0.99	2429.7	23.7	2434.6	10.9	2438.7	3.0	2438.7	3.0	99.6
25NA16-74C	100	130258	2.0	6.3130	0.5	10.0783	1.2	0.4614	1.1	0.92	2445.9	22.7	2442.0	11.2	2438.7	7.9	2438.7	7.9	100.3
25NA16-57C	94	296973	1.7	6.2913	0.6	10.1056	1.8	0.4611	1.7	0.95	2444.4	35.2	2444.5	16.8	2444.5	9.4	2444.5	9.4	100.0
25NA16-6R	199	185372	3.0	6.2906	0.2	10.1388	1.3	0.4626	1.3	0.99	2450.9	25.8	2447.5	11.9	2444.7	3.7	2444.7	3.7	100.3
25NA16-70C	283	252251	1.5	6.2902	0.4	10.2401	1.5	0.4672	1.4	0.95	2471.1	28.6	2456.7	13.5	2444.8	7.4	2444.8	7.4	101.1
25NA16-12C	125	206164	1.8	6.2842	0.2	10.1336	1.0	0.4619	0.9	0.98	2447.8	19.0	2447.0	8.8	2446.4	3.2	2446.4	3.2	100.1
25NA16-9C	199	322655	1.3	6.2808	0.3	10.1541	0.7	0.4625	0.7	0.90	2450.8	13.5	2448.9	6.8	2447.3	5.5	2447.3	5.5	100.1
25NA16-64C	78	133920	2.2	6.2676	0.7	10.0779	1.8	0.4581	1.7	0.91	2431.2	33.6	2441.9	16.8	2450.9	12.6	2450.9	12.6	99.2
25NA16-76C	348	54757	6.2	6.2657	0.5	10.0454	1.1	0.4565	0.9	0.89	2424.1	19.2	2439.0	9.9	2451.4	8.4	2451.4	8.4	98.9
25NA16-85C	283	317420	2.0	6.2481	0.2	10.1470	0.8	0.4598	0.8	0.97	2438.7	15.3	2448.3	7.2	2456.2	3.0	2456.2	3.0	99.3
25NA16-38C	193	320784	1.4	6.2467	0.2	10.1693	1.0	0.4607	1.0	0.97	2442.7	20.6	2450.3	9.6	2456.5	4.2	2456.5	4.2	99.4
25NA16-9R	178	377306	2.9	6.2380	0.2	10.4286	3.2	0.4718	3.2	1.00	2491.5	66.3	2473.6	29.8	2458.9	3.0	2458.9	3.0	101.3
25NA16-42C	116	235424	2.1	6.2376	0.3	10.3977	2.9	0.4704	2.9	0.99	2485.3	59.4	2470.8	26.9	2459.0	5.6	2459.0	5.6	101.1
25NA16-22C	88	82323	2.0	6.2301	0.5	10.3313	1.1	0.4668	1.0	0.90	2469.6	19.5	2464.9	9.8	2461.0	7.9	2461.0	7.9	100.3
25NA16-39C	102	195720	1.9	6.2227	0.4	10.6416	0.8	0.4803	0.7	0.89	2528.4	15.5	2492.3	7.7	2463.0	6.4	2463.0	6.4	102.7
25NA16-58C	351	60626	2.0	6.2139	0.3	10.2657	1.2	0.4626	1.2	0.98	2451.2	24.7	2459.0	11.5	2465.5	4.6	2465.5	4.6	99.4
25NA16-6C	598	193173	1.3	6.2085	0.1	10.6595	1.6	0.4800	1.5	1.00	2527.2	32.3	2493.9	14.4	2466.9	2.2	2466.9	2.2	102.4
25NA16-8C	114	11544	2.2	6.2018	0.9	10.4075	1.8	0.4681	1.6	0.87	2475.3	32.2	2471.7	16.7	2468.7	15.0	2468.7	15.0	100.3
25NA16-31C	98	221779	2.0	6.2005	0.4	10.5781	1.1	0.4757	1.1	0.93	2508.5	22.1	2486.8	10.6	2469.1	6.8	2469.1	6.8	101.6
25NA16-75C	530	473955	1.4	6.1956	0.1	10.5243	0.7	0.4729	0.7	0.99	2496.3	15.2	2482.1	6.9	2470.4	2.1	2470.4	2.1	101.0
25NA16-14C	53	109633	2.1	6.1900	1.0	10.3957	1.7	0.4667	1.4	0.81	2469.1	28.6	2470.7	15.9	2471.9	16.9	2471.9	16.9	99.9
25NA16-2C	157	315225	1.3	6.1850	0.3	10.5180	0.6	0.4718	0.5	0.89	2491.5	10.3	2481.5	5.2	2473.3	4.3	2473.3	4.3	100.7
25NA16-81C	73	185055	2.5	6.1844	0.4	10.4666	1.0	0.4695	0.9	0.90	2481.2	19.1	2477.0	9.5	2473.5	7.5	2473.5	7.5	100.3
25NA16-10C	191	756048	1.9	6.1748	0.2	10.7802	1.0	0.4828	1.0	0.97	2539.4	21.2	2504.4	9.7	2476.1	4.1	2476.1	4.1	102.6
25NA16-29C	85	13356	2.4	6.1728	0.8	10.4969	1.5	0.4699	1.3	0.86	2483.3	26.9	2479.6	14.0	2476.6	12.8	2476.6	12.8	100.3
25NA16-65C	117	79387	1.8	6.1388	0.5	10.8472	1.1	0.4829	1.0	0.90	2540.1	21.0	2510.1	10.4	2486.0	8.3	2486.0	8.3	102.2
25NA16-59C	89	190087	2.1	6.1276	0.4	10.5787	1.8	0.4701	1.8	0.98	2484.1	36.9	2486.8	17.0	2489.0	6.5	2489.0	6.5	99.8
25NA16-62C	88	173499	1.7	6.1265	0.4	10.6595	2.5	0.4736	2.4	0.99	2499.5	50.6	2493.9	23.0	2489.3	6.7	2489.3	6.7	100.4
25NA16-87C	86	20766	1.8	6.1175	0.7	10.7133	3.2	0.4753	3.1	0.98	2506.9	65.3	2498.6	29.9	2491.8	11.5	2491.8	11.5	100.6

Appendix C: Lu-Hf Analysis.

Appendix C includes Lu-Hf zircon analysis of samples 03NA16 and 04NA16 of the quartzofeldspathic gneiss from the Maiden Peak area. Sample 02NA16 was not selected for Hf analysis because of the similarity in its U-Pb signature and its geographic proximity to sample 03NA16. Samples 18NA16 and 25NA16 were collected from the Bloody Dick gneiss in the Beaverhead Range.

03NA16

Analysis	(^{176}Yb + ^{176}Lu) / ^{176}Hf (%)	Volts Hf	^{176}Hf/^{177}Hf	± (1σ)	^{176}Lu/^{177}Hf	^{176}Hf/^{177}Hf (T)	E-Hf (0)	E-Hf (0) ± (1σ)	E-Hf (T)	Age (Ma)
03NA16-22C	13.8	4.0	0.281241	0.000015	0.000805	0.281203	-54.6	0.5	0.3	2477
03NA16-1C	34.6	3.2	0.281264	0.000021	0.001790	0.281179	-53.8	0.8	-0.5	2479
03NA16-7C	22.4	3.6	0.281298	0.000018	0.001366	0.281234	-52.6	0.6	1.5	2483
03NA16-18C	36.4	3.3	0.281329	0.000021	0.002036	0.281233	-51.5	0.7	1.5	2484
03NA16-21C	6.4	3.6	0.281192	0.000017	0.000491	0.281169	-56.3	0.6	-1.5	2451
03NA16-13C	19.0	3.9	0.281291	0.000024	0.001073	0.281240	-52.8	0.8	1.9	2488
03NA16-6C	39.9	3.0	0.281332	0.000029	0.002409	0.281217	-51.4	1.0	1.1	2491
03NA16-2C	7.4	4.2	0.281419	0.000017	0.000517	0.281401	-48.3	0.6	-8.3	1804
03NA16-19C	14.0	3.7	0.281200	0.000018	0.000785	0.281164	-56.0	0.6	-2.9	2397
03NA16-23C	14.7	3.4	0.281183	0.000019	0.000891	0.281141	-56.7	0.7	-3.0	2432

04NA16

Analysis	(^{176}Yb + ^{176}Lu) / ^{176}Hf (%)	Volts Hf	^{176}Hf/^{177}Hf	± (1σ)	^{176}Lu/^{177}Hf	^{176}Hf/^{177}Hf (T)	E-Hf (0)	E-Hf (0) ± (1σ)	E-Hf (T)	Age (Ma)
04NA16-3C	35.9	3.7	0.281040	0.000015	0.002000	0.280934	-61.7	0.5	-2.2	2781
04NA16-3R	16.9	4.3	0.281167	0.000018	0.000972	0.281121	-57.2	0.6	-2.9	2467
04NA16-17C	18.0	3.7	0.281024	0.000017	0.001100	0.280966	-62.3	0.6	-1.4	2766
04NA16-17R	12.6	4.3	0.281230	0.000017	0.000847	0.281189	-55.0	0.6	0.5	2507
04NA16-11C	19.1	3.9	0.280982	0.000016	0.001120	0.280923	-63.7	0.6	-3.3	2748
04NA16-11R	18.1	4.3	0.281175	0.000015	0.001173	0.281119	-56.9	0.5	-2.2	2496
04NA16-16C	25.8	3.7	0.281060	0.000016	0.001516	0.280979	-61.0	0.6	-0.4	2788
04NA16-2C	45.6	3.0	0.281107	0.000018	0.002597	0.280968	-59.3	0.6	-0.6	2794
04NA16-14R	12.0	3.6	0.280964	0.000018	0.000730	0.280927	-64.4	0.6	-4.7	2686
04NA16-20C	14.2	3.7	0.280989	0.000018	0.000877	0.280945	-63.5	0.7	-4.8	2652
04NA16-18C	25.9	3.7	0.280958	0.000018	0.001438	0.280883	-64.6	0.6	-5.4	2722
04NA16-19C	29.6	3.2	0.281056	0.000020	0.001710	0.280968	-61.2	0.7	-3.7	2662
04NA16-13C	13.3	3.7	0.281012	0.000015	0.000809	0.280970	-62.7	0.5	-3.3	2677
04NA16-4C	20.1	3.9	0.281008	0.000016	0.001060	0.280954	-62.8	0.6	-4.1	2669

18NA16

Analysis	$(^{176}Yb + ^{176}Lu) / ^{176}Hf$ (%)	Volts Hf	$^{176}Hf/^{177}Hf$	± (1σ)	$^{176}Lu/^{177}Hf$	$^{176}Hf/^{177}Hf$ (T)	E-Hf (0)	E-Hf (0) ± (1σ)	E-Hf (T)	Age (Ma)
18NA16-1C	24.2	3.1	0.281728	0.000017	0.001452	0.281679	-37.4	0.6	1.2	1789
18NA16-1R	7.7	3.9	0.281677	0.000016	0.000499	0.281660	-39.2	0.6	0.8	1797
18NA16-9C	12.5	4.7	0.281670	0.000014	0.000905	0.281639	-39.4	0.5	0.1	1800
18NA16-9R	5.8	4.1	0.281588	0.000019	0.000349	0.281577	-42.3	0.7	-2.5	1783
18NA16-5C	17.9	3.6	0.281688	0.000018	0.000990	0.281655	-38.8	0.6	-0.3	1759
18NA16-5R	5.8	3.9	0.281650	0.000018	0.000356	0.281638	-40.1	0.6	0.1	1803
18NA16-15R	7.6	3.9	0.281626	0.000017	0.000500	0.281611	-41.0	0.6	-5.1	1619
18NA16-13C	16.8	4.0	0.281709	0.000015	0.001060	0.281673	-38.0	0.5	1.7	1816
18NA16-8C	19.9	2.9	0.281744	0.000023	0.001317	0.281699	-36.8	0.8	2.3	1804
18NA16-14C	20.1	3.8	0.281620	0.000017	0.001207	0.281578	-41.2	0.6	-1.9	1808
18NA16-12C	21.6	3.9	0.281673	0.000016	0.001146	0.281634	-39.3	0.6	-0.4	1788
18NA16-6C	20.7	3.5	0.281701	0.000014	0.001318	0.281656	-38.3	0.5	0.8	1803
18NA16-7C	42.5	3.2	0.281785	0.000025	0.002253	0.281708	-35.4	0.9	2.7	1809
18NA16-10C	19.4	3.1	0.281706	0.000019	0.001149	0.281667	-38.2	0.7	0.2	1761

25NA16

Analysis	(^{176}Yb + ^{176}Lu) / ^{176}Hf (%)	Volts Hf	^{176}Hf/^{177}Hf	± (1σ)	^{176}Lu/^{177}Hf	^{176}Hf/^{177}Hf (T)	E-Hf (0)	E-Hf (0) ± (1σ)	E-Hf (T)	Age (Ma)
25NA16-55C	13.0	3.7	0.281355	0.000014	0.000825	0.281324	-50.6	0.5	-7.6	1952
25NA16-8C	11.7	3.6	0.281169	0.000015	0.000722	0.281135	-57.1	0.5	-2.3	2469
25NA16-8R	17.8	3.3	0.281419	0.000026	0.001212	0.281370	-48.3	0.9	-1.9	2129
25NA16-78C	9.9	2.4	0.281787	0.000025	0.000708	0.281763	-35.3	0.9	3.6	1760
25NA16-5R	11.1	4.0	0.281476	0.000019	0.000752	0.281451	-46.3	0.7	-7.7	1752
25NA16-2C	24.0	3.4	0.281206	0.000018	0.001190	0.281150	-55.8	0.6	-1.7	2473
25NA16-2R	13.9	4.1	0.281542	0.000017	0.000851	0.281513	-44.0	0.6	-4.8	1784
25NA16-3C	7.2	3.8	0.281365	0.000018	0.000462	0.281348	-50.2	0.6	-9.4	1837
25NA16-3R	10.3	3.8	0.281237	0.000015	0.000622	0.281208	-54.8	0.5	-1.9	2377
25NA16-41R	10.2	3.9	0.281423	0.000019	0.000670	0.281401	-48.2	0.7	-9.5	1752
25NA16-59C	10.0	3.8	0.281223	0.000017	0.000593	0.281195	-55.2	0.6	0.3	2489
25NA16-60C	21.3	3.5	0.281242	0.000016	0.001221	0.281184	-54.6	0.6	-0.2	2483
25NA16-10C	13.1	3.8	0.281210	0.000017	0.000756	0.281174	-55.7	0.6	-0.7	2476
25NA16-58C	22.5	3.6	0.281252	0.000017	0.001130	0.281198	-54.2	0.6	-0.1	2466
25NA16-30C	15.1	3.8	0.281252	0.000015	0.000912	0.281210	-54.2	0.5	-0.4	2436
25NA16-52C	7.6	4.3	0.281229	0.000017	0.000477	0.281206	-55.0	0.6	-0.5	2436
25NA16-12C	10.8	4.0	0.281242	0.000019	0.000641	0.281212	-54.6	0.7	-0.1	2446
25NA16-6C	21.7	3.7	0.281222	0.000020	0.001348	0.281158	-55.3	0.7	-1.5	2467
25NA16-80C	15.6	3.8	0.281242	0.000016	0.000988	0.281197	-54.6	0.6	-2.4	2369
25NA16-16C	7.8	4.4	0.281172	0.000013	0.000542	0.281147	-57.1	0.5	-3.4	2405
25NA16-71C	37.0	3.2	0.281252	0.000024	0.002316	0.281144	-54.2	0.8	-3.0	2426

Appendix D: (U-Th)/He analysis.

Appendix D includes the (U-Th)/He data of 4 zircon grains from sample 18NA16 from the felsic gneiss unit within the Bloody Dick gneiss.

18NA16

Zircon sample	U (ppm)	Th (ppm)	Th/U (atomic)	^{4}He (nmol/g)	Mass (µg)	Half-width (µm)	HAC (Ft)	Corrected age (Ma)	±2σ (Ma)
17A579_18NA16_z2	1276.85	172.43	0.143079417	446.17	1.40E-05	53.5	0.822	78.55	3.10
17A580_18NA16_z3	862.65	141.08	0.174481841	311.71	1.83E-05	59.25	0.838	79.63	5.40
17A581_18NA16_z4	1289.26	232.53	0.193214301	418.69	1.02E-05	43.5	0.790	76.00	5.15
17A583_18NA16_Z6	728.11	150.46	0.222808761	223.8	1.43E-05	55.25	0.828	68.7	1.90

Appendix E: Petrography.

Appendix E includes the analysis of 30 µm thin sections for relative mineral abundances and identification of deformational features. It also includes plane polarized light and cross polarized light images of each sample that was analyzed.

01NA16: Plane polarized light (left), cross polarized light (right).

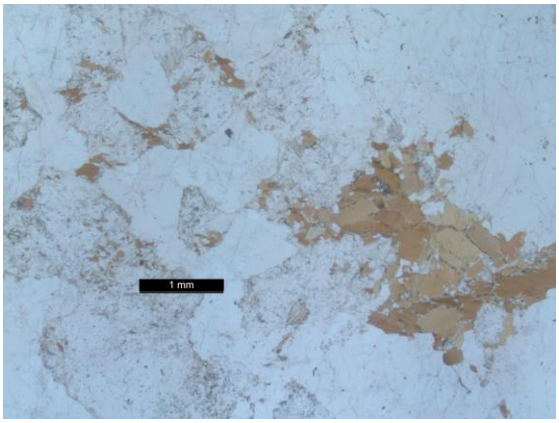

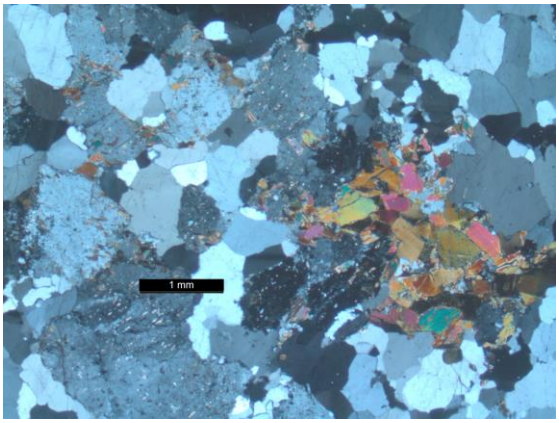

02NA16: Plane polarized light (left), cross polarized light (right).

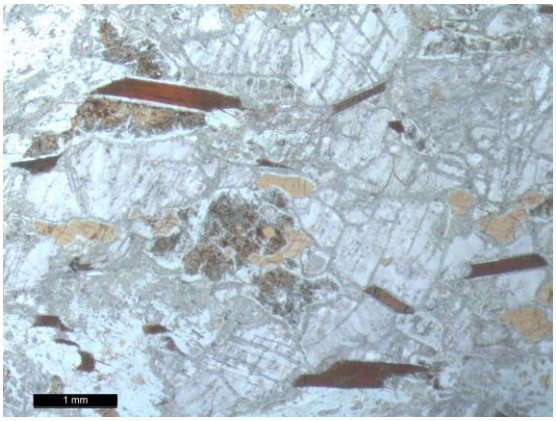

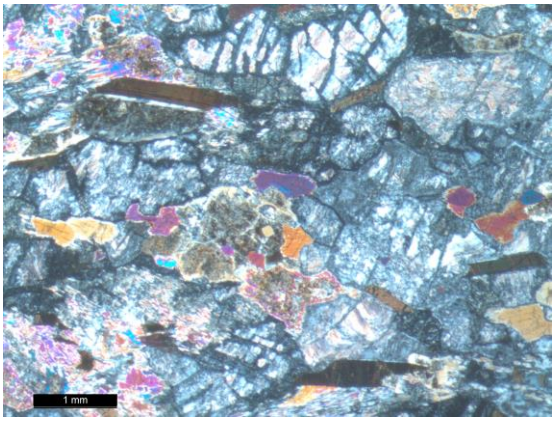

03NA16: Plane polarized light (left), cross polarized light (right).

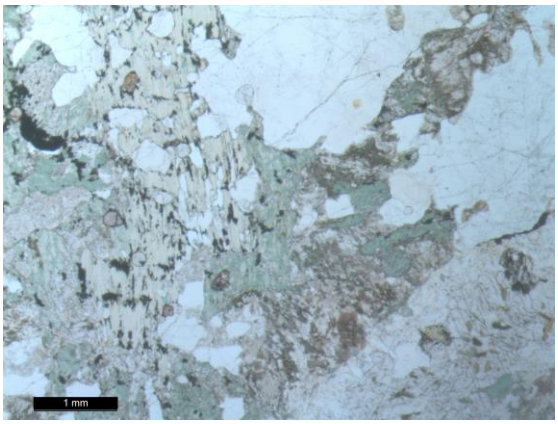

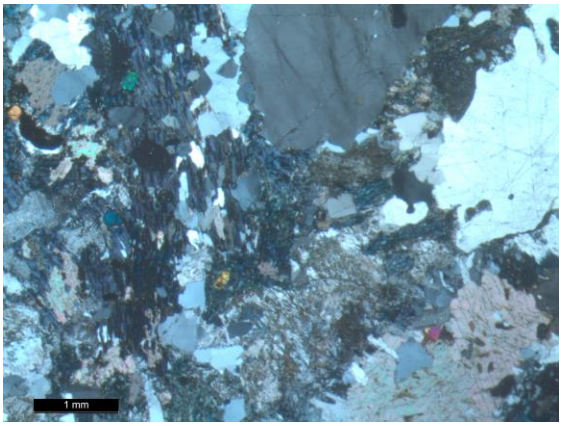

04NA16: Plane polarized light (left), cross polarized light (right).

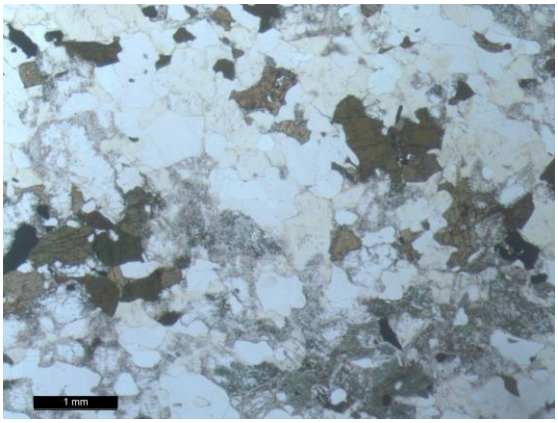

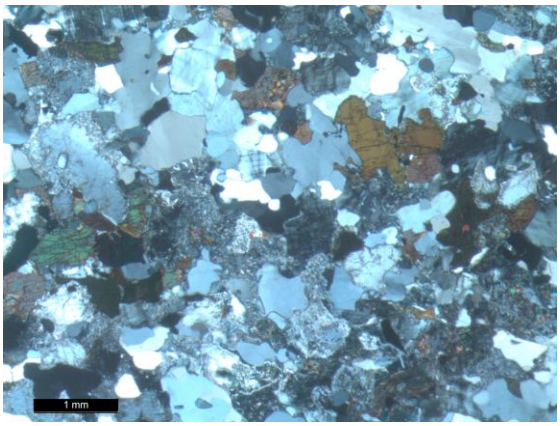

05NA16: Plane polarized light (left), cross polarized light (right).

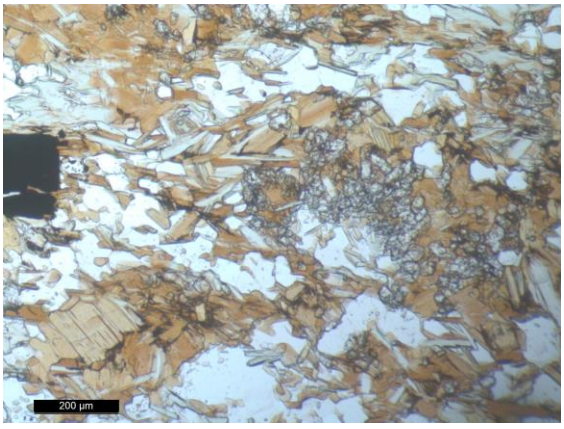

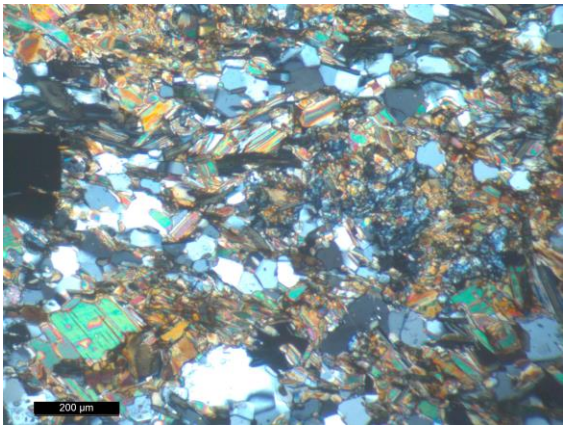

06NA16: Plane polarized light (left), cross polarized light (right).

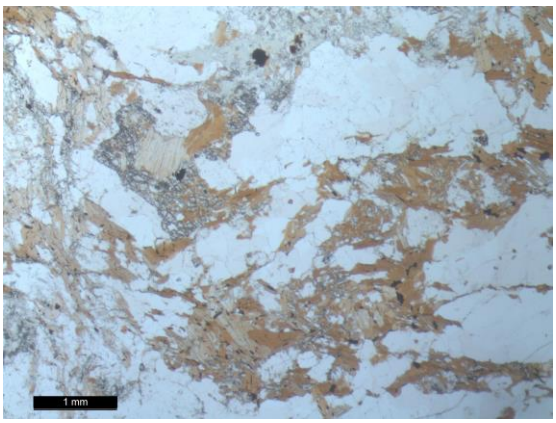

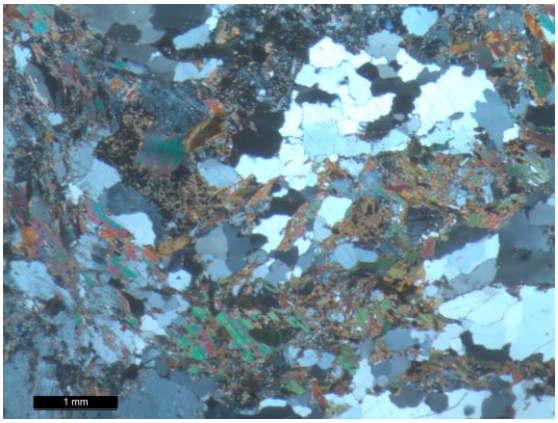

08NA16: Plane polarized light (left), cross polarized light (right).

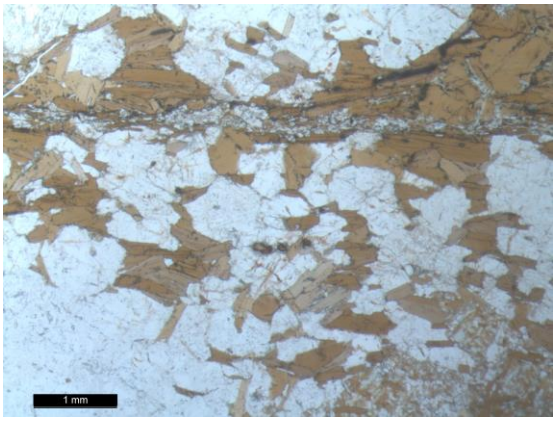

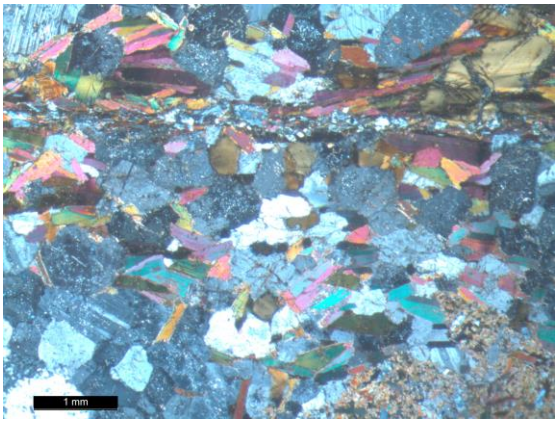

09NA16: Plane polarized light (left), cross polarized light (right).

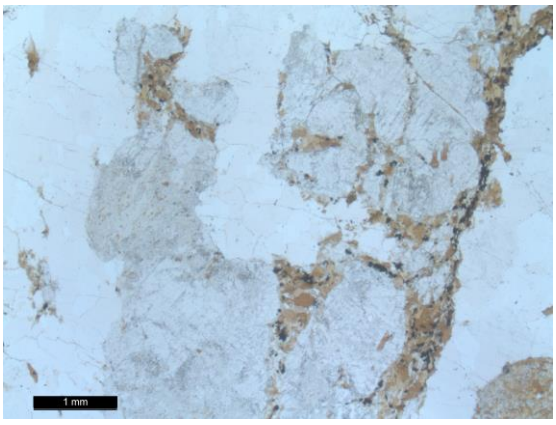

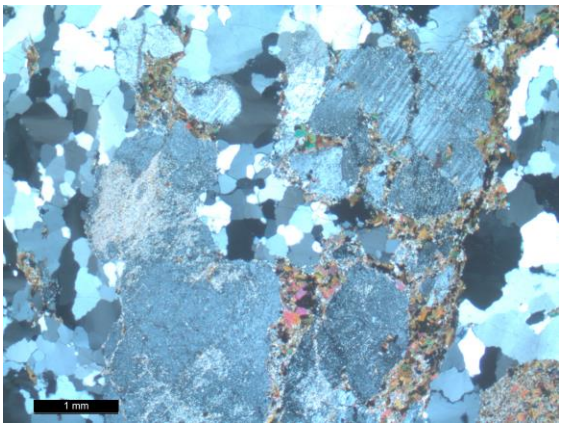

11NA16: Plane polarized light (left), cross polarized light (right).

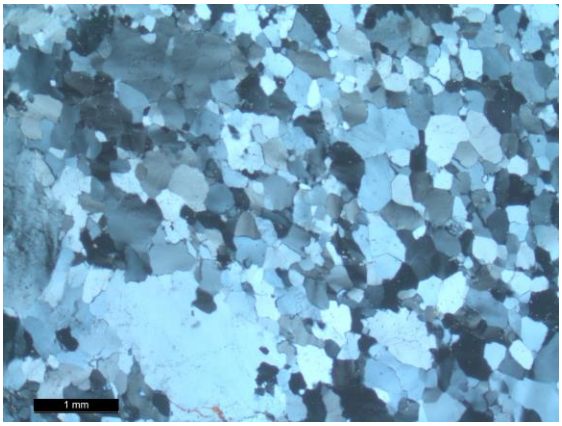

12NA16: Plane polarized light (left), cross polarized light (right).

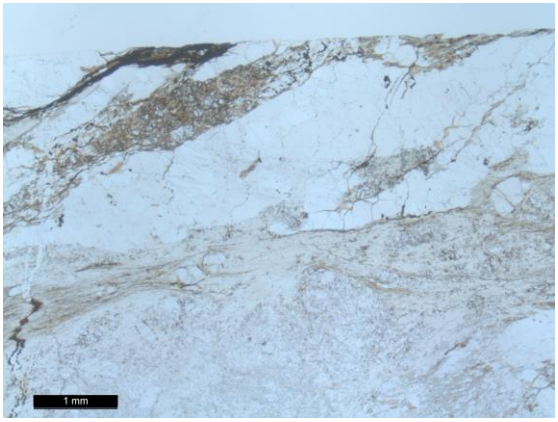

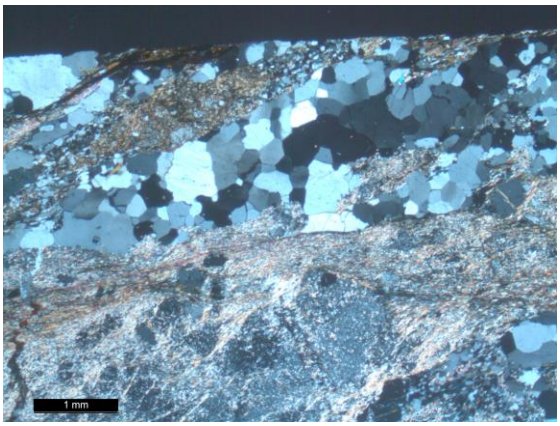

14NA16A, oriented: Plane polarized light (left), cross polarized light (right).
Plane of view is sub-vertical looking towards 244° (southwest). Ductile fabrics are interpreted as preserving a "top to the right" sense of shear.

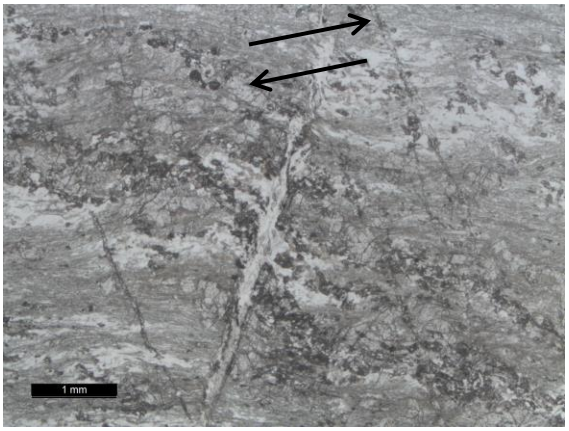

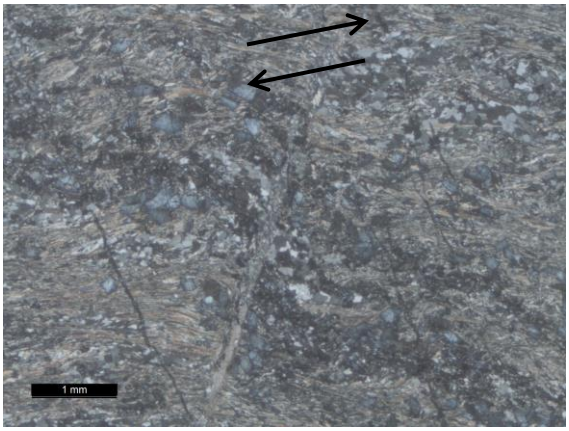

14NA16B: Plane polarized light (left), cross polarized light (right).

Plane of view is sub-vertical looking towards 257° (west-southwest).

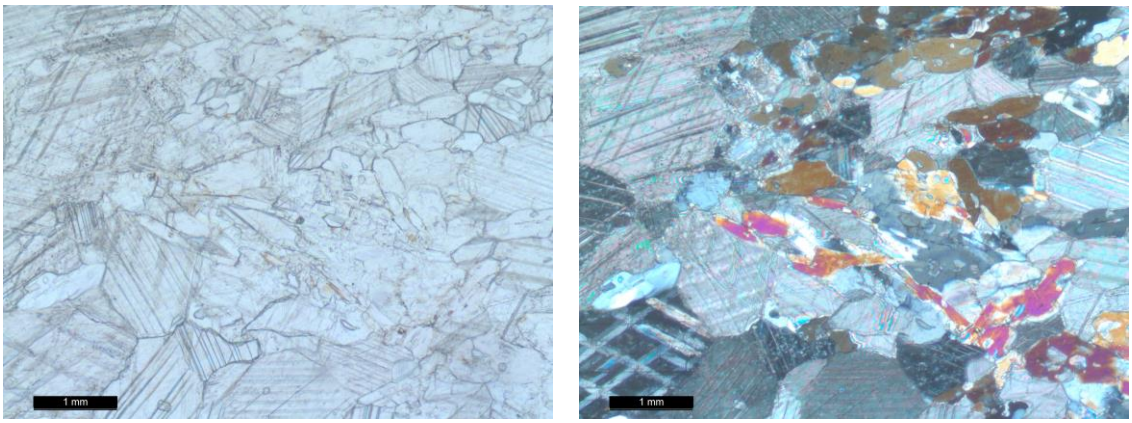

17NA16: Plane polarized light (left), cross polarized light (right).

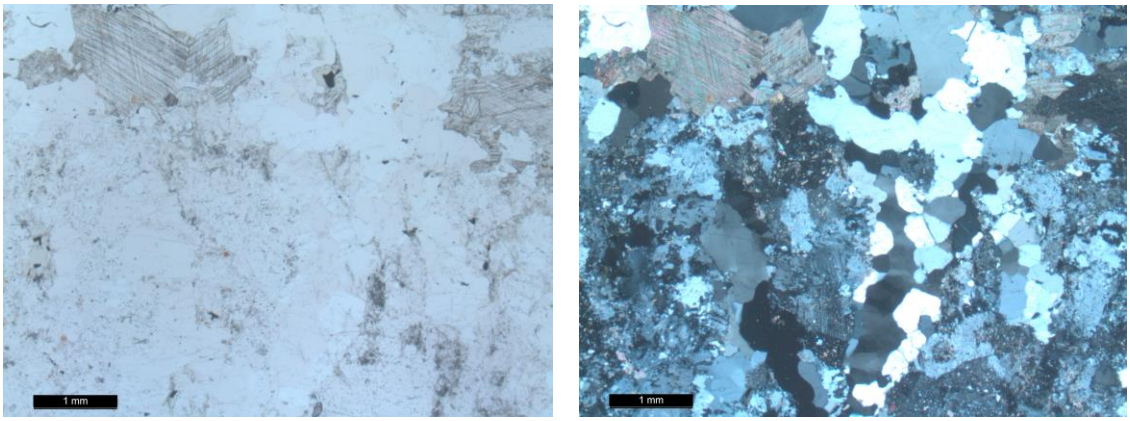

18NA16: Plane polarized light (left), cross polarized light (right).

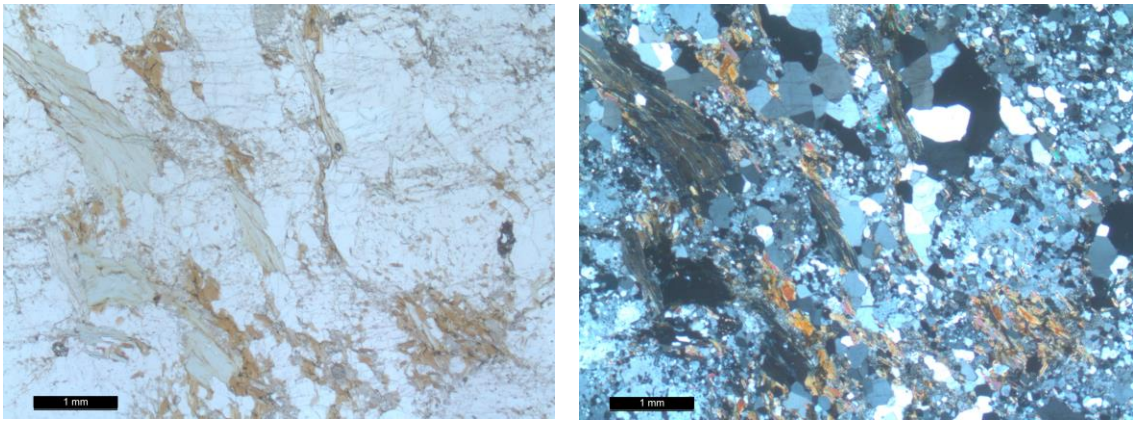

19NA16: Plane polarized light (left), cross polarized light (right).

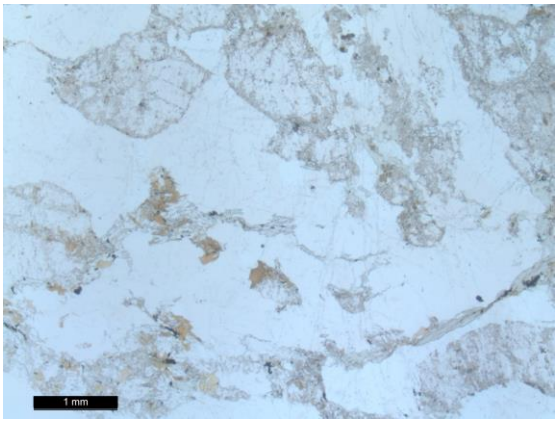

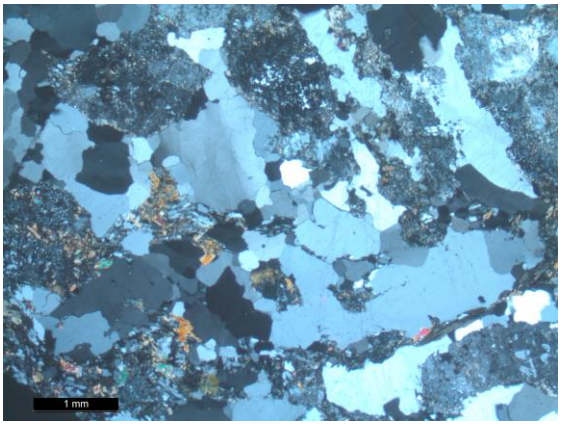

20NA16: Plane polarized light (left), cross polarized light (right).

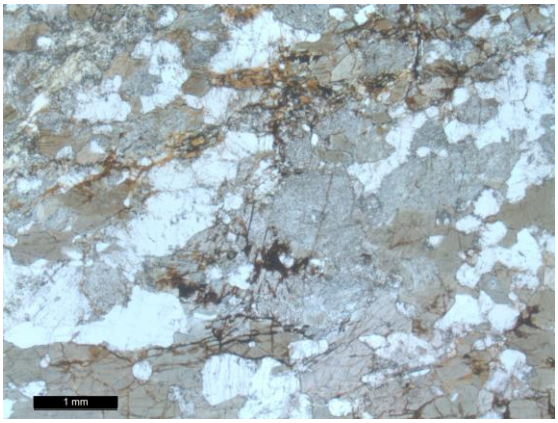

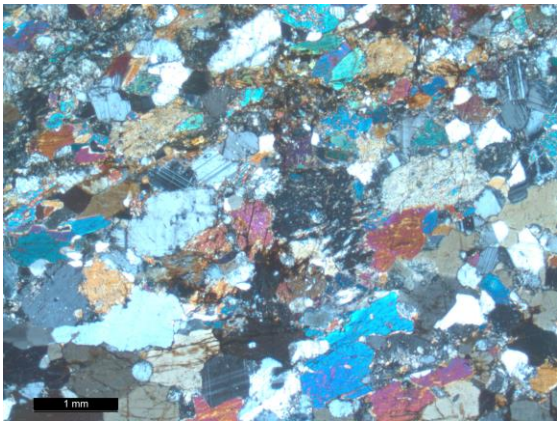

21NA16: Plane polarized light (left), cross polarized light (right).

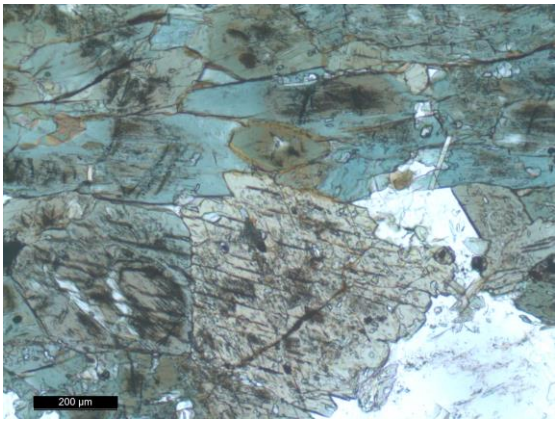

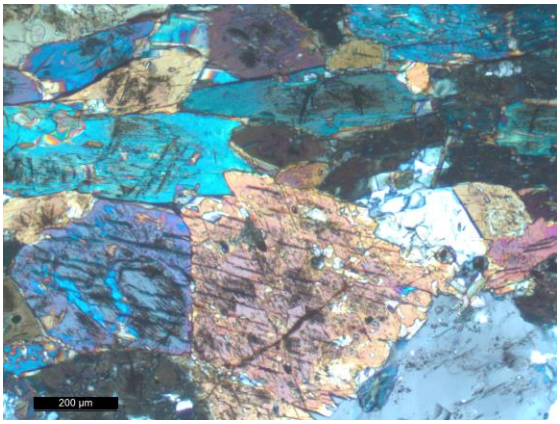

22NA16 oriented: Plane polarized light (left), cross polarized light (right).
Plane of view is looking towards 114° (east-southeast) and down 40°.

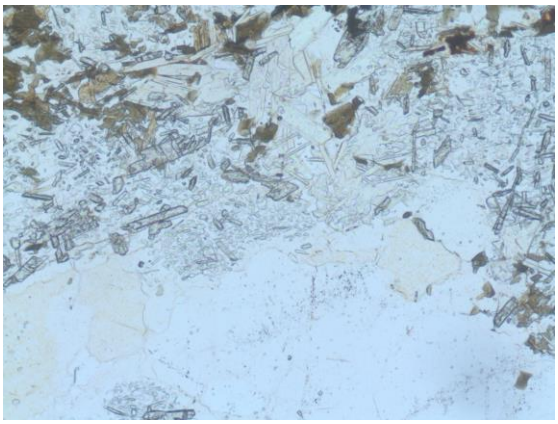

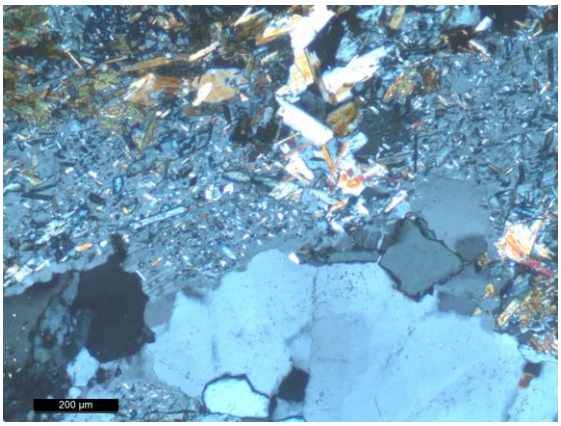

23NA16 oriented: Plane polarized light (left), cross polarized light (right).
Plane of view is looking towards 100° (east) and down 40°.

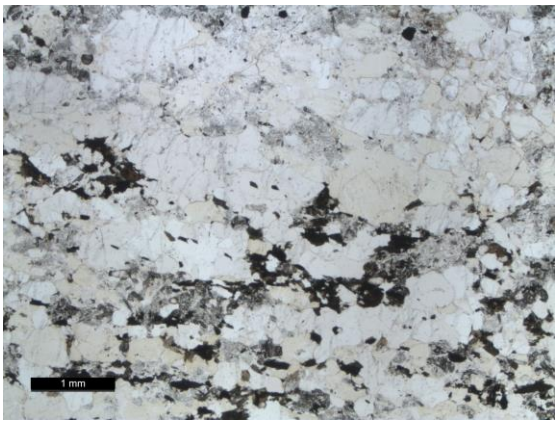

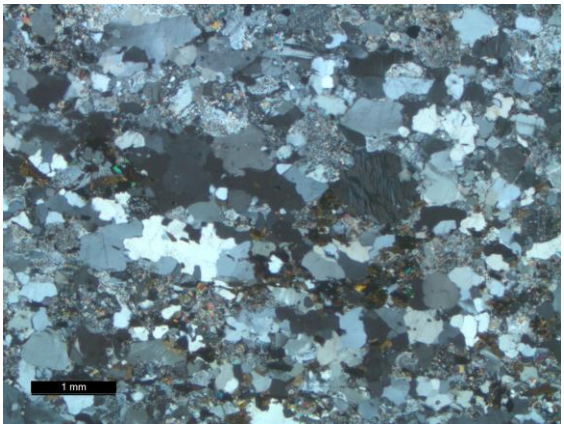

25NA16: Plane polarized light (left), cross polarized light (right).

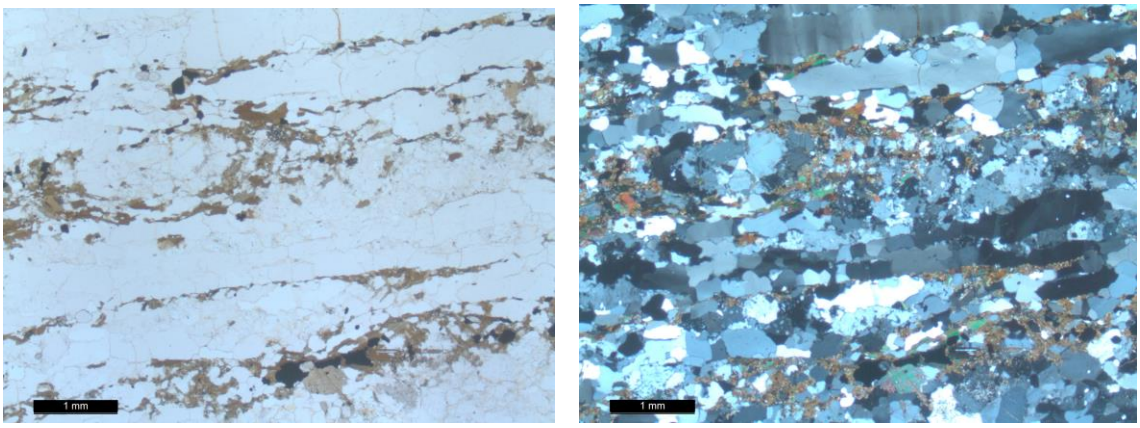

26NA16: Plane polarized light (left), cross polarized light (right).

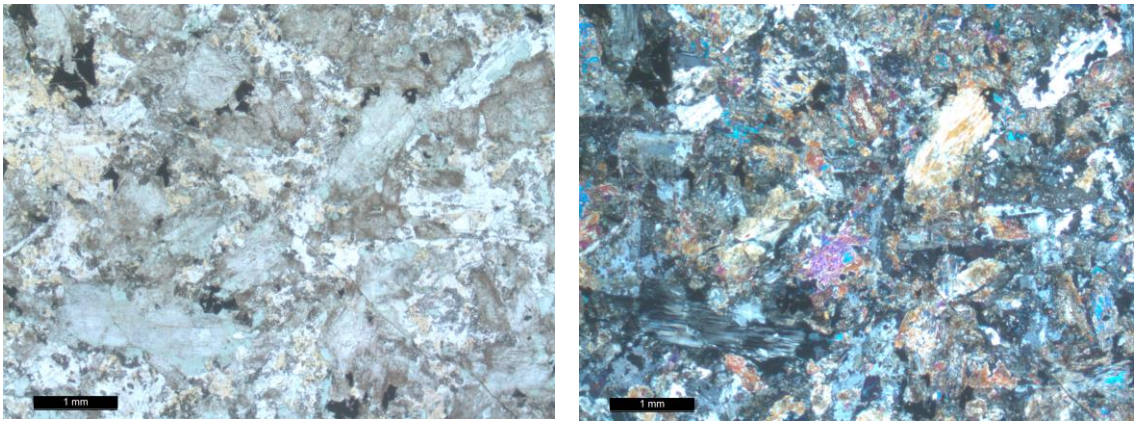

Plate 1: Geologic map of the Bloody Dick gneiss

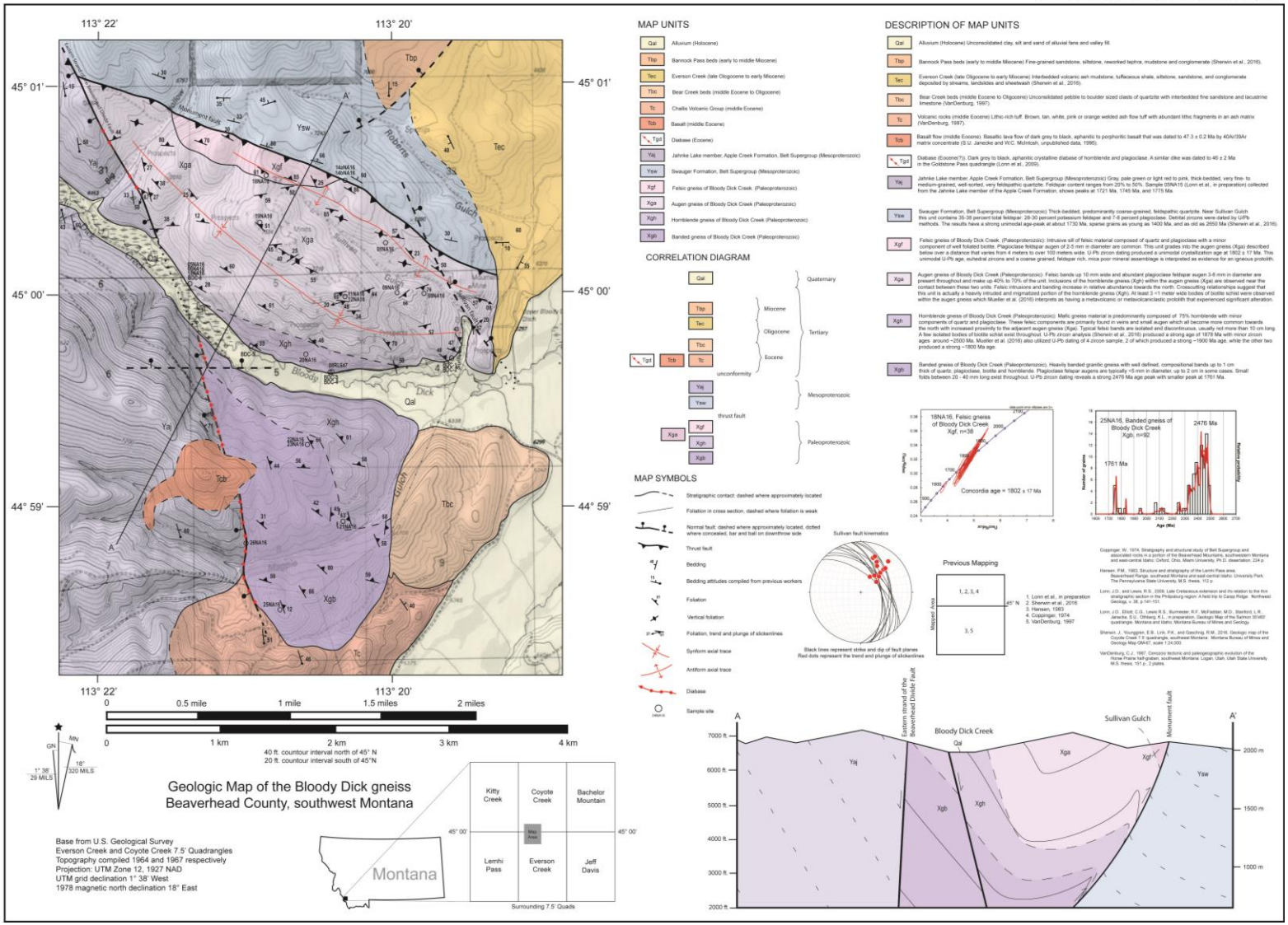
113° 22'
113° 20'
45° 01'
45° 00'
44° 59'
Tbp
Tec
Ysw
Xga
Xgf
Yaj
Qal
Xgh
Xgb
Tcb
Tbc
Tc
Tgd
Sullivan Gulch
Bloody Dick Creek
Robbins Gulch
Monument fault
0 0.5 mile 1 mile 1.5 miles 2 miles
0 1 km 2 km 3 km 4 km
40 ft. countour interval north of 45° N
20 ft. countour interval south of 45°N
Geologic Map of the Bloody Dick gneiss
Beaverhead County, southwest Montana
Base from U.S. Geological Survey
Everson Creek and Coyote Creek 7.5' Quadrangles
Topography compiled 1964 and 1967 respectively
Projection: UTM Zone 12, 1927 NAD
UTM grid declination 1° 38' West
1978 magnetic north declination 18° East
Montana
Kitty Creek
Coyote Creek
Bachelor Mountain
Lemhi Pass
Everson Creek
Jeff Davis
Surrounding 7.5' Quads
MAP UNITS
Qal Alluvium (Holocene)
Tbp Bannock Pass beds (early to middle Miocene)
Tec Everson Creek (late Oligocene to early Miocene)
Tbc Bear Creek beds (middle Eocene to Oligocene)
Tc Challis Volcanic Group (middle Eocene)
Tcb Basalt (middle Eocene)
Tgd Diabase (Eocene)
Yaj Jahnke Lake member, Apple Creek Formation, Belt Supergroup (Mesoproterozoic)
Ysw Swauger Formation, Belt Supergroup (Mesoproterozoic)
Xgf Felsic gneiss of Bloody Dick Creek. (Paleoproterozoic)
Xga Augen gneiss of Bloody Dick Creek (Paleoproterozoic)
Xgh Hornblende gneiss of Bloody Dick Creek (Paleoproterozoic)
Xgb Banded gneiss of Bloody Dick Creek (Paleoproterozoic)
CORRELATION DIAGRAM
Quaternary
Tertiary
Miocene
Oligocene
Eocene
unconformity
Mesoproterozoic
thrust fault
Paleoproterozoic
MAP SYMBOLS
Stratigraphic contact: dashed where approximately located
Foliation in cross section, dashed where foliation is weak
Normal fault: dashed where approximately located, dotted where concealed, bar and ball on downthrow side
Thrust fault
Bedding
Bedding attitudes compiled from previous workers
Foliation
Vertical foliation
Foliation, trend and plunge of slickenlines
Synform axial trace
Antiform axial trace
Diabase
Sample site
DESCRIPTION OF MAP UNITS
Qal Alluvium (Holocene) Unconsolidated clay, silt and sand of alluvial fans and valley fill.
Tbp Bannock Pass beds (early to middle Miocene) Fine-grained sandstone, siltstone, reworked tephra, mudstone and conglomerate (Sherwin et al., 2016).
Tec Everson Creek (late Oligocene to early Miocene) Interbedded volcanic ash mudstone, tuffaceous shale, siltstone, sandstone, and conglomerate deposited by streams, landslides and sheetwash (Sherwin et al., 2016).
Tbc Bear Creek beds (middle Eocene to Oligocene) Unconsolidated pebble to boulder sized clasts of quartzite with interbedded fine sandstone and lacustrine limestone (VanDenburg, 1997).
Tc Volcanic rocks (middle Eocene) Lithic-rich tuff. Brown, tan, white, pink or orange welded ash flow tuff with abundant lithic fragments in an ash matrix (VanDenburg, 1997).
Tcb Basalt flow (middle Eocene). Basaltic lava flow of dark grey to black, aphanitic to porphoritic basalt that was dated to 47.3 ± 0.2 Ma by 40Ar/39Ar matrix concentrate (S.U. Janecke and W.C. McIntosh, unpublished data, 1995).
Tgd Diabase (Eocene(?)): Dark grey to black, aphanitic crystalline diabase of hornblende and plagioclase. A similar dike was dated to 46 ± 2 Ma in the Goldstone Pass quadrangle (Lonn et al., 2009).
Yaj Jahnke Lake member, Apple Creek Formation, Belt Supergroup (Mesoproterozoic) Gray, pale green or light red to pink, thick-bedded, very fine- to medium-grained, well-sorted, very feldspathic quartzite. Feldspar content ranges from 20% to 50%. Sample 05NA15 (Lonn et al., in preparation) collected from the Jahnke Lake member of the Apple Creek Formation, shows peaks at 1721 Ma, 1745 Ma, and 1775 Ma.
Ysw Swauger Formation, Belt Supergroup (Mesoproterozoic) Thick-bedded, predominantly coarse-grained, feldspathic quartzite. Near Sullivan Gulch this unit contains 35-38 percent total feldspar 28-30 percent potassium feldspar and 7-8 percent plagioclase. Detrital zircons were dated by U/Pb methods. The results have a strong unimodal age-peak at about 1730 Ma, sparse grains as young as 1400 Ma, and as old as 2650 Ma (Sherwin et al., 2016).
Xgf Felsic gneiss of Bloody Dick Creek. (Paleoproterozoic). Intrusive sill of felsic material composed of quartz and plagioclase with a minor component of well foliated biotite. Plagioclase feldspar augen of 2-5 mm in diameter are common. This unit grades into the augen gneiss (Xga) described below over a distance that varies from 4 meters to over 100 meters wide. U-Pb zircon dating produced a unimodal crystallization age at 1802 ± 17 Ma. This unimodal U-Pb age, euhedral zircons and a coarse grained, feldspar rich, mica poor mineral assemblage is interpreted as evidence for an igneous protolith.
Xga Augen gneiss of Bloody Dick Creek (Paleoproterozoic). Felsic bands up 10 mm wide and abundant plagioclase feldspar augen 3-6 mm in diameter are present throughout and make up 40% to 70% of the unit. Inclusions of the hornblende gneiss (Xgh) within the augen gneiss (Xga) are observed near the contact between these two units. Felsic intrusions and banding increase in relative abundance towards the north. Crosscutting relationships suggest that this unit is actually a heavily intruded and migmatized portion of the hornblende gneiss (Xgh). At least 3 <1 meter wide bodies of biotite schist were observed within the augen gneiss which Mueller et al. (2016) interprets as having a metavolcanic or metavolcaniclastic protolith that experienced significant alteration.
Xgh Hornblende gneiss of Bloody Dick Creek (Paleoproterozoic). Mafic gneiss material is predominantly composed of 75% hornblende with minor components of quartz and plagioclase. These felsic components are primarily found in veins and small augen which all become more common towards the north with increased proximity to the adjacent augen gneiss (Xga). Typical felsic bands are isolated and discontinuous, usually not more than 10 cm long. A few isolated bodies of biotite schist exist throughout. U-Pb zircon analysis (Sherwin et al., 2016) produced a strong age of 1878 Ma with minor zircon ages around ~2550 Ma. Mueller et al. (2016) also utilized U-Pb dating of 4 zircon sample, 2 of which produced a strong ~1900 Ma age, while the other two produced a strong ~1800 Ma age.
Xgb Banded gneiss of Bloody Dick Creek (Paleoproterozoic). Heavily banded granitic gneiss with well defined, compositional bands up to 1 cm thick of quartz, plagioclase, biotite and hornblende. Plagioclase feldspar augens are typically <5 mm in diameter, up to 2 cm in some cases. Small folds between 20 - 40 mm long exist throughout. U-Pb zircon dating reveals a strong 2475 Ma age peak with smaller peak at 1761 Ma.
18NA16, Felsic gneiss of Bloody Dick Creek Xgf, n=38
Concordia age = 1802 ± 17 Ma
25NA16, Banded gneiss of Bloody Dick Creek Xgb, n=92
2475 Ma
1761 Ma
Number of grains
Relative probability
Age (Ma)
Sullivan fault kinematics
Black lines represent strike and dip of fault planes
Red dots represent the trend and plunge of slickenlines
Previous Mapping
Mapped Area
1, 2, 3, 4
3, 5
45° N
1. Lonn et al., in preparation
2. Sherwin et al., 2016
3. Hansen, 1983
4. Coppinger, 1974
5. VanDenburg, 1997
Coppinger, W., 1974, Stratigraphy and structural study of Belt Supergroup and associated rocks in a portion of the Beaverhead Mountains, southwestern Montana and east-central Idaho: Oxford, Ohio, Miami University, Ph.D. dissertation, 224 p.
Hansen, P.M., 1983, Structure and stratigraphy of the Lemhi Pass area, Beaverhead Range, southwest Montana and east-central Idaho: University Park, The Pennsylvania State University, M.S. thesis, 112 p.
Lonn, J.D., and Lewis, R.S., 2009, Late Cretaceous extension and its relation to the thin stratigraphic section in the Philipsburg region: A field trip to Carpp Ridge: Northwest Geology, v. 38, p.141-157.
Lonn, J.D., Elliott, C.G., Lewis, R.S., Sunnseder, R.F., McFaddan, M.D., Stanford, L.R., Janecke, S.U., Ottenberg, K.L., in preparation, Geologic Map of the Salmon 30'x60' quadrangle, Montana and Idaho: Montana Bureau of Mines and Geology.
Sherwin, J., Youngpeter, E.B., Lonn, P.K., and Gieschnig, R.M., 2016, Geologic map of the Coyote Creek 7.5' quadrangle, southwest Montana: Montana Bureau of Mines and Geology Map GM407, scale 1:24,000.
VanDenburg, C.J., 1997, Cenozoic tectonic and paleogeographic evolution of the Horse Prairie half-graben, southwest Montana: Logan, Utah, Utah State University M.S. thesis, 151 p., 2 plates.
A
A'
Eastern strand of the Beaverhead Divide Fault
Bloody Dick Creek
Sullivan Gulch
Monument fault
Qal
Yaj
Xga
Xgf
Ysw
Xgb
Xgh
7000 ft.
6000 ft.
5000 ft.
4000 ft.
3000 ft.
2000 ft.
2000 m
1500 m
1000 m